A grayscale background image of a microscope. The objective lenses are visible at the top, with labels such as '10X/0.70' and '5X 0.15'. The eyepiece is on the right. The central part of the microscope is in focus, showing the stage and the specimen being examined.

# An Experimental Approach to Study Drainage in Relation to Geometrical Features of Artificial Adhesives

By

W. De Geyndt

in partial fulfilment of the requirements for the degree of

**Master of Science**  
In Mechanical Engineering

at the Delft University of Technology,  
to be defended publicly on Wednesday August 28, 2019 at 10:00 AM.

Supervisor:

Dr. D. Dodou  
P. van Assenbergh, MSc

Thesis committee:

Dr. D. Dodou,  
P. van Assenbergh, MSc  
Dr. Pouyan Boukany,

TU Delft  
TU Delft  
TU Delft

 **TU Delft**

An electronic version of this thesis is available at <http://repository.tudelft.nl/>.



# Preface

This thesis, “An Experimental Approach to Study Drainage in Relation to Geometrical Features of Artificial Adhesives”, describes my graduation project for the MSc program Mechanical Engineering, track Biomechanical Design. This work has been written to fulfil the graduation requirements of this program at Delft University of Technology. The focus of this work lies on fluid flows in wet adhesive technology.

This research was conducted at the TU Delft. The work was preceded by a literature research to accumulate knowledge on the state of the art regarding fluidic measurement methods. Listing these measurement methods aided in choosing a method capable of fulfilling the needs of the thesis goal. The goal of this research is to experimentally determine the influence of pillar diameter, spacing, alignment, and fluidic medium on the flow profile using Particle Image Velocimetry (PIV).

I would like to thank the staff at the TU Delft Applied Sciences building for giving access to various equipment and for the opportunity to collect my data. Especially I would like to thank Dimitra Dodou and Peter Van Assenbergh for their guidance and support. Questions, discussion, and alterations towards the project could be introduced to them at any time allowing for quick adaptations when needed. I would also like to thank Gerrit E. Elsinga and Ben Norder for allowing access to software and hardware required for this project.

Enjoy reading,

*W. De Geyndt  
Delft, August 2019*



# Contents

Abstract .....	6
1. Introduction.....	7
1.1 Background.....	7
1.2 State of The Art on Drainage Research .....	7
1.3 Thesis goal.....	8
2. Materials and Methods .....	9
2.1 Variables.....	9
2.2 Sample Types.....	9
2.2.1 Fabrication Method.....	10
2.3 Experimental Setup .....	11
2.3.1 Components of the Setup.....	11
2.3.2 Motion of the Setup .....	13
2.4 Experimental Procedure .....	13
2.4.1 Calibration of The Setup.....	13
2.4.2 Data Collection.....	13
2.4.3 Quality Inspection .....	14
2.4.4 Image Conversion .....	15
2.4.5 PIV Analysis .....	15
2.4.6 Statistical Analysis.....	16
3. Results .....	17
3.1 Water as a Fluid Type .....	17
3.2 Glycerol as a Fluid Type .....	19
3.3 Fluid Type Effect .....	22
4. Discussion .....	23
4.1 Effect of Diameter on Drainage .....	23
4.2 Effect of Spacing on Drainage .....	23
4.3 Effect of Alignment on Drainage.....	23
4.4 Effect of Fluid Type on Drainage.....	24
4.5 Limitations .....	24
5. Conclusion.....	26
References .....	27
Appendices .....	29

# Abstract

With growing interest in wet adhesion, animals such as tree frogs are often used as paradigm for creating grippers in wet environments. Tree frogs are capable of attaching to surfaces under several conditions (smooth, rough, dry, wet, and flooded) due to the microstructure of their toe pads. This microstructure consists of pillar-shaped hexagonal cells separated by thin and deep channels. Drainage is an important phenomenon to consider, since too much liquid between the toe pad and surface results in a low adhesive force. Therefore, understanding the relationship between pillar-shaped microstructures and drainage can lead to the creation of adhesive pads that are functional in wet conditions and to other drainage related applications.

Adhesives with a pillar-shaped microstructure were fabricated and their drainage speed was experimentally studied against a glass substrate. Gathering experimental data was accomplished by using Particle Image Velocimetry, and by using fluid velocity as a proxy for drainage. A custom-made set-up was built to accurately control the speed at which the adhesive and the substrate approached each other. Adhesives with various pillar diameters, pillar spacings, and pillar alignments were tested with fluids of various viscosities. It was found that the pillar diameter most likely has a significant effect on drainage, whereas the effect of pillar spacing and the effect of fluid type could not be determined. Pillar alignment did not have a significant effect on drainage.

In future work, it is recommended to complement the findings of this thesis with adhesion and friction measurements to understand how drainage associates to adhesive force.

Keywords: Fluid Flow, Particle Image Velocimetry, Artificial Adhesive, Wet Adhesion

# 1. Introduction

## 1.1 Background

Coulomb friction is determined by the normal force between two surfaces multiplied by the friction coefficient. When a force acts on one of the two surfaces, parallel to those surfaces, slipping will occur when the force of friction is exceeded. When a liquid such as water is present between these two surfaces the coefficient of friction reduces, resulting in the surfaces being more prone to slip.

Friction and adhesion are fundamental to animal locomotion and maneuverability [1]. Yet various animals live in a wet environment, which causes water to be present between the locomotory organ and the surface upon which the animal moves. Animals employ micropatterned surfaces that presumably promote drainage and enhance adhesion. Such micropatterned surfaces deserve to be studied for potential engineering applications such as grippers, as well as in order to gain a better understanding of the inner workings of biological grip [2]–[5].

Drainage is defined in this thesis as the ability to expel excess liquid between the micropatterned adhesive (locomotory organ) and the substrate [6]. The expulsion of excess liquid happens due to a generated pressure by the adhesive approaching the substrate, which builds up a pressure field on the liquid. When this pressure field on the liquid exceeds a certain threshold, fluid will flow towards a lower pressure environment (away from the substrate). In this paper, experimental data will be gathered and analyzed regarding drainage, proxied by fluid velocity.

## 1.2 State of The Art on Drainage Research

The first studies about drainage and adhesion are dated from the 1960's, when researchers tried to create higher skid resistant tires [7] and pavements [8]. The conclusion was that "The experiments showed the importance of adequate drainage of the region of contact between tyre and road" [7]. Since then, an increasing amount of research has been conducted regarding drainage and adhesion in wet conditions.

One direction of research focused on improving commercially available products such as wheels (cars, planes, bikes) [7], [9], [10], robotics [11], and shoes [12]. Another research direction concerns biomimetic methods. Biological organisms are till this day often used as an inspiration source. Animals like tree frogs [13], chameleons [14], and geckos [15] became inspiration sources for their impressive adhesive abilities in wet conditions, thanks to their micropatterned locomotory organs. This led to research on the effect of geometrical characteristics of micropatterned adhesives on drainage [3], [5]. In this research drainage was mostly represented by the flow field between the substrate and the adhesive.

Flow field research regarding drainage and micropatterned adhesives showed three flow field regimes (near-, intermediate-, and far-field). The occurrence of these regimes was determined according to Equation (1) [3]:

$$h_0 = D \left( \frac{w}{w+d} \right)^{\frac{1}{3}} \quad (1)$$

where  $D$  is the pillar height,  $w$  is the pillar spacing,  $d$  is the pillar diameter, and  $h_0$  is the height at which the flow field changes. When the substrate distance from the adhesive ( $h$ ) is larger than  $h_0$ , the far-field regime occurs, when  $h \sim h_0$  an intermediate flow field occurs, and when  $h \ll h_0$  near-field regime is at play. The far-field means that flow passed above the micropatterned area, the intermediate field is a transitional phase between far- and near-field, and near-field meant that flow occurs between the pillars. Equation (1) only held true for smooth surfaces, and in the absence of any contributions due to the effect of chemistry, deformation, or other surface forces.

Research on far-field drainage for micropatterned adhesives concluded that when channels divided a micropatterned adhesive into  $n$  separate smaller structures (of radii  $r < R/\sqrt{n}$ ), the drainage was  $n$  times faster, according to Equation (2) [5]:

$$F_r = F_R/n \text{ and } t_r \propto \frac{r^4}{F_r} \propto t_R/n \quad (2)$$

where  $R$  is the radius of the adhesive,  $r$  is the radius of the circular pillars that are separated by the channels,  $n$  is the number of circular pillars, and  $t$  is the time required for the adhesive and substrate to reach each other depending on the amount of force applied  $F$ . The drainage time was theoretically derived with the assumption that the two surfaces were cylindrical, had no deformation, smooth surface, and that the adhesive, and micropatterned structures were both circular. This theoretical finding was not experimentally confirmed.

Previous research also did mention that a more viscous fluid is expected to result in lower fluid velocity, thus slower drainage [5]. Overall, relatively little experimental data is available on how the viscosity of the fluid and micropatterned geometries affect drainage. Therefore, this thesis, focused on experimentally gathering fluid flow data in the far-field region, to compare with previous research findings.

### 1.3 Thesis goal

The goal of this thesis was to experimentally investigate the effect of geometrical characteristics and the effect of fluid viscosity on drainage. The geometrical characteristics investigated were the diameter of the pillars, the side-to-side spacing between the pillars, and the alignment of the pillars. Also, the effect from fluid viscosity was investigated.

In this thesis, drainage was proxied by fluid velocity. Fluid velocity was experimentally recorded over time and analyzed using the PIV method. Based on the state-of-the-art, it was expected that a smaller diameter and smaller spacing both resulted in faster drainage. The alignment of the pillars was expected to not have any effect on drainage. Furthermore, it was expected that a more viscous fluid will lead to slower drainage due to the much higher resistance against movement caused by viscosity.



## 2. Materials and Methods

This section describes the variables of the experiment, samples used, measurement setup, and experimental procedure. Following the experimental procedure, the data filtering and data analysis methods are briefly described.

### 2.1 Variables

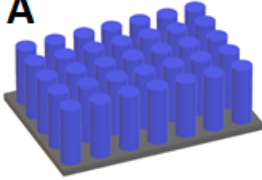
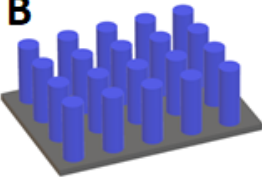
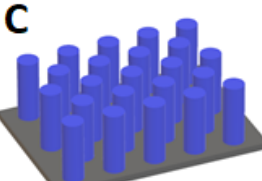
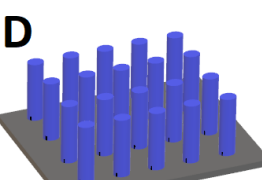
Drainage was investigated as a function of the following independent variables:

- *Pillar Diameter:*  
Pillars with circular cross-sectional diameters of 20  $\mu\text{m}$  and 80  $\mu\text{m}$  were tested. The diameter of 20  $\mu\text{m}$  was chosen as the smallest possible diameter to fabricate without defects with the chosen fabrication method (see section 2.2.1). The 80  $\mu\text{m}$  was chosen as the maximum diameter in combination with the maximum pillar spacing to ensure at least 4 complete pillars were recorded (see section 2.3.1) at any time during a measurement.
- *Pillar Spacing:*  
The pillar spacing was defined as a side-to-side distance with 20  $\mu\text{m}$  and 40  $\mu\text{m}$ . Similar to the diameter of 20  $\mu\text{m}$ , the spacing of 20  $\mu\text{m}$  was also chosen based on fabrication capabilities. The 40  $\mu\text{m}$  was chosen as the maximum spacing in combination with the maximum pillar diameter to ensure at least 4 complete pillars were recorded at any time during a measurement.
- *Pillar Alignment:*  
Pillar alignment refers to the parallel and offset alignments that were tested. Parallel aligned meant that the pillars were aligned parallel to the sample's sides. Offset referred to the pillars' alignment being 45° offset from the sample's sides. The 45° offset was chosen as the most extreme offset possible.
- *Fluid Type:*  
Fluid type refers to the fluid film between the substrate and adhesive. Two fluid types were tested: water and glycerol. Water was chosen as the most common medium used in the literature investigating adhesion in wet conditions [3], [5], [16]–[18]. Glycerol was chosen due to the refractive index being closely related to water (water 1.33 vs glycerol 1.47) while having a large difference in viscosity ( $8.90 \times 10^{-4}$  Pa·s for water vs. 1.412 Pa·s for glycerol). Similar refractive indexes kept the minimized differences of optical distortions due to light passing through the fluid, ensuring easier comparison.

### 2.2 Sample Types

A total of four sample types (Table 1), henceforth referred to as samples, were used. These samples were chosen such that there were always two samples which differed from each other in terms of only one of the independent variables. All samples were 1000 x 1000  $\mu\text{m}$ , and had pillars with a circular cross-section, a height of 12  $\mu\text{m}$ , and other geometrical dimensions matching the independent variables. Cylindrical pillars were chosen because these are frequently encountered in the literature and relatively easy to manufacture [18]–[23].

**Table 1:** The four sample types used: A) sample with pillar diameter of 80  $\mu\text{m}$ , spacing of 20  $\mu\text{m}$ , and an aligned pillar array (D80S20A), B) sample with pillar diameter of 80  $\mu\text{m}$ , spacing of 40  $\mu\text{m}$ , and an aligned pillar array (D80S40A), C) the same as B but with a nonaligned pillar array (D80S40N), and D) sample with pillar diameter of 20  $\mu\text{m}$ , spacing of 40  $\mu\text{m}$ , and an aligned pillar array (D20S40A)

Sample	Diameter	Spacing	Alignment	Physical Appearance
D80S20A	80 $\mu\text{m}$	20 $\mu\text{m}$	Aligned	<b>A</b> 
D80S40A	80 $\mu\text{m}$	40 $\mu\text{m}$	Aligned	<b>B</b> 
D80S40N	80 $\mu\text{m}$	40 $\mu\text{m}$	Not-Aligned (45° offset)	<b>C</b> 
D20S40A	20 $\mu\text{m}$	40 $\mu\text{m}$	Aligned	<b>D</b> 

### 2.2.1 Fabrication Method

A SU-8 (epoxy-based negative photoresist) hard template was fabricated using photolithographic processing. SU-8 (acquired from Microchem) was spin-coated with a thickness of 55  $\mu\text{m}$ , and selectively exposed via a photomask for 48 seconds at 15  $\text{mJ}/\text{cm}^2$ . The photomask on a flexible foil was purchased from CAD/Art Service, Inc (Bandon, Oregon), containing 10 x 10  $\text{mm}^2$  arrays of circular holes. The samples were subsequently cured at 65  $^\circ\text{C}$  for 5 min, and cured once more at 95  $^\circ\text{C}$  for 12 min. Followed by cooling down the samples to 55  $^\circ\text{C}$  over a period of 10 minutes. The photoresist was laid to rest for 10 minutes and plasma-flashed afterward to obtain the pattern in the photoresist.

Before use, the SU-8 hard template was coated with a per-fluorosilane coating (from Sigma Aldrich), acting as an anti-stick layer. The silanization agent was dropped on a glass slide, and placed in a desiccator. The wafer was cleaned with oxygen plasma for 3 minutes and placed in the desiccator, which was then evacuated for 2 hours to start gas-phase silanization. Subsequently, the wafer was rinsed with ethanol to remove excess silanization agent.

The silanized SU-8 hard template was used to fabricate pillar arrays from PDMS. The template was cast with uncured PDMS, degassed for 30 minutes, and cured for 2 hours at 68  $^\circ\text{C}$ . The uncured PDMS (Sylgard-184) and curing agent were purchased from Dow Corning (MI, USA). Pre-polymer and curing agent were mixed in a 10:1 weight-based mixing ratio before use.

PDMS was chosen because it is semi-transparent, allowing light to pass through the sample to contrast the particles against the PDMS background.

## 2.3 Experimental Setup

### 2.3.1 Components of the Setup

An optical microscope (Nikon Japan I-UEPI) with a light source of 100 W at 12 V and an optical zoom of 50x were used to track the particle flow. The microscope had a field of view of  $184 \times 230 \mu\text{m}$ , with a theoretical spatial resolution of  $0.42 \mu\text{m}$  [24], [25]. This field of view allowed the camera to capture at least 4 pillars at all times, while keeping the magnification high enough to clearly record the microparticles ( $2 \mu\text{m}$  diameter), referred to as tracers. A separate compact slow-motion camera (Sony Cybershop DSC-RX100 V) was used to capture the motion of the microparticles by recording through the ocular of the microscope. The recording captured images with a resolution of  $1080 \times 1920$  pixels at a rate of 250 frames per second, in a RAW (uncompressed) format. An ISO of 2000 and aperture (F) of 1.8 [26] was used. Six sequential images with the aforementioned settings can be seen in Figure 1.

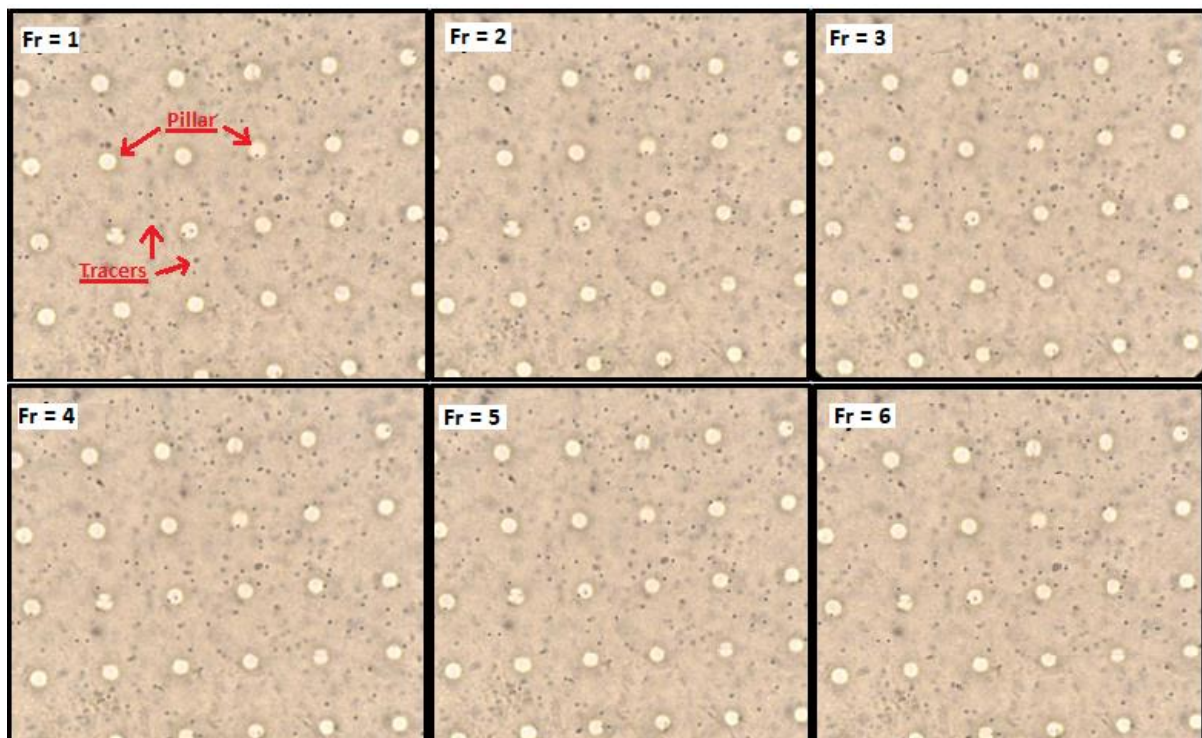


**Figure 1:** A sequence of frames recorded during the experiment of sample type D20S40A where  $t = x$  represents the order of frames (Fr = 1 is the first frame, Fr = 2 is the second frame). The circular white objects are the top of the pillars, while the black dots are the tracers (microparticles) moving through the liquid. In each frame, the tracers had small positional changes which were analyzed by a PIV tool to extract fluid velocity.

Figures 2 and 3 show, respectively, a schematic and a physical representation of the setup from a side view. On the bottom of the entire setup, the light source of the microscope was located. This light source focused the light to go through a hole in the baseplate, the top of which was covered with a glass plate. On top of the glass plate, the sample was located. Above the sample, the substrate was hung. The light passed through the glass, sample, and substrate before reaching the camera connected to the ocular of the microscope. The baseplate was connected to a Micro Positioning Stage (MPS). This MPS allowed movement of the sample, and will henceforth be referred to as MPS-sample. Another MPS was connected to the substrate and will henceforth be called the MPS-substrate. In the setup, the MPS-substrate

was mechanically connected to the MPS-sample by means of the baseplate. The MPS-sample was fixed to a T-slot frame to serve as a stable connection to the ground.

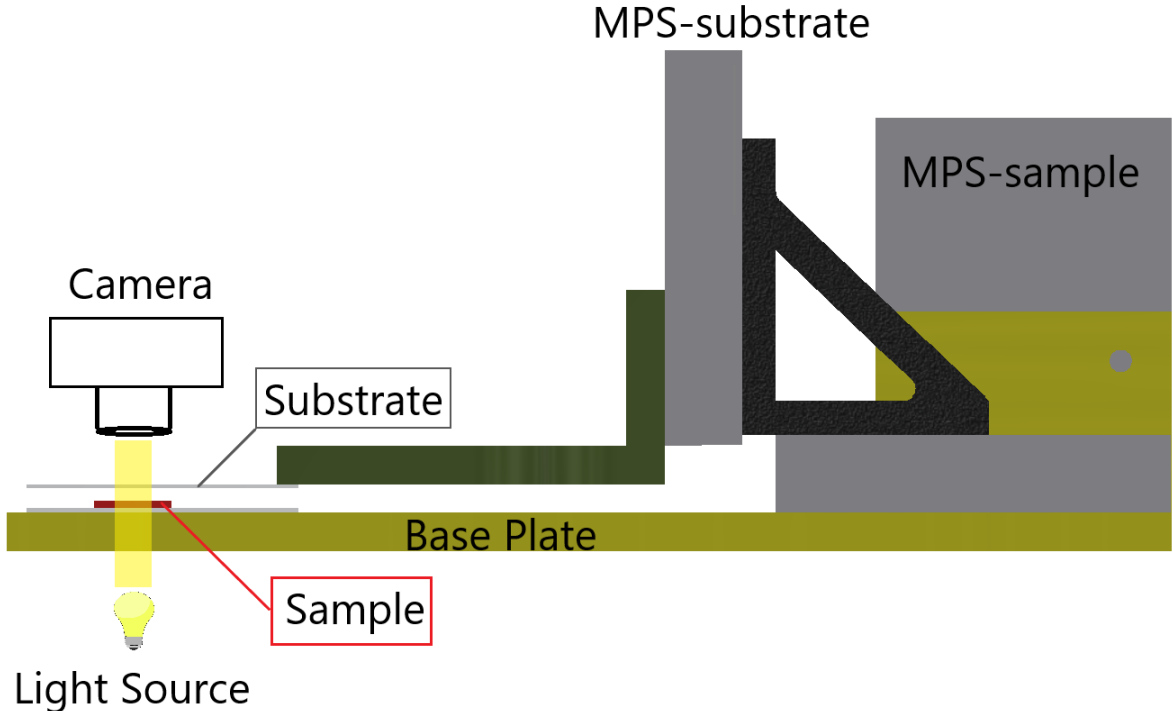


**Figure 2:** Side view of a modeled representation of the setup used for experimentally gathering data. The MPS-sample was connected to the baseplate. The sample lied on top of the baseplate and had a substrate hanging above it. The substrate was attached to the MPS-substrate. The light source went through a hole in the baseplate, through the sample, and the substrate before being recorded by the camera through the ocular of the microscope.

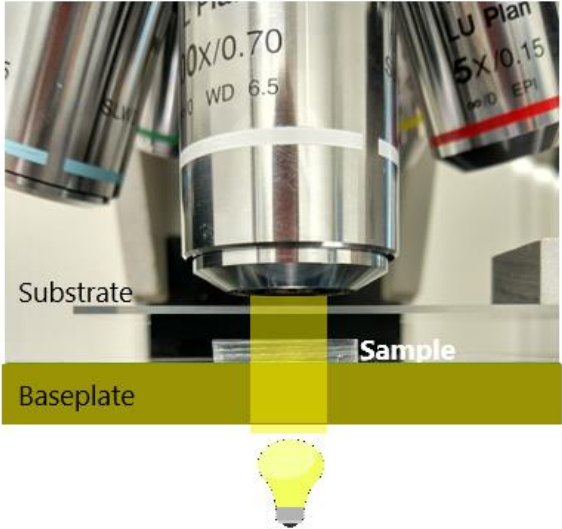


**Figure 3:** Side view picture of the experimental setup described in Figure 2. The light source went through a hole in the baseplate, through the sample, and the substrate, before being recorded by the camera through the ocular of the microscope.

## 2.3.2 Motion of the Setup

The travel direction of the MPS are shown in Figure 4. The MPS-substrate and MPS-sample were mechanically connected. The advantage of this connection was that the MPS-sample could move to change the focus depth without changing the substrate's relative distance from the sample. The substrate could only be moved relative to the sample by the MPS-substrate. Both MPS had their max velocity set to 10  $\mu\text{m/s}$ , max acceleration set to 10  $\mu\text{m/s}^2$ , and no overshoot allowed.

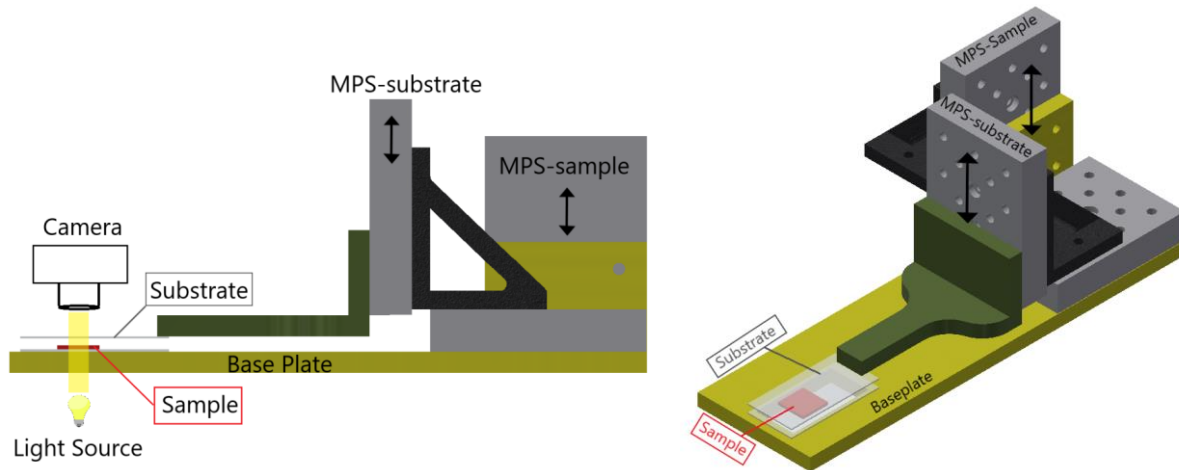


**Figure 4:** (Left) Side view of a modeled representation, as in Figure 3, with arrows indicating the direction the micro-positioning stages can move. (Right) Isometric view of the same representation on the left.

## 2.4 Experimental Procedure

### 2.4.1 Calibration of The Setup

In order to ensure consistency of the MPS position and the predetermined start/end positions, the zero position of the MPS was calibrated every five measurements. First, the sample was removed from the baseplate and the substrate was lowered until a piece of paper (50  $\mu\text{m}$  thick) could no longer slide freely between the substrate and the baseplate. Then, the top substrate was moved up by 10  $\mu\text{m}$  and the MPS-substrate controlling unit moved upwards so that the two substrates were separated by a total of 60  $\mu\text{m}$ ; this position was taken as the zero position.

### 2.4.2 Data Collection

Before each measurement, samples were washed with distilled water and dried with KimWipes in order to remove water, residual particles, or dust. Once the sample was cleaned, the substrate was separated from the baseplate by 7 mm in order to create space for easy placement of the sample. The sample was put on top of the baseplate in a position such that the light of the microscope illuminated the quadrant of the sample closest to a marked corner (Figure 5). Once the quadrant with the marked corner was shown on camera, 200  $\mu\text{L}$  of liquid was deposited on top of the sample using a micropipette (Eppendorf Research Plus). The substrate was then lowered to the starting position 200  $\mu\text{m}$  above the sample by using the MPS-substrate. Finally, the sample was brought into focus by moving the MPS-baseplate to the pre-set position of the corresponding sample type (Figure 5). This pre-set position was determined based on the best focus of the top of the pillars.

The liquid that was deposited on top of the sample contained micro particles. The tracers were acquired from Sigma-Aldrich as an aqueous suspension. They were made out of a carboxylate-modified polystyrene (L3030-1ML), with an excitation/emission of 553/635 nm, a diameter of 2.0  $\mu\text{m}$ , and a density of 1.05E-3 g/mm (Appendix C: Tracer Safety Datasheet). The aquatic suspended particles were diluted with a 1:100 (aqueous suspended particles to water/glycerol) ratio.

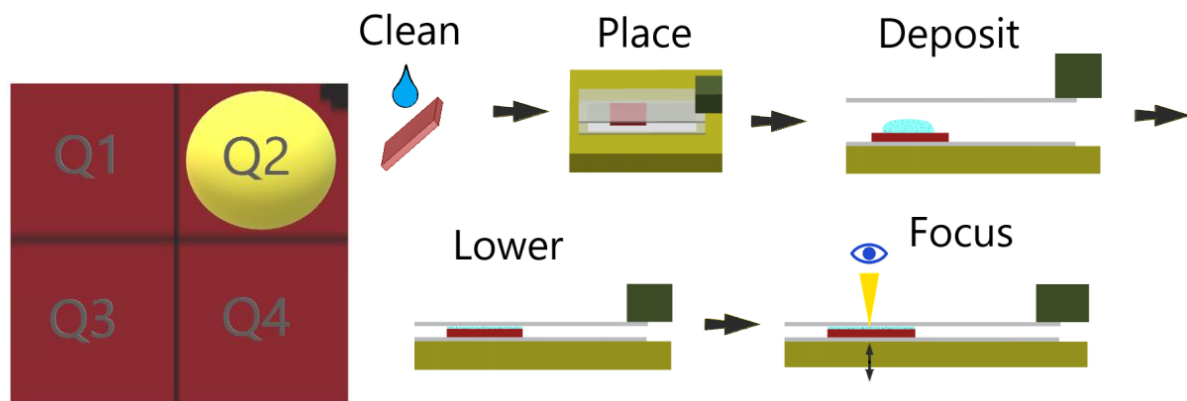


**Figure 5:** (Left) The quadrant illuminated by the light source according to where the black mark in the corner was. (Right) Steps for preparation of the sample before the recording of a measurement started. The first step is to clean the sample, which is then placed under the substrate and on top of the baseplate. Water or glycerol is then deposited on top of the sample. The substrate was subsequently lowered to the starting position, 200  $\mu\text{m}$  away from the top of the sample. Finally, the baseplate is moved up or down in order to bring the top of the pillars of the sample into focus.

After the preparations were made, measurements were conducted according to the following protocol. The MPS-substrate was set to move from its start position at 10  $\mu\text{m/s}$  for 10 seconds. After starting the movement of the substrate, the recording was manually started 2 to 3 seconds later. Approximately 7 seconds after the start of the recording, the recordings stopped in order to give the camera time to process and save the 7 seconds it recorded. Exactly 10 seconds after the MPS-substrate started to move, the MPS-substrate stopped. Once the processing of the recording was finished, the MPS-substrate was initiated to move again for the same duration and at the same speed. The recording was manually started again 2 to 3 seconds after the MPS-substrate restarted. The recording stopped to process the images again after 7 seconds of recording time had passed. Ten seconds since the restart of the MPS-substrate, the end position of that measurement had been reached, and the preparation for the next measurement could start.

Following this approach, a measurement consisted of two recordings, each 7 seconds in length. This meant that 14 seconds were recorded out of the 20 seconds of movement time coming from the MPS-substrate. The first 2 to 3 seconds right after the movement started were lost due to the manual start of the recording. To ensure the recording captured the liquid while the MPS-substrate was moving, the movement time was slightly longer than the time it took to manually start the recording and recording time added together.

The measurements for each sample were taken in a randomized order per liquid type. Per sample, 20 measurements were taken using water and 10 measurements were taken using glycerol as a fluid type. This amounts to a total of 120 measurements taken for all four samples and both fluid types.

### 2.4.3 Quality Inspection

After the recordings were taken, measurements were excluded based upon the recorded quality and particle activity during a recording. The entire measurement was excluded when:

(1) the tracers could not be seen for more than 3 seconds of the recorded duration of a measurement (14 seconds); or (2) when the top of the pillars were out of focus for more than 3 seconds of the measurement's recorded duration; or (3) when no tracer movement was present, that is, when three consecutive snapshots (taken every 1.5 seconds of the measurement) did not visually show any difference in tracer position. A total of 32 out of 120 recorded measurements were removed based on the above criteria.

#### 2.4.4 Image Conversion

All measurements that passed quality inspection were converted into images using "Free Video to JPG Converter" (DVDVideoSoft). For each recorded measurement, every other frame was extracted. This was done because the PIV software could not track the displacement of tracers for every frame due to the low velocity of the tracers and high fps recorded. Once the images were extracted from all recordings, they were imported in MATLAB, cropped to a size of 800 x 800 pixels, and converted into black-white images (Figure 6). The MATLAB code converted each pixel to black or white depending on whether or not the pixel value was above a predefined threshold. After the conversion, the images were saved and numbered sequentially (1<sup>st</sup> image = 1, 2<sup>nd</sup> image = 2 ...) (Appendix B: MATLAB code).

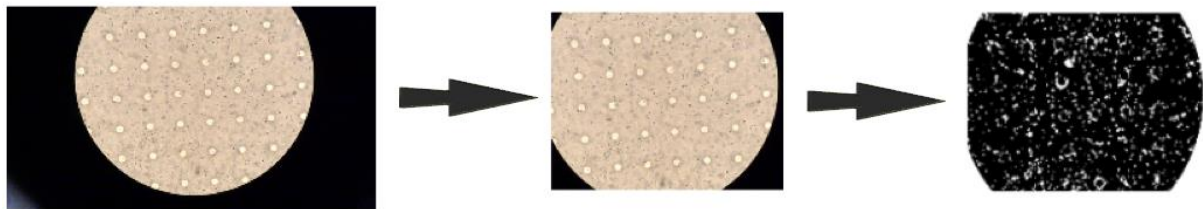


**Figure 6:** Image conversion steps done by MATLAB before being imported into PIVLab. The original frame extracted from the video recording (left) was cropped into an 800 x 800 pixel image (middle) before being converted into a black-white image (right). These frames were then automatically saved in sequential order.

#### 2.4.5 PIV Analysis

In a literature review that preceded this thesis (Appendix D: Literature Review), fluidic flow measurement methods were categorized based on their spatial and temporal resolution, and their level of invasiveness. Invasiveness was defined as the physical interference of the measurement method on the situation of interest. Less invasive methods were arguably preferred as they can capture the natural (unobstructed) flow of interest. The results of the review showed that the spatial and temporal resolution of the methods increased while the invasiveness of the methods decreased over the years. Particle Image Velocimetry (PIV) was chosen as the most suitable method to analyze the movement between subsequent images (Figure 7). PIV was chosen for its limited distortion of the flow, capacity to capture micrometer-sized objects, and its proven reliability under various conditions such as liquids, gases, different pressures and temperatures [27]–[29]. In PIV, particles moving in a fluid, were recorded and had their velocity estimated as a proxy of fluid velocity.

The PIV analysis was done with an open-access MATLAB script called PIVLab [30]. PIVLab standard settings were used, such as dividing pictures into sections of 32 x 32 pixels, a linear window deformation interpolation, and a Rankine Vortex flow simulation setting. To track the mean particle displacement within that section, each 32 x 32 pixel section, was compared to the same section of the next frame. After the direction of motion was determined, a displacement vector was put in the middle of that section representing the displacement of the entire 32 x 32 pixel section. The comparison of these sections started at the top left corner of the two images. After that section between the first and the second frame were compared, the center of the section moved 16 pixels to the right and the new 32 x 32 pixel section was compared with the corresponding section in the next frame. When the analyzed section

reached the right side of the picture, the following analyzed section was on the left side again but 16 pixels lower than the previously analyzed section. This continued until the last section finished analyzing was located in the bottom right corner. The software then moved to the next two consecutive frames in order to analyze their particle displacement and represent it with a displacement vector. This process was repeated until the particle displacement of all imported frames regarding a measurement were analyzed.

In order to analyze the differences in flow direction over time, the results of the analysis done by PIVLab, were split up in 4 phases (i.e., each of the two 7-second recordings per measurement was split into two phases). Phase 1 corresponded to the first 3.5 seconds of the 1<sup>st</sup> recording, Phase 2 corresponded to the last 3.5 seconds of the 1<sup>st</sup> recording, Phase 3 corresponded to the first 3.5 seconds of the 2<sup>nd</sup> recording, and Phase 4 corresponded to the final 3.5 seconds of the 2<sup>nd</sup> recording. The analyzed result for these phases were then used for the statistical analysis.

The analyzed frames of each phase had one vector that represented the mean of all calculated vectors of the frames belonging to that phase. The magnitudes (velocities) of these vectors for each of the 4 phases of a measurement were manually saved and used for analysis.

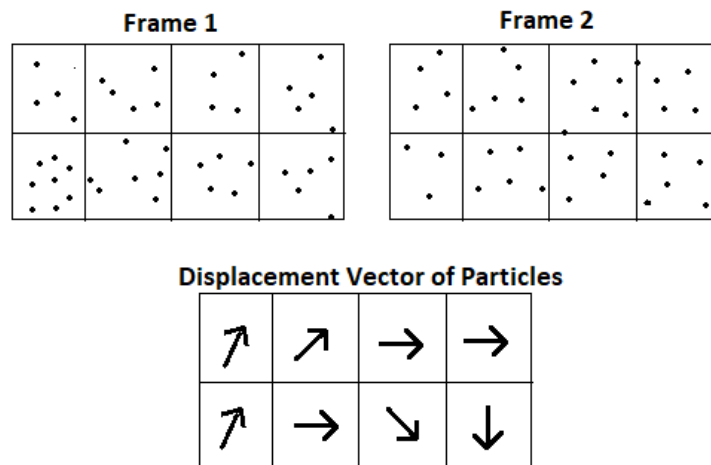


**Figure 7:** The PIV software splits each frame into about 2500 sections, the same section in Frame 1 and Frame 2 were then analyzed. Displacement per section of all particles was determined and represented by a single vector. Afterward, all vectors were averaged into one mean vector per phase and per sample.

### 2.4.6 Statistical Analysis

The mean velocities were grouped per phase and sample type and were compared according to the variables of interest mentioned in Section 2.1 using independent two-tailed t-tests. The effect of the pillar diameter on fluid velocity was investigated by comparing the 4 phases (combined and individually) from sample D20S40A and D80S40A. The effect of the pillar spacing on fluid velocity was investigated by comparing the 4 phases (combined and individually) from sample D80S20A and D80S40A. The effect of alignment on fluid velocity was investigated by comparing the 4 phases (combined and individually) from sample D80S40N and D80S40A. The effect of fluid type on fluid velocity was investigated by comparing the results of the four samples (combined phases) for water versus glycerol. The effect of time on drainage was investigated by comparing the 4 phases for each of the samples using a repeated measures ANOVA (analysis of variance) (Appendix B: MATLAB code). Considering the relatively large number of statistical comparisons, a strict alpha value of 0.001 was used.

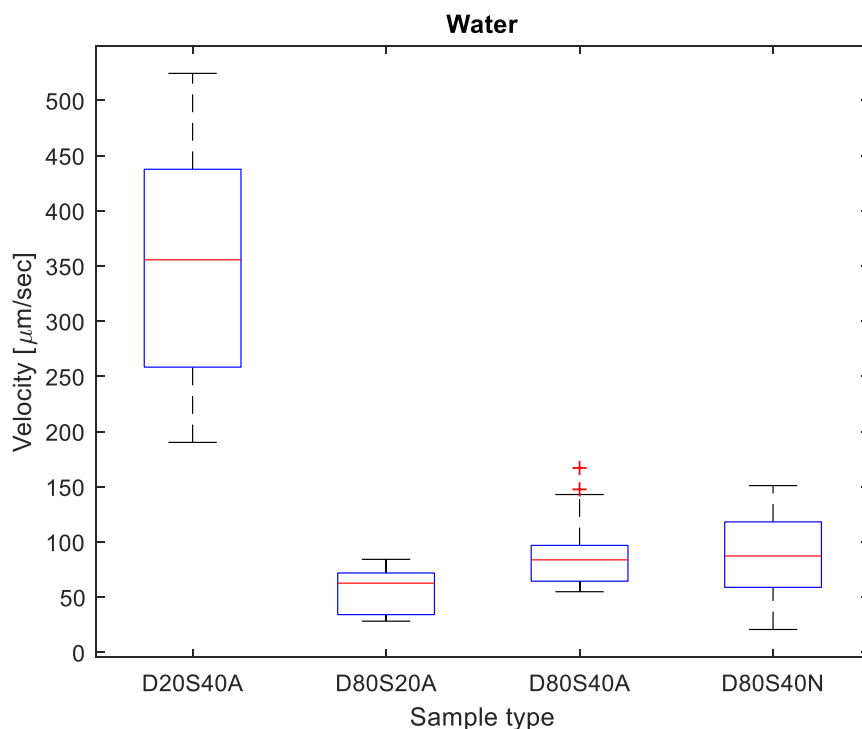


### 3. Results

In this section, we presented the experimental results regarding the effect of pillar diameter, pillar spacing, and pillar alignment on fluid velocity in the presence of water or glycerol. The average fluid velocity per phase, sample, and fluid type can be found in Appendix A.

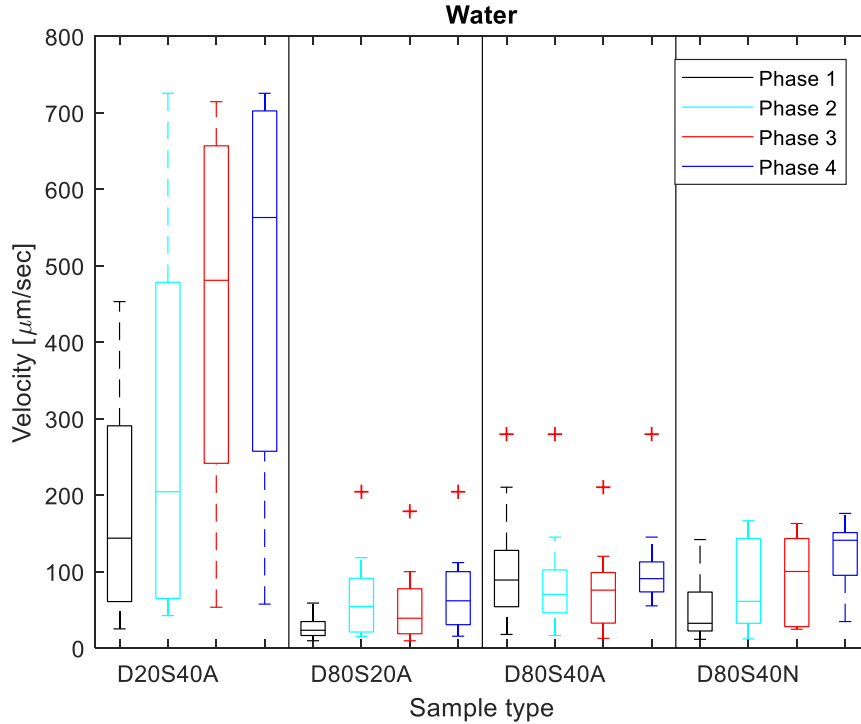
#### 3.1 Water as a Fluid Type

Figure 8 shows the fluid velocity of each sample type in the presence of water across all four phases. It can be seen that the mean and standard deviation for sample type D20S40A were much larger than for the other sample types.



**Figure 8:** Fluid velocity [ $\mu\text{m}/\text{sec}$ ] of all phases grouped together for each sample in the presence of water. The sample size ( $N$ ) expressed in number of measurements were 15 for D20S40A, 14 for D80S20A, 16 for D80S40A, and 12 for D80S40N.

Figure 9 shows the fluid velocity for each sample type in the presence of water for all four phases. It can be seen that the mean fluid velocity for D20S40A was consistently higher than that for the other geometries for all four phases.



**Figure 9:** Fluid velocity [ $\mu\text{m}/\text{sec}$ ] per sample for each of the four phases separately and water as a fluid. The sample size ( $N$ ) for each of the phases expressed in number of measurements were 15 for D20S40A, 14 for D80S20A, 16 for D80S40A, and 12 for D80S40N.

Table 2 shows the mean ( $M$ ) and standard deviation ( $SD$ ) of each sample type per phase. It can be seen that the variation for each of the measurements were quite high, with the standard deviation being at least half the amount of the mean value.

**Table 2:** Means ( $M$ ) and standard deviations ( $SD$ ) of fluid velocity for each sample type per phase for water, where  $M$  is the mean,  $SD$  is the standard deviation, in  $\mu\text{m}/\text{sec}$ . The sample size ( $N$ ) for each of the phases expressed in number of measurements were 15 for D20S40A, 14 for D80S20A, 16 for D80S40A, and 12 for D80S40N.

	D20S40A		D80S20A		D80S40A		D80S40N	
	$M$	$SD$	$M$	$SD$	$M$	$SD$	$M$	$SD$
Phase 1	190.65	151.11	28.91	16.04	98.98	69.12	52.58	46.33
Phase 2	304.23	241.68	65.54	52.66	83.15	63.11	80.57	57.41
Phase 3	434.56	225.11	53.41	45.90	75.20	50.10	92.73	58.70
Phase 4	495.85	245.75	71.66	49.32	104.05	52.55	123.04	44.10

Table 3 shows the  $t$ - and  $p$ -values of the difference in fluid velocity due to diameter, spacing, and alignment, across all four phases. Diameter was found to have a significant effect on fluid velocity ( $t(29) = 9.41$ ,  $p < 0.001$ ), with the smaller diameter sample (D20S40A) exhibiting a significantly higher fluid velocity than the larger diameter sample (D80S40A). A larger spacing was not proven to have a significantly higher fluid velocity than a narrower spacing (D80S40A vs D80S20A:  $t(28) = 3.38$ ,  $p = 2.127\text{E-}3$ ). The effect of pillar alignment on fluid velocity (D80S40A vs. D80S40N) was not significant ( $t(26) = 0.23$ ,  $p = 0.823$ ).

Table 4 shows the  $t$ - and  $p$ -values of the difference in fluid velocity due to diameter, spacing, and alignment, per phase. A smaller diameter did not have a significantly higher fluid velocity for the first phase (Phase 1:  $t(29) = 2.20$ ,  $p = 0.036$ ). The other three phases did exhibit a significantly higher fluid velocity for the sample with the larger diameter (Phase 2:  $t(29) = 3.53$ ,  $p = 0.001$ ; Phase 3:  $t(29) = 6.23$ ,  $p < 0.001$ ; Phase 4:  $t(29) = 6.23$ ,  $p < 0.001$ ). A larger spacing

did exhibit a significantly higher fluid velocity in Phase 1 ( $t(28) = 3.70, p = 0.001$ ), but not in the other three phases (Phase 2:  $t(28) = 0.82, p = 0.417$ ; Phase 3:  $t(28) = 1.24, p = 0.227$ ; Phase 4:  $t(28) = 1.73, p = 0.094$ ). The effect of alignment on fluid velocity was not significant in any of the phases (Phase 1:  $t(26) = 2.01, p = 0.055$ ; Phase 2:  $t(26) = 0.11, p = 0.912$ ; Phase 3:  $t(26) = 0.85, p = 0.402$ ; Phase 4:  $t(26) = 1.01, p = 0.321$ ).

**Table 3:** The effect of diameter, spacing, and alignment on drainage, for water ( $t$ - and  $p$ -values). The sample size ( $N$ ) expressed in number of measurements were 31 for diameter, 30 for spacing, and 28 for alignment.

	$df$	$t$	$p$
Diameter	29	9.41	2.603E-10
Spacing	28	3.38	2.127E-3
Alignment	26	0.23	0.823

**Table 4:** Differences between the effect of diameter, spacing, and alignment on drainage per sample type for each of the four phases, with water used as a liquid medium ( $t$ - and  $p$ -values). The sample size ( $N$ ) for all phases per sample expressed in number of measurements were 31 for diameter, 30 for spacing, and 28 for alignment.

	Diameter			Spacing			Alignment		
	$df$	$t$	$p$	$df$	$t$	$p$	$df$	$t$	$p$
Phase 1	29	2.20	0.036	28	3.70	0.001	26	2.01	0.055
Phase 2	29	3.53	0.001	28	0.82	0.417	26	0.11	0.912
Phase 3	29	6.23	8.500E-7	28	1.24	0.227	26	0.85	0.402
Phase 4	29	6.23	8.408E-7	28	1.73	0.094	26	1.01	0.321

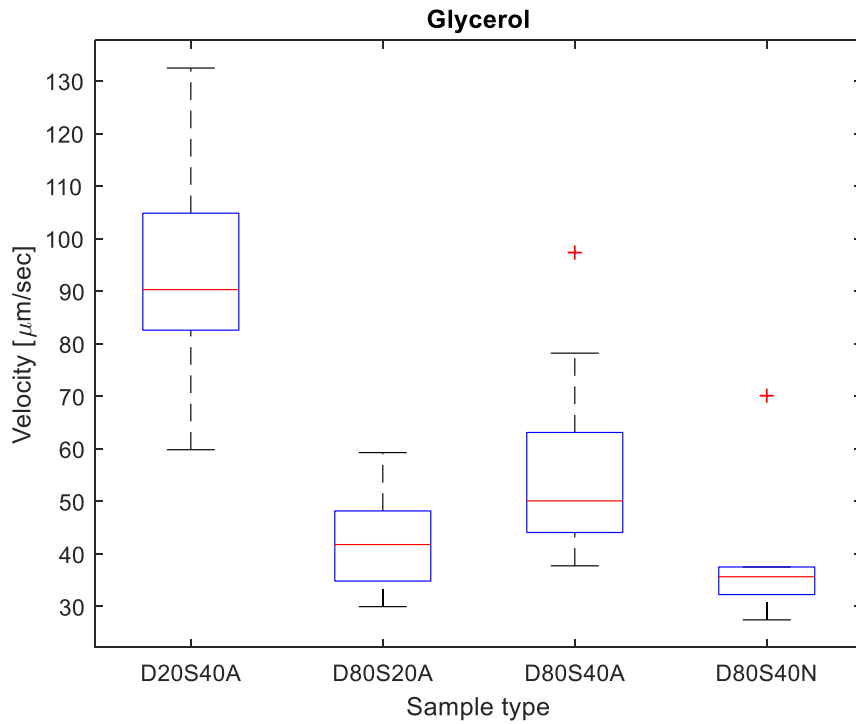
Table 5 shows the  $F$ - and  $p$ -values from a repeated measures ANOVA between the four phases per sample. The change over time is proxied by the change between the phases. The effect of time on drainage did not significantly differ from each other for any of the samples.

**Table 5:** The effect of time (phases) on drainage ( $F$ - and  $p$ -values) per sample type for water. The sample size ( $N$ ) expressed in number of measurements were 15 for D20S40A, 14 for D80S20A, 16 for D80S40A, and 12 for D80S40N.

	$df$	$F$	$p$
D20S40A	56	2.79E+5	1.594E-3
D80S20A	52	5002.80	0.059
D80S40A	60	2899.70	0.484
D80S40N	44	10229.00	0.016

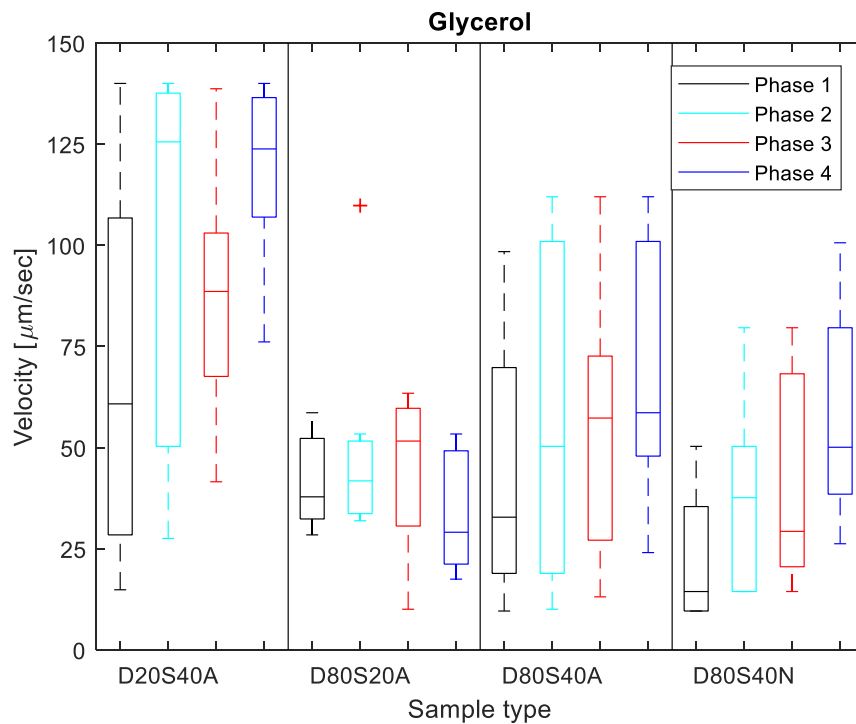
## 3.2 Glycerol as a Fluid Type

Figure 10 shows the fluid velocity of each sample type in the presence of glycerol across all four phases. The mean and standard deviation for sample D20S40A were much larger than for the other samples.



**Figure 10:** Fluid velocity [ $\mu\text{m}/\text{sec}$ ] of all phases grouped together for each sample in the presence of glycerol. The sample size ( $N$ ) expressed in number of measurements were 8 for D20S40A and D80S20A, 9 for D80S40A, and 6 for D80S40N.

Figure 11 shows the fluid velocity of each sample type in the presence of glycerol for each of the 4 phases. Across all four phases, the mean fluid velocity for D20S40A was consistently higher than the mean fluid velocity for the other samples.



**Figure 11:** Fluid velocity [ $\mu\text{m}/\text{sec}$ ] per sample for each of the four phases separately and glycerol as a fluid. The sample size ( $N$ ) for each of the phases expressed in number of measurements were 8 for D20S40A and D80S20A, 9 for D80S40A, and 6 for D80S40N.

Table 6 shows the mean ( $M$ ) and standard deviation ( $SD$ ) of the sales per phase. The standard deviation for each of the measurements were quite high, with the standard deviation being at least half the amount of the mean value. Except Phase 3 and Phase 4 of D20S40A and Phase 1 of D80S20A, for which the standard deviation was much lower than half the corresponding mean.

**Table 6:** Mean and standard deviation of fluid velocity for each sample type per phase for glycerol, where  $M$  is the mean,  $SD$  is the standard deviation, in  $\mu\text{m}/\text{sec}$ . The sample size ( $N$ ) for all phases per sample expressed in number of measurements were 8 for D20S40A and D80S20A, 9 for D80S40A, and 6 for D80S40N.

	D20S40A		D80S20A		D80S40A		D80S40N	
	$M$	$SD$	$M$	$SD$	$M$	$SD$	$M$	$SD$
Phase 1	68.36	46.58	41.51	11.45	44.58	31.24	22.31	16.75
Phase 2	99.31	48.14	49.49	25.84	58.19	40.58	39.01	25.65
Phase 3	87.34	30.40	44.68	19.17	52.99	32.47	40.25	27.21
Phase 4	118.84	22.14	33.74	14.71	69.32	30.60	57.53	27.56

Table 7 shows the  $t$ - and  $p$ -values of the difference in fluid velocity due to diameter, spacing, and alignment, across all four phases. None of these variables were found to have a significant effect on fluid velocity (Diameter:  $t(15) = 3.74$ ,  $p = 1.967\text{E-}3$ ; Spacing:  $t(15) = 1.83$ ,  $p = 0.086$ ; Alignment:  $t(13) = 1.75$ ,  $p = 0.104$ ).

Table 8 shows the  $t$ - and  $p$ -values of the difference in fluid velocity due to diameter, spacing, and alignment, per phase. Diameter did not have a significantly effect on fluid velocity for any of the phases (Phase 1:  $t(15) = 1.25$ ,  $p = 0.230$ ; Phase 2:  $t(15) = 1.91$ ,  $p = 0.075$ ; Phase 3:  $t(15) = 2.24$ ,  $p = 0.040$ ; Phase 4:  $t(15) = 3.78$ ,  $p = 1.828\text{E-}3$ ). The effect of spacing on fluid velocity was not significant either (Phase 1:  $t(15) = 0.26$ ,  $p = 0.797$ ; Phase 2:  $t(15) = 0.52$ ,  $p = 0.611$ ; Phase 3:  $t(15) = 0.63$ ,  $p = 0.537$ ; Phase 4:  $t(15) = 2.99$ ,  $p = 0.009$ ). The effect of alignment on fluid velocity was not significant in any of the 4 phases (Phase 1:  $t(13) = 1.59$ ,  $p = 0.136$ ; Phase 2:  $t(13) = 1.02$ ,  $p = 0.325$ ; Phase 3:  $t(13) = 0.79$ ,  $p = 0.443$ ; Phase 4:  $t(13) = 0.76$ ,  $p = 0.461$ ).

**Table 7:** The effect of diameter, spacing, and alignment on drainage, for glycerol ( $t$ - and  $p$ -values). The sample size ( $N$ ) expressed in number of measurements were 17 for diameter and spacing, and 15 for alignment.

	$df$	$t$	$p$
Diameter	15	3.74	1.967E-3
Spacing	15	1.83	0.086
Alignment	13	1.75	0.104

**Table 8:** Differences between the effect of diameter, spacing, and alignment on drainage per sample type for each of the four phases, with glycerol used as a liquid medium ( $t$ - and  $p$ -values). The sample size ( $N$ ) for each of the phases expressed in number of measurements were 17 for diameter and spacing, and 15 for alignment.

	Diameter			Spacing			Alignment		
	$df$	$t$	$p$	$df$	$t$	$p$	$df$	$T$	$p$
Phase 1	15	1.25	0.230	15	0.26	0.797	13	1.59	0.136
Phase 2	15	1.91	0.075	15	0.52	0.611	13	1.02	0.325
Phase 3	15	2.24	0.040	15	0.63	0.537	13	0.79	0.443
Phase 4	15	3.78	1.828E-3	15	2.99	0.009	13	0.76	0.461

Table 9 shows the  $F$ - and  $p$ -values from a repeated measures ANOVA between the four phases per sample type. The time (proxied by the four phases) does not significantly affect fluid velocity for any of the samples (D20S40A:  $t(28) = 3588.60$ ,  $p = 0.086$ ; D80S20A:  $t(28) = 349.98$ ,  $p = 0.402$ ; D80S40A:  $t(32) = 964.47$ ,  $p = 0.484$ ; D80S40N:  $t(20) = 1242.10$ ,  $p = 0.141$ ).

**Table 9:** The effect of time (phases) on drainage ( $F$ - and  $p$ -values) per sample type for glycerol. The sample size ( $N$ ) expressed in number of measurements were 8 for D20S40A and D80S20A, 9 for D80S40A, and 6 for D80S40N.

	$df$	$F$	$p$
D20S40A	28	3588.60	0.086
D80S20A	28	349.98	0.402
D80S40A	32	964.47	0.484
D80S40N	20	1242.10	0.141

### 3.3 Fluid Type Effect

Table 10 shows the  $t$ - and  $p$ -values of the difference in fluid velocity due to fluid type for each of the samples. Fluid type was found to have a significant effect on fluid velocity for sample D20S40A ( $t(21) = 6.77$ ,  $p < 0.001$ ), whereas the effect of fluid type was not significant for the other three samples (D80S40A:  $t(20) = 1.63$ ,  $p = 0.118$ ; D80S20A:  $t(23) = 2.73$ ,  $p = 0.012$ ; D80S40N:  $t(16) = 2.87$ ,  $p = 0.011$ ).

**Table 10:** Effect of fluid type on drainage for each sample type ( $t$ - and  $p$ -values). The sample size ( $N$ ) expressed in number of measurements were 24 for D20S40A, 22 for D80S20A, 25 for D80S40A, and 18 for D80S40N.

	$df$	$t$	$P$
D20S40A	21	6.77	1.073E-6
D80S20A	20	1.63	0.118
D80S40A	23	2.73	0.012
D80S40N	16	2.87	0.011

## 4. Discussion

### 4.1 Effect of Diameter on Drainage

Our results showed that pillar diameter had a significant effect on fluid velocity, thus drainage, for water. A similar trend was observed for glycerol, but the effect was not statistically significant. Per phase, the effect of diameter on fluid velocity was significant for 3 out of the 4 phases for water. When expressing the findings in % channel volume change, it showed that a larger % channel volume resulted in larger fluid velocities, thus faster drainage.

According to previous research [5], when  $r < \frac{R}{\sqrt{n}}$ , where  $r$  is the radius of the pillar,  $R$  is the radius of the entire wet adhesive, and  $n$  is the number of pillars, drainage would be  $n$  times faster. In our experiment, the samples were 10 x 10 mm (= 10000 x 10000  $\mu\text{m}$ ) and can contain  $\left(\frac{\text{sample width}}{\text{diameter pillar} + \text{pillar spacing}}\right)^2 = \left(\frac{10000}{20+40}\right)^2 = 166^2$  pillars for D20S40A and  $\left(\frac{\text{sample width}}{\text{diameter pillar} + \text{pillar spacing}}\right)^2 = \left(\frac{10000}{80+40}\right)^2 = 83^2$  pillars for D80S40. When applying the condition  $r < \frac{R}{\sqrt{n}}$  to our results, we get  $20 < \frac{10000}{\sqrt{166^2}} = 60.24$  for D20S40A and  $80 < \frac{10000}{\sqrt{83^2}} = 120.48$  for D80S40A, meaning that both samples fulfilled the requirement. Since  $n$  differed by a factor of 2 (166 vs 83), drainage was theoretically expected to change by a factor of 2. According to our experimental results, the effect of diameter on drainage was a factor of 9.41 in the case of water, and 3.74 in case of glycerol. The large deviance between the theoretical and the experimental increase could be due to the limitations of the experiment (section 4.5).

### 4.2 Effect of Spacing on Drainage

The effect of pillar spacing on drainage was not statistically significant for water nor glycerol, albeit a trend of faster drainage with a large spacing was observed for water. A positive effect of a larger spacing on water drainage was further observed at the first phase of the measurements. When looking at the effect of spacing based on the % channel volume, increasing the channel width resulted in an increase in % channel volume. Based on the findings from section 4.1, an increase in channel volume would result in more drainage. The opposing expectations from % channel volume and the experimental results confirmed that more accurate measurements are needed.

According to previous research [5], when  $r < \frac{R}{\sqrt{n}}$ , drainage would be  $n$  times faster. For sample D80S20A:  $80 < \frac{10000}{\sqrt{100^2}} = 100$  and D80S40A:  $80 < \frac{10000}{\sqrt{83^2}} = 120.48$ . Both samples were fulfilling the condition  $r < \frac{R}{\sqrt{n}}$ . Since  $n$  differed by a factor of 0.2 (100 vs 83), it meant that drainage was theoretically expected to change by a factor of 0.2. According to the results, the effect of diameter on drainage was significant and had a factor of 3.38 in the case of water. In case of glycerol, the results were not significant and had a difference with a factor of 1.83. The difference between the theoretical and the experimental factor could be due to the limitations of the experiment (section 4.5).

### 4.3 Effect of Alignment on Drainage

The results regarding the effect of pillar alignment on drainage were not significant for neither water nor glycerol. When looking at the phases individually, no significant effect was found

either. These results are consistent with the fact that the % channel volume remains the same for both alignments, thereby drainage was expected to remain unchanged.

In previous research [5], when  $r < \frac{R}{\sqrt{n}}$ , drainage would be  $n$  times faster. The number of pillars ( $n$ ), the pillar diameter ( $r$ ), and the overall sample diameter ( $R$ ) all remain the same. This shows that theoretically, drainage was unaffected by the changes in pillar alignment. Our results are consistent with that for both types of fluids tested.

## 4.4 Effect of Fluid Type on Drainage

The effect of fluid type on drainage was investigated by comparing the results for water and glycerol as a liquid medium for the 4 sample types. Only D20S40A showed a significant effect. Considering that three out of the four samples showed no significant effect of fluid type on fluid velocity, it is likely that viscosity has a limited effect on drainage.

Viscosity was defined as a property defining the rate of resistance against deformation. Since flow close to the moving substrate needed some time to translate flow to the layers farther away from the substrate. It stands to reason that a higher viscosity would result in slower drainage due to this resistance and flow delay. Previous research also mentioned that less viscous fluid should lead to faster drainage [5], which is not the case in our experiments. More measurements would be needed with more fluid types. Other factors such as cohesion or surface tension could also be influencing these results.

## 4.5 Limitations

One of the limitations of our measurement method was that only tracers moving above the pillars (far-field flow region) of the sample were captured. No recordings were made in-between the pillars, giving no indication about the flow and drainage in these areas. According to Gupta [30], drainage occurs in 3 regions, the near-, far-, and intermediate regions depending on how far the adhesive is from the substrate. During this thesis, we only focused on the far-field, and therefore cannot determine anything about the other flow field regions. Future research could expand the current work by investigating the near- and intermediate field.

A second restriction was that the recorded time and the time the substrate approached the sample were not the same for all measurements, due to manually having to initiate the recording and the MPS movement. These small deviations in activation time of the recording limited the consistency of the recorded data. For each measurement, there were two recordings, because the camera was able to only record 7 seconds at 250 fps. In future experiments, it would be beneficial if the entire 20 seconds are recorded without stop, and if the recording start and stop would be synchronized to the MPS-substrate's movements. Several other limitations of this experiment include the squared geometry instead of circular shape of the samples, the manual cleaning and placement of the sample, the limited accuracy of the MPS, and the fluidic compatibility with the glass substrate. The square samples deviated from the typically circular samples used in previous research. The manual cleaning and placement of the sample, while done in the same manner each time, cannot guarantee that all residual tracers or dust is removed, nor that the camera captures the exact same location. Clogging between the pillars, or tracers being stuck at the bottom of the sample could have altered the flow dynamics of the sample. Only the quadrant was taken into account when placing the sample. The start and stop positions of the MPS, were controlled with a positional accuracy of  $5.0 \mu\text{m}$  [31]. Finally, the glass slides repelled water and caused water to gather towards one point. When water was squeezed between the substrate and the sample, the point where water gathers could no longer be in-between the sample and substrate. Having



water located away from the substrate and sample caused water to have a preference of flowing towards that point instead of radially outward.

A final restriction of the experiment was the number of samples used. Since only 4 samples were used in the experiments, a defect that went undetected, or a defect created during the experiment, would influence the results. In further experiments, multiple replicas of the same sample type should be used in order to improve the reliability of the measurements.

## 5. Conclusion

In this thesis, we investigated the effect of pillar diameter, pillar spacing, pillar alignment, and fluid type on drainage. We found that pillar diameter has a significant effect on drainage, regardless of the fluid type. The acquired data were insufficient to draw a conclusion with respect to the effect of the pillar spacing. Pillar alignment did not affect drainage. The findings of the geometrical features were partially in line with previous research for pillar diameter and pillar alignment. The effect of fluid type on drainage is limited.

Due to the limitation of the setup, the results were limited to a 2-dimensional representation of the flow and large deviation occurred during the recording of the measurements or PIV analysis. It is recommended that future research gathers more data and uses multiple copies of a specific sample type. Experimental results can then be compared with simulated data in order to understand the motion not only parallel to the substrate but also in a 3-dimensional setting (flow towards and away from the substrate) in order to verify their findings, and extrapolate it for a more complete analysis.

# References

- [1] V. Radhakrishnan, "Locomotion: dealing with friction.," *Proc. Natl. Acad. Sci. U. S. A.*, vol. 95, no. 10, pp. 5448–55, May 1998.
- [2] D.-M. Drotlef, L. Stepien, M. Kappl, W. J. P. Barnes, H.-J. Butt, and A. del Campo, "Insights into the adhesive mechanisms of tree frogs using artificial mimics," *Adv. Funct. Mater.*, vol. 23, no. 9, pp. 1137–1146, Mar. 2013.
- [3] R. Gupta and J. Fréchet, "Measurement and scaling of hydrodynamic interactions in the presence of draining channels," *Langmuir*, vol. 28, no. 41, pp. 14703–14712, Oct. 2012.
- [4] H. Chen, L. Zhang, D. Zhang, P. Zhang, and Z. Han, "Bioinspired surface for surgical graspers based on the strong wet friction of tree frog toe pads," *ACS Appl. Mater. Interfaces*, vol. 7, no. 25, pp. 13987–13995, Jul. 2015.
- [5] W. Federle, W. J. P. Barnes, W. Baumgartner, P. Drechsler, and J. M. Smith, "Wet but not slippery: Boundary friction in tree frog adhesive toe pads.," *J. R. Soc. Interface*, vol. 3, no. 10, pp. 689–97, Oct. 2006.
- [6] "Drainage | Definition of drainage by Merriam-Webster." [Online]. Available: <https://www.merriam-webster.com/dictionary/drainage>. [Accessed: 08-Apr-2019].
- [7] G. Maycock, "Second paper: Studies on the skidding resistance of passenger-car tyres on wet surfaces," *Proc. Inst. Mech. Eng. Automob. Div.*, vol. 180, no. 1, pp. 122–157, Jan. 1965.
- [8] D. F. Moore, "Prediction of skid-resistance gradient and drainage characteristics for pavements," *Highw. Res. Rec.*, no. 131, 1966.
- [9] B. N. J. Persson, "Biological adhesion for locomotion: Basic principles," *J. Adhes. Sci. Technol.*, vol. 21, no. 12–13, pp. 1145–1173, Jan. 2007.
- [10] "Tire tread having drainage chambers," Sep. 1972.
- [11] J. Shintake, V. Cacucciolo, D. Floreano, and H. Shea, "Soft robotic grippers," *Adv. Mater.*, vol. 30, no. 29, p. 1707035, Jul. 2018.
- [12] C. Morio, A. Bourrelly, L. Sissler, and N. Gueguen, "Perceiving slipperiness and grip: A meaningful relationship of the shoe-ground interface," *Gait Posture*, vol. 51, pp. 58–63, Jan. 2017.
- [13] G. Hanna, W. Jon, and P. Barnes, "Adhesion and detachment of the toe pads of tree frogs," 1991.
- [14] A. C. Noel and D. L. Hu, "The tongue as a gripper.," *J. Exp. Biol.*, vol. 221, no. Pt 7, p. jeb176289, Apr. 2018.
- [15] P. Glass, H. Chung, N. R. Washburn, and M. Sitti, "Enhanced reversible adhesion of dopamine methacrylamide-coated elastomer microfibrillar structures under wet conditions," *Langmuir*, vol. 25, no. 12, pp. 6607–6612, Jun. 2009.
- [16] D. M. Green, "Adhesion and the toe-pads of treefrogs," *Copeia*, vol. 1981, no. 4, p. 790, Dec. 1981.
- [17] D. M. Green and J. Carson, "The adhesion of treefrog toe-pads to glass: Cryogenic examination of a capillary adhesion system," *J. Nat. Hist.*, vol. 22, no. 1, pp. 131–135, Feb. 1988.
- [18] D. M. Green, "Treefrog toe pads: Comparative surface morphology using scanning electron microscopy," *Can. J. Zool.*, vol. 57, no. 10, pp. 2033–2046, Oct. 1979.
- [19] U. Welsch, V. Storch, and W. Fuchs, "The fine structure of the digital pads of rhacophorid tree frogs," *Cell Tissue Res.*, vol. 148, no. 3, pp. 407–416, Apr.

- 1974.
- [20] W. McAllister, A. C.-A. Zoology, and undefined 1983, "Comparison of toe pads of some southern African climbing frogs," *ajol.info*.
  - [21] D. Green, M. S.-A. journal of Zoology, and U. 1986, "Digital microstructure in ecologically diverse sympatric microhylid frogs, genera *Cophixalus* and *Sphenophryne* (Amphibia, Anura), from Papua-new-Guinea," *CSIRO*.
  - [22] I. Hertwig, U. S.- Copeia, and U. 1995, "Comparative toe pad morphology in marsupial frogs (Genus *Gastrotheca*): Arboreal versus ground-dwelling species," *JSTOR*.
  - [23] V. Mizuhira, "The digital pads of rhacophorid tree-frogs," *J. Electron Microsc. (Tokyo)*, vol. 53, no. 1, pp. 63–78, Mar. 2004.
  - [24] X. Chen, B. Zheng, and H. Liu, "Optical and digital microscopic imaging techniques and applications in pathology," *Anal. Cell. Pathol. (Amst)*, vol. 34, no. 1–2, pp. 5–18, 2011.
  - [25] M. W. Davidson, "Resolution | MicroscopyU." [Online]. Available: <https://www.microscopyu.com/microscopy-basics/resolution>. [Accessed: 10-Dec-2018].
  - [26] "Sony RX100 V advanced manual with tips and tricks," <https://www.wimarys.com/>.
  - [27] S. Watanabe and H. Kato, "Stereo PIV applications to large-scale low-speed wind tunnels," 2003.
  - [28] L. Liang, S. Hui, S. Zhao, Q. Zhou, T. Xu, and Q. Zhao, "Cold modeling investigation of aerodynamic characteristics of an arch-fired boiler on particle image velocimetry (PIV): Influence of momentum flux ratio of arch air to secondary air and secondary air angle," *Exp. Therm. Fluid Sci.*, vol. 42, pp. 240–247, Oct. 2012.
  - [29] G. L. Morrison, I. Budihardjo, and M. Behnia, "Measurement and simulation of flow rate in a water-in-glass evacuated tube solar water heater," *Sol. Energy*, vol. 78, no. 2, pp. 257–267, Feb. 2005.
  - [30] W. Thielicke, "PIVLab - Particle image velocimetry (PIV) Tool." Matlab Central File Exchange, 2018.
  - [31] "(13 mm) Travel motorized actuators." [Online]. Available: [https://www.thorlabs.com/NewGroupPage9.cfm?ObjectGroup\\_ID=1882](https://www.thorlabs.com/NewGroupPage9.cfm?ObjectGroup_ID=1882). [Accessed: 23-Jun-2019].

# Appendices

# Appendix A

All velocities (pixel/frame) obtained from the PIV analysis per measurement and for each sample when using water. Each Measurement used in analysis passed the quality check.

Measurement # (used in analysis)	D20S40A				D80S20A			
	Phase1	Phase2	Phase3	Phase4	Phase1	Phase2	Phase3	Phase4
1	70.72	42.43	314.36	435.26	20.99	20.99	25.55	49.73
2	42.43	435.26	453.06	57.49	20.99	49.73	18.71	30.57
3	314.36	453.06	219.46	87.14	25.55	18.71	9.58	58.86
4	435.26	57.49	87.14	180.68	49.73	30.57	58.86	15.51
5	431.16	204.40	186.15	198.01	13.23	15.06	16.88	91.25
6	453.06	87.14	53.38	661.56	18.71	58.86	81.21	99.92
7	139.16	50.19	507.35	725.44	34.68	34.22	49.28	204.40
8	57.49	180.68	661.56	667.95	30.57	15.51	99.92	111.78
9	219.46	53.38	662.48	714.49	9.58	81.21	178.85	28.74
10	204.40	198.01	307.97	563.01	15.06	91.25	77.56	64.79
11	143.72	619.59	480.89	491.84	56.12	78.93	15.97	18.71
12	87.14	661.56	714.49	544.76	58.86	99.92	28.74	99.92
13	25.09	486.82	676.62	720.42	16.43	118.17	61.14	56.58
14	50.19	725.44	642.40	679.81	34.22	204.40	25.55	72.54
15	186.15	307.97	551.15	709.93				

Measurement # (used in analysis)	D80S40A				D80S40N			
	Phase1	Phase2	Phase3	Phase4	Phase1	Phase2	Phase3	Phase4
1	83.95	93.99	210.33	279.68	11.41	11.86	24.64	34.68
2	93.99	279.68	52.93	145.09	11.86	34.68	30.11	83.49
3	210.33	52.93	17.79	110.41	24.64	30.11	25.09	141.89
4	279.68	145.09	110.41	55.21	34.68	83.49	141.89	161.06
5	31.94	31.94	98.09	73.46	20.08	44.26	130.03	54.29
6	52.93	110.41	19.16	64.79	30.11	141.89	26.01	144.63
7	145.09	93.99	12.78	67.07	62.96	67.98	160.60	157.41
8	145.09	55.21	64.79	110.87	83.49	161.06	144.63	106.76
9	17.79	19.16	75.28	119.99	25.09	26.01	162.88	141.44
10	31.94	73.46	76.19	103.11	44.26	54.29	70.26	134.14
11	77.56	16.43	31.94	93.53	140.53	166.53	55.21	140.53
12	110.41	64.79	119.99	88.06	141.89	144.63	141.44	176.11
13	55.66	39.24	99.46	73.46				
14	93.99	67.07	33.31	81.67				
15	98.09	76.19	92.62	83.95				
16	55.21	110.87	88.06	114.52				

All velocities (pixel/frame) obtained from the PIV analysis per measurement and for each sample when using glycerol. Each Measurement used in analysis passed the quality check.

Measurement # (used in analysis)	D20S40A				D80S20A			
	Phase1	Phase2	Phase3	Phase4	Phase1	Phase2	Phase3	Phase4
1	14.88	27.56	80.06	116.81	28.44	32.81	54.69	49.88
2	27.56	116.81	41.56	140.00	32.81	49.88	35.00	31.94
3	80.06	41.56	104.56	138.69	54.69	35.00	63.44	48.56
4	116.81	140.00	138.69	134.31	49.88	31.94	48.56	53.38
5	29.31	136.50	101.50	123.81	40.69	109.81	63.00	23.63
6	41.56	138.69	80.06	97.13	35.00	48.56	10.06	26.25
7	96.69	59.06	55.13	123.81	58.63	34.56	56.44	18.81
8	140.00	134.31	97.13	76.13	31.94	53.38	26.25	17.50
9								

Measurement # (used in analysis)	D80S40A				D80S40N			
	Phase1	Phase2	Phase3	Phase4	Phase1	Phase2	Phase3	Phase4
1	20.56	19.25	69.56	70.44	9.63	14.44	35.44	50.31
2	19.25	70.44	17.94	98.44	14.44	50.31	14.44	49.88
3	69.56	17.94	32.81	112.00	35.44	14.44	20.56	79.63
4	70.44	98.44	112.00	108.50	50.31	49.88	79.63	100.63
5	9.63	50.31	81.81	24.06	9.63	25.38	68.25	38.50
6	17.94	112.00	13.13	57.31	14.44	79.63	23.19	26.25
7	62.56	36.75	30.19	58.63				
8	98.44	108.50	57.31	48.56				
9	32.81	13.13	62.13	45.94				

# Appendix B

## MATLAB Script (Color to Black and White Conversion)

```
%water and glass
%crop dimensions -> x1=400-x2=1200

%glycerol and glass
%crop dimensions -> x1=450-x2=1050

%!!! same cropping resolution needs to be used for video's you want to
%analyze together (800x800 pixels)
%%loading images and cropping
myDir = 'D:\Mijn Bestanden\Documents\All Glycerol Re-
Analyzed\D80S20A\C0458\';
ext_img = '*.jpg';

a = dir([myDir ext_img]);
nfile = max(size(a)) ; % number of image files

for i=1:nfile
    my_img(i).img = imread([myDir a(i).name]);
    %my_img_crop(i).img = imcrop(my_img(i).img,[x1 y1 x2 y2]);
    x1 = 0;
    y1 = 0;%always zero
    my_img_crop(i).img = imcrop(my_img(i).img,[x1 y1 1050 800]);
end
%% processing
itt=1;
while itt<nfile+1
    RGB = my_img_crop(itt);
    RGB = RGB.img;

    Br=mean(mean(RGB(:,:,1)));
    BW=im2bw(RGB,Br*0.0033);%Filter to binary image (black and white), with
a certain threshold
    %rotate image if needed
    %BW = imrotate(BW,180);

    picname=sprintf('%d.jpg', itt+100);
    fullFileName = fullfile('D:\Mijn Bestanden\Documents\All Glycerol Re-
Analyzed\D80S20A\C0458_re',picname);
    imwrite(BW, fullFileName);

    itt= itt+1;
end
```

## MATLAB Script (Averages)

```
clear all
avg = [];
avg_parts = [];

for i=1:12%number of measurements for this sample (measurement has 4
phases)

    for parts=1:4 %number of phases
        str_parts = num2str(parts*i);
```



```

file = "D:\Mijn Bestanden\Documents\All Water Re-
Analyzed\D80S40N\Results 4Phases\part"+ str_parts + ".mat";
IN = load(file);
exp = IN.mag;
exp(any(isnan(exp), 2), :) = [];
avg_parts = [avg_parts mean(exp)];
end
avg = [avg; avg_parts];
avg_parts = [];
end

```

## MATLAB Script (Significance)

```

close all;clearvars;clc
% D=Diameter, S=Spacing, A=alignment
% Data per geometry and per phase
% Columns 1-4: D20S40A, Columns 5-8: D80S20A, Columns 9-12: D80S40A,
Columns 13-16: D80S40N (4 phases per geometry)
% Water
W =[1.5500    0.9300    6.8900    9.5400    0.4600    0.4600    0.5600
1.0900    1.8400    2.0600    4.6100    6.1300    0.2500    0.2600
0.5400    0.7600
    0.9300    9.5400    9.9300    1.2600    0.4600    1.0900    0.4100
0.6700    2.0600    6.1300    1.1600    3.1800    0.2600    0.7600
0.6600    1.8300
    6.8900    9.9300    4.8100    1.9100    0.5600    0.4100    0.2100
1.2900    4.6100    1.1600    0.3900    2.4200    0.5400    0.6600
0.5500    3.1100
    9.5400    1.2600    1.9100    3.9600    1.0900    0.6700    1.2900
0.3400    6.1300    3.1800    2.4200    1.2100    0.7600    1.8300
3.1100    3.5300
    9.4500    4.4800    4.0800    4.3400    0.2900    0.3300    0.3700
2.0000    0.7000    0.7000    2.1500    1.6100    0.4400    0.9700
2.8500    1.1900
    9.9300    1.9100    1.1700    14.5000    0.4100    1.2900    1.7800
2.1900    1.1600    2.4200    0.4200    1.4200    0.6600    3.1100
0.5700    3.1700
    3.0500    1.1000    11.1200    15.9000    0.7600    0.7500    1.0800
4.4800    3.1800    2.0600    0.2800    1.4700    1.3800    1.4900
3.5200    3.4500
    1.2600    3.9600    14.5000    14.6400    0.6700    0.3400    2.1900
2.4500    3.1800    1.2100    1.4200    2.4300    1.8300    3.5300
3.1700    2.3400
    4.8100    1.1700    14.5200    15.6600    0.2100    1.7800    3.9200
0.6300    0.3900    0.4200    1.6500    2.6300    0.5500    0.5700
3.5700    3.1000
    4.4800    4.3400    6.7500    12.3400    0.3300    2.0000    1.7000
1.4200    0.7000    1.6100    1.6700    2.2600    0.9700    1.1900
1.5400    2.9400
    3.1500    13.5800    10.5400    10.7800    1.2300    1.7300    0.3500
0.4100    1.7000    0.3600    0.7000    2.0500    3.0800    3.6500
1.2100    3.0800
    1.9100    14.5000    15.6600    11.9400    1.2900    2.1900    0.6300
2.1900    2.4200    1.4200    2.6300    1.9300    3.1100    3.1700
3.1000    3.8600
    0.5500    10.6700    14.8300    15.7900    0.3600    2.5900    1.3400
1.2400    1.2200    0.8600    2.1800    1.6100    NaN    NaN
NaN    NaN
    1.1000    15.9000    14.0800    14.9000    0.7500    4.4800    0.5600
1.5900    2.0600    1.4700    0.7300    1.7900    NaN    NaN
NaN    NaN

```

```

    4.0800    6.7500    12.0800    15.5600         NaN         NaN         NaN
NaN    2.1500    1.6700    2.0300    1.8400         NaN         NaN         NaN
NaN
    NaN         NaN         NaN         NaN         NaN         NaN         NaN
NaN    1.2100    2.4300    1.9300    2.5100         NaN         NaN         NaN
NaN];
    W = W*45.625; % convert from px/frame to um/sec
%Glycerol
G =[0.3400    0.6300    1.8300    2.6700    0.6500    0.7500    1.2500
1.1400    0.4700    0.4400    1.5900    1.6100    0.2200    0.3300
0.8100    1.1500
    0.6300    2.6700    0.9500    3.2000    0.7500    1.1400    0.8000
0.7300    0.4400    1.6100    0.4100    2.2500    0.3300    1.1500
0.3300    1.1400
    1.8300    0.9500    2.3900    3.1700    1.2500    0.8000    1.4500
1.1100    1.5900    0.4100    0.7500    2.5600    0.8100    0.3300
0.4700    1.8200
    2.6700    3.2000    3.1700    3.0700    1.1400    0.7300    1.1100
1.2200    1.6100    2.2500    2.5600    2.4800    1.1500    1.1400
1.8200    2.3000
    0.6700    3.1200    2.3200    2.8300    0.9300    2.5100    1.4400
0.5400    0.2200    1.1500    1.8700    0.5500    0.2200    0.5800
1.5600    0.8800
    0.9500    3.1700    1.8300    2.2200    0.8000    1.1100    0.2300
0.6000    0.4100    2.5600    0.3000    1.3100    0.3300    1.8200
0.5300    0.6000
    2.2100    1.3500    1.2600    2.8300    1.3400    0.7900    1.2900
0.4300    1.4300    0.8400    0.6900    1.3400         NaN         NaN
NaN         NaN
    3.2000    3.0700    2.2200    1.7400    0.7300    1.2200    0.6000
0.4000    2.2500    2.4800    1.3100    1.1100         NaN         NaN
NaN         NaN
    NaN         NaN         NaN         NaN         NaN         NaN         NaN
NaN    0.7500    0.2300    1.4200    1.0500         NaN         NaN         NaN
NaN];
    G = G*43.75; % convert from px/frame to um/sec
disp('Means and standard deviations of fluid velocity for each sample type
per phase for water')
Water=table(nanmean(W(:,1:4))',nanstd(W(:,1:4))',
nanmean(W(:,5:8))',nanstd(W(:,5:8))',
nanmean(W(:,9:12))',nanstd(W(:,9:12))',
nanmean(W(:,13:16))',nanstd(W(:,13:16))',...

'VariableNames',{'D20S40A_M','D20S40A_SD','D80S20A_M','D80S20A_SD','D80S40A
_M','D80S40A_SD','D80S40N_M','D80S40N_SD'},'RowNames',{'Phase1';'Phase2';'P
hase3';'Phase4'});
disp(Water)

disp('Means and standard deviations of fluid velocity for each sample type
per phase for glycerol')
Glycerol=table(nanmean(G(:,1:4))',nanstd(G(:,1:4))',
nanmean(G(:,5:8))',nanstd(G(:,5:8))',
nanmean(G(:,9:12))',nanstd(G(:,9:12))',
nanmean(G(:,13:16))',nanstd(G(:,13:16))',...

'VariableNames',{'D20S40A_M','D20S40A_SD','D80S20A_M','D80S20A_SD','D80S40A
_M','D80S40A_SD','D80S40N_M','D80S40N_SD'},'RowNames',{'Phase1';'Phase2';'P
hase3';'Phase4'});
disp(Glycerol)

% Data per geometry averaged across the four phases

```

```

WT=[nanmean(W(:,1:4),2) nanmean(W(:,5:8),2) nanmean(W(:,9:12),2)
nanmean(W(:,13:16),2)];
GT=[nanmean(G(:,1:4),2) nanmean(G(:,5:8),2) nanmean(G(:,9:12),2)
nanmean(G(:,13:16),2)];

% Effect of diameter, spacing, and alignment across the phases, for water
[~, pD,~, statsD]=ttest2(WT(:,1),WT(:,3)); % effect of diameter (20 vs. 80)
[~, pS,~, statsS]=ttest2(WT(:,2),WT(:,3)); % effect of spacing (40 vs. 80)
[~, pA,~, statsA]=ttest2(WT(:,3),WT(:,4)); % effect of alignment (aligned
vs. nonaligned)
disp('Table 1. Effect of diameter, spacing, and alignment across the four
phases, for water (t- and p-values)')
T=table([statsD.df statsS.df statsA.df],[statsD.tstat statsS.tstat
statsA.tstat],[pD pS
pA]','VariableNames',{'df','t','p'},'RowNames',{'Diameter';'Spacing';'Align
ment'});
disp(T)

% Effect of diameter, spacing, and alignment across the phases, for
% glycerol
clear pD statsD pS statsS pA statsA
[~, pD,~, statsD]=ttest2(GT(:,1),GT(:,3)); % effect of diameter (20 vs. 80)
[~, pS,~, statsS]=ttest2(GT(:,2),GT(:,3)); % effect of spacing (40 vs. 80)
[~, pA,~, statsA]=ttest2(GT(:,3),GT(:,4)); % effect of alignment (aligned
vs. nonaligned)
disp('Table 2. Effect of diameter, spacing, and alignment across the four
phases, for glycerol (t- and p-values)')
T=table([statsD.df statsS.df statsA.df],[statsD.tstat statsS.tstat
statsA.tstat],[pD pS
pA]','VariableNames',{'df','t','p'},'RowNames',{'Diameter';'Spacing';'Align
ment'});
disp(T)

% Effect of diameter, spacing, & alignment per phase, for water
clear pD statsD pS statsS pA statsA
pD=NaN(1,4);pS=pD;pA=pD;
for i=1:4
    [~, pD(i),~, statsD(i)]=ttest2(W(:,i),W(:,i+8)); % effect of diameter
(20 vs. 80)
    [~, pS(i),~, statsS(i)]=ttest2(W(:,i+4),W(:,i+8)); % effect of spacing
(40 vs. 80)
    [~, pA(i),~, statsA(i)]=ttest2(W(:,i+8),W(:,i+12)); % effect of
alignment (aligned vs. nonaligned)
end
disp('Table 3. Effect of diameter, spacing, and alignment per phase, for
water (t- and p-values)')
T=table(cat(1,statsD.df),cat(1,statsD.tstat),
pD',cat(1,statsS.df),cat(1,statsS.tstat),pS',cat(1,statsA.df),cat(1,statsA.
tstat),
pA','VariableNames',{'Diameter_df','Diameter_t','Diameter_p','Spacing_df','
Spacing_t','Spacing_p','Alignment_df','Alignment_t','Alignment_p'},'RowName
s',{'Phase 1';'Phase 2';'Phase 3';'Phase 4'});
disp(T)

% Effect of diameter, spacing, & alignment per phase, for glycerol
clear pD statsD pS statsS pA statsA
pD=NaN(1,4);pS=pD;pA=pD;
for i=1:4
    [~, pD(i),~, statsD(i)]=ttest2(G(:,i),G(:,i+8)); % effect of diameter
(20 vs. 80)

```

```

    [~, pS(i),~,statsS(i)]=ttest2(G(:,i+4),G(:,i+8)); % effect of spacing
(40 vs. 80)
    [~, pA(i),~,statsA(i)]=ttest2(G(:,i+8),G(:,i+12)); % effect of
alignment (aligned vs. nonaligned)
end
disp('Table 4. Effect of diameter, spacing, and alignment per phase, for
glycerol (t- and p-values)')
T=table(cat(1,statsD.df),cat(1,statsD.tstat),
pD',cat(1,statsS.df),cat(1,statsS.tstat),pS',cat(1,statsA.df),cat(1,statsA.
tstat),
pA', 'VariableNames',{'Diameter_df','Diameter_t','Diameter_p','Spacing_df','
Spacing_t','Spacing_p','Alignment_df','Alignment_t','Alignment_p'}, 'RowName
s',{'Phase 1';'Phase 2';'Phase 3';'Phase 4'});
disp(T)

% Effect of diameter, spacing, & alignment per phase, for water
phase=[ones(16,1); 2*ones(16,1); 3*ones(16,1); 4*ones(16,1)];
for i=1:4
    Wp(:,i)=reshape(W(:,(4*i-3):4*i),[],1);
    [p(i),tbl,stats(i)]=anovan(Wp(:,i),{phase});
    F(i)=cell2mat(tbl(18));
end
disp('Table 5. Comparison of phases (F- and p-values) per sample type for
water')
T=table(cat(1,stats.dfe),F',p', 'VariableNames',{'df','F','p'}, 'RowNames',{'
D20S40A';'D80S20A';'D80S40A';'D80S40N'});
disp(T)

% Effect of diameter, spacing, & alignment per phase, for glycerol
clear p tbl stats F phase
phase=[ones(9,1); 2*ones(9,1); 3*ones(9,1); 4*ones(9,1)];
for i=1:4
    Gp(:,i)=reshape(G(:,(4*i-3):4*i),[],1);
    [p(i),tbl,stats(i)]=anovan(Gp(:,i),{phase});
    F(i)=cell2mat(tbl(18));
end
disp('Table 6. Comparison of phases (F- and p-values) per sample type for
glycerol')
T=table(cat(1,stats.dfe),F',p', 'VariableNames',{'df','F','p'}, 'RowNames',{'
D20S40A';'D80S20A';'D80S40A';'D80S40N'});
disp(T)

% Effect of fluid type
 [~, pa,~,statsa]=ttest2(WT(:,1),GT(:,1)); % for D20S40A
 [~, pb,~,statsb]=ttest2(WT(:,2),GT(:,2)); % for D80S20A
 [~, pc,~,statsc]=ttest2(WT(:,3),GT(:,3)); % for D80S40A
 [~, pd,~,statsd]=ttest2(WT(:,4),GT(:,4)); % for D80S40A
disp('Table 7. Effect of fluid type on drainage for each sample type (t-
and p-values)')
T=table([statsa.df statsb.df statsc.df statsd.df]',[statsa.tstat
statsb.tstat statsc.tstat statsd.tstat]',[pa pb pc
pd]', 'VariableNames',{'df','t','p'}, 'RowNames',{'D20S40A';'D80S20A';'D80S40
A';'D80S40N'});
disp(T)

% plots
% across phases, for water
figure;boxplot(WT);title('Water');
set(gca,'xticklabel',{'D20S40A','D80S20A','D80S40A','D80S40N'})
xlabel('Sample type')
ylabel('Velocity [\um/sec]')

```

```

% per phase, for water
figure;boxplot(W,'color','kcrb');title('Water');
set(gca,'xticklabel',{'','D20S40A',' ',' ',' ','D80S20A',' ',' ',' ','D80S40A',' ',' ',' ','D80S40N',' ',' ',' ',' '})
hold on; plot([4.5 4.5],[0 800],'k-')
plot([8.5 8.5],[0 800],'k-')
plot([12.5 12.5],[0 800],'k-')
plot([16.5 16.5],[0 800],'k-')
xlabel('Sample type')
ylabel('Velocity [\mum/sec]')
boxes = findobj(gca, 'Tag', 'Box');
legend(boxes([end 3 2 1]), 'Phase 1', 'Phase 2', 'Phase 3', 'Phase 4')
ylim([0 800])

% across phases, for glycerol
figure;boxplot(GT);title('Glycerol');
set(gca,'xticklabel',{'D20S40A','D80S20A','D80S40A','D80S40N'})
xlabel('Sample type')
ylabel('Velocity [\mum/sec]')

% per phase, for glycerol
figure;boxplot(G,'color','kcrb');title('Glycerol');
set(gca,'xticklabel',{'','D20S40A',' ',' ',' ','D80S20A',' ',' ',' ','D80S40A',' ',' ',' ','D80S40N',' ',' ',' ',' '}, 'YTick',0:25:150)
hold on; plot([4.5 4.5],[0 150],'k-')
plot([8.5 8.5],[0 150],'k-')
plot([12.5 12.5],[0 150],'k-')
plot([16.5 16.5],[0 150],'k-')
xlabel('Sample type')
ylabel('Velocity [\mum/sec]')
boxes = findobj(gca, 'Tag', 'Box');
legend(boxes([4 3 2 1]), 'Phase 1', 'Phase 2', 'Phase 3', 'Phase 4')
ylim([0 150])

```

# Appendix C

## Product Information

### Polystyrene Latex Beads

Catalog Numbers **LB1, LB3, LB5, LB6, LB8, LB11, LB30, SD6A, SD26, SD91, CLB4, and CLB9**  
Store at Room Temperature

#### Product Description

Uniform latex particles were first discovered in 1947. Since then they have been utilized in a wide variety of applications including electron microscopy and cell counter calibration, antibody mediated agglutination diagnostics, phagocytosis experiments, and many others.

Polystyrene microparticles are negative charge-stabilized colloidal particles. The microparticles are produced by polymerization of styrene under conditions that induce spontaneous coalescent bead formation. Polymerization is terminated when two chains react to make a sulfate-terminated polymer chain. These terminal sulfate groups locate on the particle surface where they interact with the aqueous phase.

Latex beads are supplied as aqueous suspensions. The percent solids concentrations are expressed as weight per weight (w/w) values.

The number of particles per milliliter (N) can be calculated using the following equation:

$$N = \frac{(6 \times 10^{10}) \times S \times P_L}{\pi \times P_s \times d^3}$$

where:

S = % solids (w/w)

d = diameter (μm)

P<sub>s</sub> = density of bulk polymer (g/mL)

P<sub>L</sub> = density of latex (g/mL)

This reduces to:

$$N = \frac{1.828 \times 10^{11}}{d^3}$$

when:

S = 10% solids

P<sub>s</sub> = 1.05 g/mL (polystyrene)

P<sub>L</sub> = 1.005 g/mL

The refractive index at 589 nm for polystyrene is 1.5905; and 1.602 at 486 nm.

The latex bead suspensions are composed mainly of polymer particles and water, with small amounts of surfactant, sodium bicarbonate and potassium sulfate. A typical latex bead contains the following:

water	>69.0%
polymer	30.0%
surfactant	0.1–0.5%
inorganic salts	0.2%

Carboxylate and amine modified latex bead suspensions also contain 0.3–1.5% water-soluble polymer. The surfactant is added to the suspension in order to stabilize the suspension. Removal of the surfactant will cause the beads to be more susceptible to flocculation.

#### Precautions and Disclaimer

This product is for R&D use only, not for drug, household, or other uses. Please consult the Safety Data Sheet for information regarding hazards and safe handling practices.

#### Preparation Instructions

##### Resuspension:

Particles larger than 0.6 μm tend to settle on prolonged storage. Particles can be easily resuspended by gentle agitation until they are returned to a uniform suspension. Depending on the particle size uniform redispersion may take several hours. Mild ultrasonic agitation can also be used.

**Diluting Particles:**

Particles can often be diluted with deionized water. However, some particles, especially at very dilute concentrations, may require additional surfactant. An anionic surfactant, especially alkyl sulfonates such as sodium dodecyl sulfate, can be used. Nonionic surfactants such as Triton™ X-100 and TWEEN® 20 can also be used. Suggested working concentration of surfactant should be <0.1% in the aqueous phase. Addition of electrolytes may cause destabilization of the particle suspension. In this case nonionic detergents may be more suitable in the diluent.

**Concentrating Particles:**

Particles can be concentrated by gravity settling, centrifugation, diafiltration, or evaporation. One micron particles will settle at an approximate rate of 1.57 mm/day. Larger particles will settle faster. Smaller particles (<0.5 μm) will never settle by gravity alone.

Centrifugation time can be calculated from the following equation:

$$V_m = 5.488 \times 10^{-5} \times (P_s - 1) \times d^2$$

where:

$V_m$  = maximum settling velocity  
 $P_s$  = density of bulk polymer (1.05 g/cm<sup>3</sup> for polystyrene)  
 $d$  = particle diameter (μm)

For a 5% suspension:

$$V_h = 2/3 \times g \times V_m$$

where:

$V_h$  = True settling velocity of a 5% suspension (cm/hr)  
 $g$  =  $g$  force

As an example, 1 mL of a 1% (w/w) 0.3 μm bead suspension can be spun down in about 10 minutes at 17,000 rpm. Longer centrifugation times will be required if a tightly compacted pellet is desired.

Centrifugation should be terminated without the use of the centrifuge brake. The supernatant should be siphoned off, not decanted. The addition of surfactant before settling or centrifugation may prevent over-compaction of the latex pellet. Resuspension can be accomplished by gentle agitation or by probe-type sonication.

Particles can also be concentrated by diafiltration. High molecular weight cut-off membranes (up to 1 million) are most efficient.

**Storage/Stability**

They may be stored at room temperature or refrigerated. However, they should be protected from freezing. Latex beads that have been frozen look like cottage cheese.

Latex beads are not considered sterile.

**Procedures****Cleaning Latex Beads:**

Your protocol may require that the existing surfactant and/or inorganic salts be removed from the latex bead suspension. This may be accomplished by centrifugation, diafiltration or dialysis. High molecular weight cut off membranes (up to 1 million) should be used for these applications.

**Sterilization:****1. Pasteurization**

Heating beads for 24 hours at 70 °C has been shown to be an effective method for killing most microbes in latex preparations.

**2. Tantalization**

Several cycles alternating between 37 °C and 60 °C have been reported to kill bacteria by induction of spore vegetation at 37 °C and killing vegetative cells at 60 °C.

**3. γ-Irradiation**

A dose of 0.03 megarad/hr for 24 hours (0.72 megarad) has been shown to control most microbes. However, a few yeast cells may survive up to 3.0 megarads.

**4. UV Irradiation**

UV irradiation can be used on very dilute suspensions (<0.1% solids). Suspensions should appear clear for this method to work.

**5. Antimicrobials**

The addition of common antimicrobials such as sodium azide, thimerosal, and formaldehyde can be used to prevent microbial growth.



## Coupling Procedures

### 1. Passive Adsorption

Many proteins can be passively adsorbed on the particle surface. The most popular use of latex beads is in the diagnostic use of adsorbed antibodies or antigens. The multivalent nature of antibodies allows them to bind to antigens on more than one latex bead simultaneously, causing the latex beads to agglutinate. Other proteins and ligands can be covalently bound to the particle surface.

Proteins and other biochemicals can be passively adsorbed on the bead surface by simply dissolving in a buffer, adding to a bead suspension, and stirring for times ranging from a few minutes to more than a day.<sup>1-4</sup>

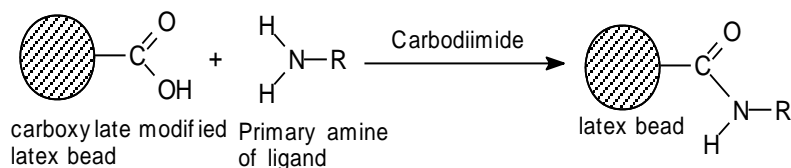
A typical protein adsorption procedure would use 1 mL of 1% bead suspension in a buffer such as 25–50 mM MES, pH 6.1, containing a final protein concentration up to 2 mg/mL. The adsorption reaction is stopped by centrifuging the suspension and resuspending the pellet in 1 mL of buffer. Centrifugation and resuspension should be repeated until the unbound protein is no longer present in the supernatant.

Protein coupling tends to decrease with increasing pH due to anionic repulsion. MES buffer typically gives good results. Phosphate buffer under acidic conditions typically gives poor results. Low protein binding can possibly be increased by adding more protein, decreasing surfactant concentration, use of beads with a different surface charge density, changing buffer, or precipitating the protein onto the bead surface ("forced" absorption).<sup>1,5</sup>

### 2. Covalent Coupling – Carboxylate-Modified beads

If passive adsorption is not suitable, covalent coupling of proteins and other ligands may be a viable alternative.

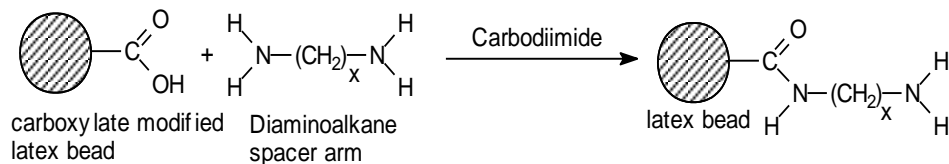
Water-soluble carbodiimide coupling agents, such as EDAC [1-ethyl-3-(3-dimethylaminopropyl) carbodiimide] can be used with carboxylate modified beads to covalently link ligands directly through primary amine groups on the ligand.<sup>2,6,7</sup>



In a typical carbodiimide coupling reaction 1 mL of a 1% bead suspension containing 25–50 mM MES buffer, pH 6.1, 0.15–2.6 mM EDAC (Product Number E7750) and up to 2 mg/mL of protein. Reaction termination and washing steps would be the same as mentioned above in the passive adsorption method.

An alternate method involves the formation of an intermediate active ester.<sup>8</sup> One advantage of the active ester method is that it allows separation of the ligand from the carbodiimide, thus preventing possible crosslinking of the ligand.

The carboxylate modified beads can also be converted to amine modified beads containing a spacer arm via the carbodiimide method.<sup>7,9,10</sup>

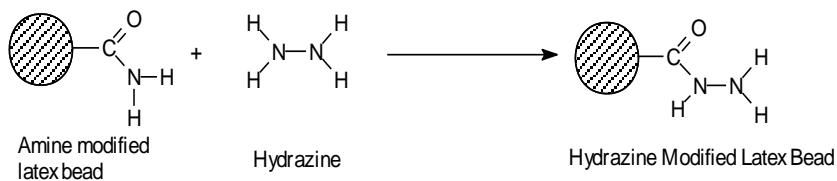


This is accomplished by reacting the beads with spacers such as diaminopentane. These spacer arms are particularly useful in antibody and other protein applications where steric hindrance is a common problem. Subsequent protein coupling can be accomplished by glutaraldehyde and other crosslinking methods (see coupling procedures for amine-modified beads below).

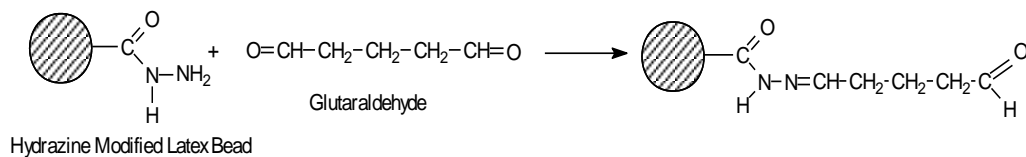
Similarly, 6-aminocaproic acid can be used to create particles with carboxylate modified surfaces attached to the bead surface through spacer arms.<sup>9</sup>

### 3. Covalent Coupling – Amine-Modified beads

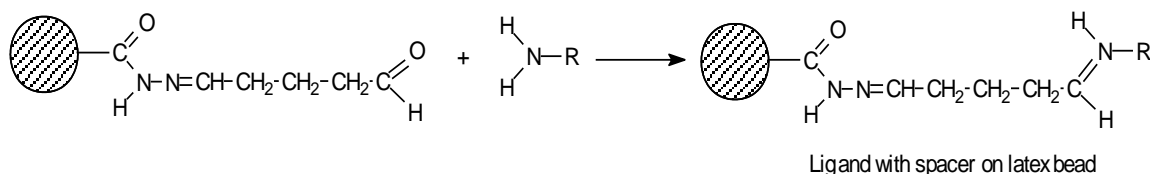
Because of the need to maintain the stability of the latex suspension in aqueous systems, amine modified beads are typically first treated in aqueous systems with hydrazine, yielding an active hydrazide form.<sup>11</sup>



The hydrazine-modified particles are very versatile since so many different reactions can be performed on their surfaces.<sup>12</sup> The easiest methods for subsequent coupling employ bifunctional compounds such as glutaraldehyde.<sup>12</sup> In this two step reaction, hydrazine-modified beads are first treated with glutaraldehyde at 25 °C for four hours.



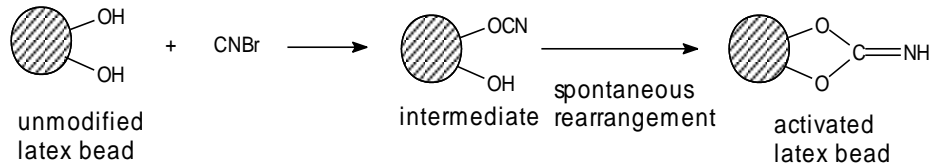
The second reaction couples the ligand to the beads and can be performed at 2–5 °C for 4 to 7 days.



Glutaraldehyde can also be used to couple ligands directly to the amine groups on amine modified beads.<sup>9</sup>

#### 4. Covalent Coupling to Unmodified Polystyrene Beads

Ligands with primary amine groups can be coupled to the surface hydroxyls of unmodified beads via cyanogen bromide activation.<sup>13-15</sup>



Other methods include tosyl chloride or trifluoroethane sulfonyl chloride activation,<sup>16-18</sup> carbonyl diimidazole,<sup>18-20</sup> and direct nitration/amination.<sup>21</sup>

#### Dyeing Particles

Fluorescent dyes can be easily covalently coupled to the surface of modified particles.<sup>9</sup> Dyeing the inside of the particle may be desired in order to minimize interference with exterior-coupled ligands. Oil soluble dyes are typically used. Large crosslinked particles (>5  $\mu\text{m}$ ) are dried and added directly to the dye dissolved in an organic solvent.<sup>22</sup> Smaller particles require careful adjustment of dye quantities in a biphasic coupling reaction.<sup>23</sup>

#### Applications

The most popular use of latex beads today is in the field of immunodiagnosics, particularly in latex agglutination tests. This method allows the detection of minute amounts of antigens or antibodies in serum, urine, and cerebrospinal fluids.<sup>1</sup>

Antigen-coated latex beads will agglutinate in the presence of minute amounts of antibody forming visible aggregates. The same visible agglutination occurs when the latex beads are coated with antibodies and exposed to antigens. Another popular method is the latex agglutination inhibition test. This method uses the indication that agglutination inhibition is observed in mixtures of antigen-bound beads and antibodies when free antigens are introduced.

Latex beads are also being used in phagocytosis research.<sup>24-27</sup> Typically latex beads being used in these applications range from <0.05  $\mu\text{m}$  to 3  $\mu\text{m}$  in size.

#### References

1. Hechemy, K.E., and Michaelson, E.E. *Laboratory Management*, 22(6), 27, ff(Part I) and 22(7), 26, ff(PartII), 1984.
2. Nathan, C.F. and Cohn, Z.A. *J. Exp. Med.*, 154, 1539-1553 (1981).
3. Pollack, W. U.S. Patent 2 234 096, (1966).
4. Rush, R.A., Kindler, S.H., and Udenfriend, S., *Clin. Chem.*, 21(1), 148-150, (1975).
5. Hechemy, K.E. U.S. Patent 4 397 959, (1983).
6. Hager, H. U.S. patent 3 857 931, (1974).
7. Quash, G., Roch, A.-M, Niveleau, A., Grang, J., Keolouangkhhot, T., and Huppert, J., *J. of Immunological Methods* 22, 165-174, (1978).
8. Dorman, L.C., U.S. Patent 4 045 384, (1977).
9. Molday, R.S., Dreyer, W.J., Rembaum, A., and Yen, S.P.S. *J. Cell Biol.*, 64, 75-88, (1975).
10. Rembaum, A., et al., *Macromolecules*, 9(2), 328-336 (1976).
11. Dorman, L.C., U.S. Patent 4 046 723, (1977).
12. Dorman, L.C., U.S. Patent 4 421 896, (1983).
13. Cuatrecasas, P., *J. Biol. Chem.* 245, 3059, ff, (1970).
14. Porath, J., In *"Methods in Enzymology, Volume XXXIV, Affinity Techniques, Enzyme Purification: Part B"*, Jakoby, W.B., Wilchek, M., Eds., Academic Press: New York, 1974;[2], 13-30.
15. Srere, P.A., Uyeda, K., In *"Methods in Enzymology, Volume XLIV, Immobilized Enzymes"*, Mosbach, K., ed.; Academic Press: New York, 1976;[2], 11-19.
16. Nilsson, K., and Mosbach, K., *Eur. J. Biochem.* 112, 397-402, (1980).
17. Nilsson, K., and Mosbach, K., *Biochem, Biophys. Res. Commun.* 102, 449-457.
18. Nustad, K., Ugelstad, J., Berge, A., Ellingsen, T., Schmid, R., Johansen, L., and Bormer, O., In *"Radioimmunoassay and Related Procedures in Medicine 1982"*; pp 45-45; LAEA-SM-259/19.
19. Bethell, G.S., Ayers, J.S., Hancock, W.S., and Hearn, M.T.W. *J. Biol. Chem.* 254, 2572-2574, (1979).

20. Nustad, K., Johansen, L., Schmid, R., Ugelstand, J., Ellingsen, T. and Berge, A. *Agents Actions Suppl.*, 9, 207-212, (1982).
21. Tenoso, H.J., Smith, D.B., *Covalent Bonding of Antibodies to Polystyrene Latex Beads: A Concept*". NASA Tech. Brief 1972, B72-10006; NASA TSP 1972m 72-10006 (Technology Utilization Office, NASA, Code KT, Washington, DC 20546).
22. The Dow Chemical Co., "Dyeing Large Particles"; 1972.
23. Vanderhoff, J.W., Lehigh University, personal communication, 1974.
24. Williams, C.A., Chase, M.W., Eds., *Methods in Immunology and Immunochemistry*"; Academic Press: New York, 1976; Vol. V, pp 280-1.
25. Roberts, J. and Quastel, J.H., *Biochem. J.*, 89, 150-156, (1963).
26. Kenny, M.T., *"Bibliography: Biomedical Uses of Latex Particles"*; The Dow Chemical Co.: Indianapolis, 1976.
27. Kenny, M.T., *"Bibliography: Biomedical Uses of Latex Particles (1976-1977)"*; The Dow Chemical Co.: Indianapolis, 1978.
28. Uniform Latex Particles, Published by Seradyne, Particle Technology Division, Indianapolis, IN, 1984.

Triton is a trademark of The Dow Chemical Company or an affiliated company of Dow  
TWEEN is a registered trademark of Croda International PLC

Acknowledgement - Portions of this document were taken from a supplier's manual.<sup>28</sup>

RBG,MAM 07/16-1

# Appendix D

## Measurement methods for microfluidic flow and pressure: a performance-based review

De Geyndt Wouter, Delft University of Technology

Keywords: rheology, velocimetry, anemometry, pressure sensor, pressure gauge

### **Abstract**

When searching for a method to measure fluidic flow and pressure, the principle on which the measurement works is often determined first, and then performance criteria shortcomings are worked around later. Alternatively, the performance requirements can be the first filter, and method compatibility could be worked around later. In order to support the latter approach, we reviewed measurement methods for fluidic flow and pressure based on performance criteria instead of their operating principle. Methods are separated depending on their level of invasiveness. This review offers a general overview of what methods can be used as well as a ‘performance requirements first’ approach.

### **1. Introduction**

The most fundamental properties in fluid dynamics, are the fluid flow and fluidic pressure. Fluid flow is defined by the velocity and/or direction of a fluid, while pressure is defined as the force a fluid exerts on an area within or in contact with that fluid. There are many methods to measure these properties and choosing a method for a specific goal can be difficult. A choice can be made with a ‘compatibility first’ or a ‘performance criteria first’ approach. In order to bring attention to the latter approach, measurement methods based on performance criteria and level of invasiveness were reviewed.

Miniaturization of electrical and mechanical components in the 1980s gave rise to the field of

micro electro-mechanical systems (MEMS). MEMS were built for several purposes such as smaller, faster, and lower material requirements (i.e., accelerometer for measuring static and dynamical forces). In the 1990s, micro pumps were being built because they could offer control over small quantities ( $\mu\text{L}$ , nL, pL). This brought attention to the field of microfluidics [1]. Unlike gravity and viscosity for macroscopic fluidics, the dominating microscopic fluidic properties include surface tension, energy dissipation, fluid resistance, and diffusion [2]–[4].

Microfluidics are used in medicine, engineering, biology, and many other fields. In medicine, microfluidics are used in order to control  $\mu\text{L}$ , fL, or

pL quantities for drug development, or to run diagnostics with minute fluid volumes [5], [6]. In engineering, the dominant properties in microfluidics such as capillary forces are used for micropumps and other devices in order to achieve better control or higher energy efficiency compared to the macroscale device [7]. Engineering an environment (surface wetting and channel dimensions) that exactly determines the influence of properties on the fluid in the channel lead to improvements (smaller, faster, more efficient) in consumer products such as inkjet printers and airbags [1]. Microfluidics has also been contributing to great progress in the field of molecular biology, such as in DNA, RNA, proteomic, and enzymatic analysis [8]–[11].

In this review we focus on measurement methods of microfluidic flow in open and closed channels, and microfluidic pressure in flow and no-flow conditions. Currently, there are many reviews available focusing on one specific measurement method, but a comparative evaluation of various measurement methods containing recent performance data is missing. In this review, measurement methods of fluid flow and pressure are evaluated and compared based on several performance criteria. This way, the overview aims to serve as a guidance tool where depending on required performance levels, experimentalist can choose which method is more promising for their needs on a performance criteria first approach.

The performance criteria for fluid flow measurements consists out of spatial resolution because dimensional accuracy determines how well small variations on a spatial level (flow vector direction) can be distinguished from each other, temporal resolution because the speed at which tracking is done depends on flow velocity and how well small variations in flow speed can be distinguished from each other (flow vector magnitude), whether the method measures a point or area (multiple points), and whether the method requires optical access or not.

The performance criteria for microfluidic pressure measurements consists out of pressure resolution (accuracy) because the changes in pressure has to be measurable, temporal resolution because more than one pressure measurement needs to be recorded before, after, and during the pressure change, the probe/chip's area, and whether the method is liquid and/or gas compatible.

## **2. Fluid Flow**

Fluid flow measurement methods measure flow speed and/or flow direction. An important criterion when choosing a fluid flow measurement method is whether and to what extent the required measuring equipment interferes with and/or alters the flow. Accordingly, in this review, the measurement methods are categorized based on the degree of their invasiveness to the flow. Three levels of

decreasing invasiveness are distinguished here: invasive, minimally invasive, and non-invasive.

We include methods for both liquids and gasses, and for open and closed channel flow. Purely mechanical measurement methods such as the Daloz Anemometer (also called 'ping-pong ball' anemometer), the cup anemometer, and the vane anemometer are not discussed here as these are macroscopic techniques.

## 2.1 Invasive

A measurement method is defined as invasive if it requires a piece of equipment (i.e., probe) to remain static inside the flow and therefore interferes with the natural behavior of the system. The amount of disturbance mainly depends on the probe dimensions and the fluidic properties.

### 2.1.1 Electrical Tomography (ET)

Invented in 1933 [12], ET measures the change in the electrical resistance, capacitance, or magnetic inductance of a wire while suspended in a flow. The wire is generally placed perpendicularly to the flow direction (

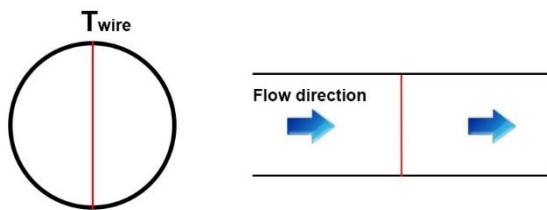


Figure 1).

ET has a temporal resolution that can go down to  $17 \mu\text{s}$  [13] and a spatial resolution limited to the contact area of the wire with the fluid. Using

wire arrays creates more measurement points than single wires, and enables to reconstruct the velocity distribution and local changes in fluid properties at a given cross-section (two dimensions) [14]. Compared to one array of electrodes, using multiple arrays of electrodes parallel to each other allow for gather data on flow velocity in three dimensions [15].

The most well-known form of electrical resistance tomography (or electrical impedance tomography, EIT) is the hot-wire anemometer. It is likely one of the oldest fluid measurement techniques using electricity [16]. This method requires a current to heat up the wire and a liquid that flows past the wire to cool it down. By measuring the resistance in the wire, its temperature is determined. The difference in temperature between no flow and the flow of interest is then equal to the heat lost due to convection caused by the fluid which is directly proportional to fluid flow speed. A typical hot-wire diameter ranges between 1 and  $5 \mu\text{m}$  [17], [18]. The smallest dimensions -thickness (depth) x width- for EIT reported is  $260 \text{ nm} \times 3.36 \mu\text{m}$  [19] and  $130 \text{ nm} \times 50 \mu\text{m}$  [20]. In other variations of EIT, the heated wire is replaced with a heated film [21], [22].

Electrical capacitance tomography (ECT) is very similar to EIT. The only difference is that electrical capacitance is measured instead of resistance [16]. Despite its similarity to EIT, ECT is rarely used in fluid measurements [23].

Magnetic inductance tomography (MIT) measures electricity induced by a magnetic field and is therefore not used in fluid flow unless the flow generates its own magnetic field which has only been reported in a liquid metal flow [24]. However, due to its small spatial and high temporal resolution, MIT is broadly used in brain imaging [16].

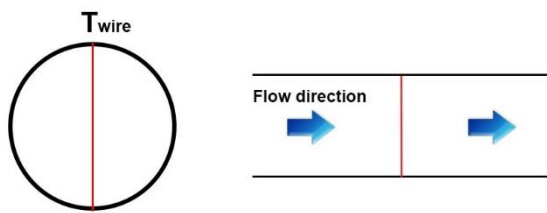


Figure 1: Set-up of a single wire Electrical Tomography for a fluid flow in a pipe. The wire is placed perpendicularly to the flow direction, and a current is run through the wire. The current and fluid flow bring the wire to a temperature equilibrium  $T_{wire}$ , and flow velocity is determined based on the resistance measured at  $T_{wire}$ .

### 2.1.2 Thermal Mass Flow Rate Meter (TMFRM)

A mass flow meter or inertial flow meter refers to two distinct types of measurement setups: the thermal mass flow rate meter and the Coriolis flow rate meter. Because the Coriolis flow rate meter is rarely used for micro fluidics, it is not discussed here.

In a TMFRM, a heating element and temperature sensor are inserted in the fluid flow in order to heat up a specific amount of fluid and measure the time the heated-up fluid needs to arrive at the temperature sensor (Figure 2). The

method was invented in 1914 and was based on the hot-wire anemometer [25].

The lag (speed) in detecting the heated region is completely dependent on the flow velocity and the distance between the heating element and temperature sensors. This means that the temporal resolution is very low because measurements can only be as fast as the time it takes for the fluid to reach the temperature sensor after being heated. The accuracy of a TMFRM measurement can be increased by releasing shorter and hotter heat pulses, and by estimating the minimal amount of heating that would be required to detect it later on. The smaller the amount of liquid that is heated, the quicker the heated region loses its heat, but the more accurately the velocity can be measured [26].

TMFRM is highly restricted in terms of flow velocity and element size. The flow has to be steady and laminar in order to ensure detection of the heated region when it reaches the sensor. The minimum size of the heating element is restricted by the fact that it has to be capable of heating up a detectable (by the sensor) volume of fluid in a short amount of time. The smaller a heating element is, the hotter it needs to be, resulting in a larger thermal stress. Because thermal stress is proportional to temperature change, smaller elements create higher stresses for heating the same amount of liquid [27]. The



smallest reported heating elements have a width  $x$  thickness of about  $20 \times 20 \mu\text{m}$  [26].

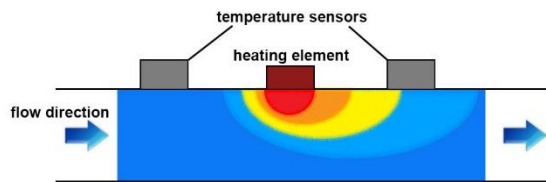


Figure 2: Schematic overview of a TMFRM. Heating element is located in between two temperature sensors. The time it takes for the heated-up fluid to reach the temperature sensors determines velocity.

## 2.2 Minimally invasive

A measurement method is defined as minimally invasive if small volumes of foreign elements or probes (most often, but not limited to, solids) are entrained (not static) in the flow. These probes or foreign elements, called tracers, are recorded by equipment outside the channel.

### 2.2.1 Particle image velocimeter (PIV)

Particle image velocimetry is perhaps the oldest (not attributed to an inventor due to unknown origin) tracking method in fluid dynamics. It requires the insertion of small particles with specific properties (fluorescence, high reflection, etc.) into the flow to be visually tracked using cameras (Figure 3). The spatial and temporal resolution are primarily dependent and restricted by the recording equipment and the tracer size.

There are many different tracers commercially available in a variety of densities and diameters

down to  $1 \mu\text{m}$ <sup>1,2</sup>, Error! Bookmark not defined.

Commercially available tracers with a nanoscopic diameter are rarer and less versatile but still available down to  $20 \text{ nm}$ <sup>1,2,3</sup>. Even with limited diversity, nanoscopic tracers are often used by researchers interested in  $\mu\text{m}$  and  $\text{nm}$  scale phenomena [28]–[30]. The smallest reported tracer is  $10 \text{ nm}$  in diameter and utilizes a biomolecular motor fixed in place to measure the motors rotation driven by the flow [31].

Depending on their diameter, tracers can be tracked with optical light-, compound-, or focal microscopy. The spatial resolution of a light microscope is limited to the wavelength of visible light which lies between  $400$  and  $700 \text{ nm}$  [32]. Smaller spatial resolutions can be obtained with a compound microscope down to  $200 \text{ nm}$ <sup>4</sup> or a confocal microscope down to  $10 \text{ nm}$  [33]. An even higher spatial resolution in order to track the

<sup>1</sup> [https://www.thermofisher.com/order/catalog/en/US/adirect/lt?cmd=catDisplayStyle&catKey=89301&filterDispName=Uncolored%252C%2BNon-Fluorescent%2BParticles&\\_bcs\\_ =H4slIAAAAAAAAAAM1Py2rDMBD8G11qEmQLGuWYBymhJBRcexfSjhzIIZHWMf77jIMCPYTSY2HZ0a6G%0AnZIZLaR%2By8n1kslmufqRPnqLZVf9i1zJ9RKNDvUMAxzbinHdPYFOLcpYt0XNPPeA1MkQMoOny3H%0AgAuiUVNJzbmnaZYLCAhIDabWS1k%2FYVyTcTdxE6G3rg7e5IQ6iPzRhIpeZcGWsMmpMvd2PsJzTif%0AyTJegYXa2eiE2u4%2FXo4gb33pghk3humS8g gjWL7SCMbn488gZxPK4yQTLuV3ov%2BUYPL0KMEXcpY7%0AdRMCAA%3D](https://www.thermofisher.com/order/catalog/en/US/adirect/lt?cmd=catDisplayStyle&catKey=89301&filterDispName=Uncolored%252C%2BNon-Fluorescent%2BParticles&_bcs_ =H4slIAAAAAAAAAAM1Py2rDMBD8G11qEmQLGuWYBymhJBRcexfSjhzIIZHWMf77jIMCPYTSY2HZ0a6G%0AnZIZLaR%2By8n1kslmufqRPnqLZVf9i1zJ9RKNDvUMAxzbinHdPYFOLcpYt0XNPPeA1MkQMoOny3H%0AgAuiUVNJzbmnaZYLCAhIDabWS1k%2FYVyTcTdxE6G3rg7e5IQ6iPzRhIpeZcGWsMmpMvd2PsJzTif%0AyTJegYXa2eiE2u4%2FXo4gb33pghk3humS8g gjWL7SCMbn488gZxPK4yQTLuV3ov%2BUYPL0KMEXcpY7%0AdRMCAA%3D)

<sup>2</sup> <http://www.polysciences.com/default/catalog-products/microspheres-particles/polymer-microspheres/polybead-sup-r-sup-microspheres>

<sup>3</sup> <http://www.polysciences.com/default/catalog-products/microspheres-particles/polymer-microspheres/polybead-sup-r-sup-microspheres>

<sup>4</sup> <http://www.cas.miamioh.edu/mbiws/microscopes/re-solution.html>

tracer movement more accurately can be obtained by using a digital holographic microscope [34].

The temporal and spatial resolution are hardware-dependent and compete for a high resolution by lowering the other. For the extreme 10 nm temporal resolution mentioned in the previous paragraph, a frame rate of only 4 Hz was possible when using a confocal microscope [33]. A higher frame rate such as 4  $\mu$ s (100 kHz) has been reported in literature for a 203 nm spatial resolution [35].

PIV can also be used for tracking flow in three dimensions. This can be done over the camera's entire field of view, by using two or three cameras and multiple optical access points with an 90° offset [36]–[38].

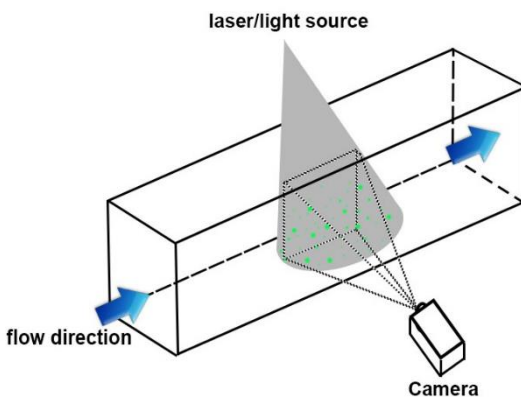


*Figure 3: Particle Imaging technique for two-dimensional tracking, where light reflects on visually distinct different particles (green) from the flow of interest. In order to track fluid speed and direction, the position of each particle and time in between each frame allows to track an entire area.*

### 2.2.2 X-ray Imaging

X-ray Imaging, invented by W. Rontgen in 1895 [39], uses high frequency -which is the same as short wavelength- waves that can pass through solid objects (Figure 4). X-ray imaging is mostly used for stationary objects and flows with no optical access point, in which case the technique is called X-ray velocimetry.

X-ray velocimetry was first introduced in 2003 [40], and it requires particles to be introduced into the flow that scatter X-rays and thus are shown on the X-ray camera as dark spots. These dark spots (i.e., detector did not receive an x-ray) represent the particles where the x-rays were deflected from.

Current equipment of X-ray imaging can obtain resolution of 30-50 nm for stationary solid objects [41], [42]. For rheological applications, exposure time is shorter the more accurately a flow needs to be tracked, and the faster the fluid flow is. This limits the spatial resolution of X-ray velocimetry.

Since the first publication on X-ray velocimetry, significant progress has been achieved in spatial and temporal resolution. In 2003, a spatial resolution of 12.3  $\mu$ m was achieved at a speed of 20 ms/image (50 Hz) [40]. In 2007, a spatial resolution of 5.87  $\mu$ m was reported [43]. In 2012, temporal resolutions were reported down to 200  $\mu$ s (5 kHz) for 14  $\mu$ m spatial resolution [44]. These resolutions decreased further in 2018 down to 7 ms (~140 Hz) for a 7  $\mu$ m resolution [45].

Spatial resolutions below  $1\ \mu\text{m}$  has not been reported yet but is expected to occur when recent patented improvements [46] are implemented into commercially available machines. This aforementioned patent claims to be capable of creating images with an effective pixel size of  $0.52\ \mu\text{m}$  with an exposure time of just  $4.5\ \text{ms}$  ( $220\ \text{Hz}$ ). The correctness, implementation difficulties, and conditions required to obtain such resolutions are currently unknown.

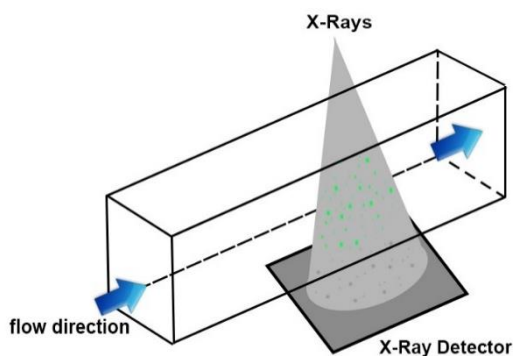


*Figure 4: A set-up for two-dimensional X-ray particle tracking. The flow enclosed in a solid channel with no optical access points is being measured by the position of tracking particles (green) which leave dark spots on the detector, and time between frames.*

### 2.2.3 Magnetic Resonance Velocimetry (MRV)

The MRV method uses magnetic resonance imaging (MRI) and/or other nuclear magnetic resonance (NMR) techniques to track tracer particles in the fluid flow (Figure 5). It requires tracers with high magnetically conductive properties (most metals), unless the fluid flow in question is a liquid metal [24]. This measurement is done by quickly switching between inducing the

field on the magnetically conductive tracer and measuring the field of that tracer. The switch between inducing and measuring the magnetic field happens fast because induced magnetic fields do not last long. MRV was first tested and evaluated by tracking a steady flow in 1990 [47]. The measurement accuracy of MRV is partially dependent on the strength of the magnetic field [48].

Up until 2003, MRV had a spatial resolution range around  $200\ \mu\text{m}$  for a fluid flow of  $1\ \text{mm/s}$ , while the highest temporal resolutions were around  $10\text{-}30\ \text{ms}$  ( $33\text{-}100\ \text{Hz}$ ). This was mainly due to using clinical MRI equipment, which has a limited magnetic field strength of  $1\text{-}3\ \text{T}$  [48]–[50]. Nevertheless, minor improvements continued to be made, and in 2018, a temporal resolution of  $1\text{-}3\ \text{ms}$  ( $330\text{-}1000\ \text{Hz}$ ) was achieved with a  $2\ \text{T}$  clinical MRI machine. The spatial resolution of this method was  $3\ \text{mm}$  for a field of view of  $196 \times 196\ \text{mm}$  [51].

The spatial and temporal resolution of MRV greatly improved when MRI equipment for non-clinical purposes were developed. Currently, the strongest MRI machine for non-clinical purposes has a magnetic field strength of  $21.1\ \text{T}$  and can render images with a resolution of  $50\ \mu\text{m}$  at a rate of  $1.1\ \text{ms/image}$  ( $909\ \text{Hz}$ ) [52].

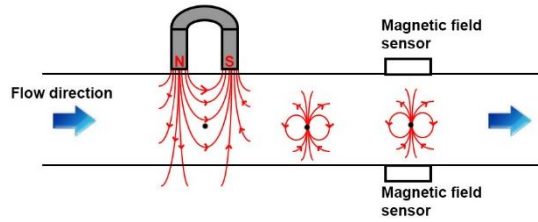


Figure 5: Magnetic Resonance Velocimetry using metallic particles (black dot). Magnetic particle can be tracked with a magnetic field sensor. This measurement is done by quickly switching between inducing the field and measuring the field at the same place.

### 2.3 Non-invasive

We define a method as non-invasive if the method does not require any physical interaction with the fluid flow of interest.

#### 2.3.1 Interferometry

The interferometer was invented by Albert Abraham Michelson [53]. In an interferometer, light from a single source is split into two beams (waves) that travel different optical paths. After each wave has traveled along their respective path, the two waves are recombined and produce interference, the fringes of which give information about the difference in optical path length (Figure 6). Since one path is through the flow, the difference in optical path length is directly correlated to the fluid flow speed. This means that tracer particles are not required [54] and that only one point in space can be measured.

On-chip interferometry can have a sensitivity of 0.127 nL/s and a spatial resolution of 54  $\mu\text{m}$  [54]. Variation on the originally designed

interferometry method (Figure 6) such as low coherence interferometry (optical coherence tomography) can have a spatial resolution of 4.5  $\mu\text{m}$  [55] and a temporal resolution of 52 ns [56].

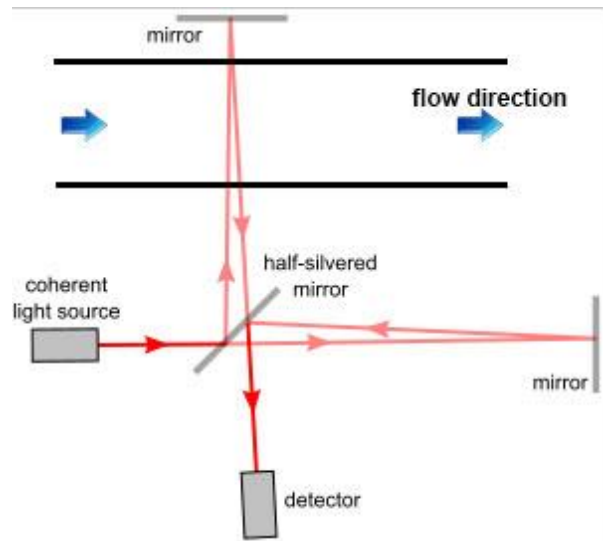


Figure 6:<sup>[5]</sup> The basic working principle of interferometry is splitting up one beam of light into two beams, letting one beam travel through the moving fluid and the other beam through a static (unmoving) medium. Interference resulting from recombining the two (split up) waves after traveling through their respective medium is used to determine the flow velocity.

The most widely used interferometrical method for fluidic measurements is Laser Doppler Velocimetry (LDV, also known as photonic doppler velocimetry), developed in 1964 [57]. In LDV, two beams of laser light (split from one beam) are crossed in the fluid flow. Transmitting optics focusses the beams to intersect at their waists (i.e., the focal point of a laser beam),

<sup>5</sup> <https://en.wikipedia.org/wiki/Interferometry>

where they interfere with each other resulting in a set of straight fringes (Figure 7). Based on the measured fringes, as well as light intensity and frequency, the velocity of the flow is determined.

Commercially available machines have become popular because of the high temporal resolution of 6.66 ms – 5.7 ns (300 Hz - 175 MHz) and high spatial resolution of 9 nm<sup>6</sup>. Turbulent gaseous mixing [58], pulsatile blood flow in capillary tubes [59], and the turbulent structure of axisymmetric diffusion flames [60] are three examples of flow types which LDV has been used for.

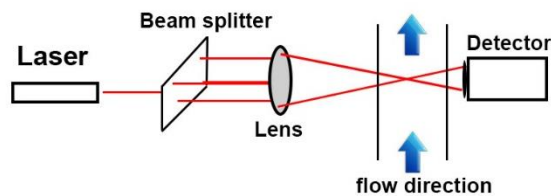


Figure 7: Laser Doppler Velocimetry measurement method. Split-up beams are crossing each other at a point in the flow, and after having passed through the entire fluid, all beams (light waves) are recorded by a detector. Depending on which beams received more interference from crossing, flow velocity is determined.

Another well-known method that uses interferometrical principles is Laser Speckle Velocimetry (LSV). Invented by Stavits in 1966, and specifically designed for measuring flows, this technique uses speckle patterns [61]. It is an effect produced by the mutual interference of a

set of wave fronts, which gives a grainy appearance to objects illuminated by laser light (Figure 8).

The lower limit in spatial resolution for LSV is about 1  $\mu\text{m}$  [62]. For a spatial resolution close to that lower limit (0.9  $\mu\text{m}$ ), an exposure time of 200  $\mu\text{s}$  (5 kHz) was needed [63]. When focusing more on the temporal resolution, an 11  $\mu\text{s}$  (92 kHz) measurement was reported for a spatial resolution of 7  $\mu\text{m}$  [64].

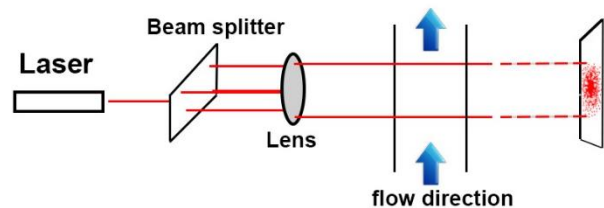


Figure 8: Laser Speckle Velocimetry (LSV). A single light wave is split up in multiple coherent light waves (lasers) and travel through the fluidic flow in order to get focused on a solid object. The coherent waves that hit the solid object are then recorded by a camera. Depending on the color and intensity of the speckles are used to analyze fluid flow velocity.

### 2.3.2 Ultrasound Image Velocimetry (UIV)

Ultrasound Image Velocimetry (UIV) is a non-invasive technique that works on a wide range of flows without the need for optical access (Figure 9). Invented in 1915 in the form of Sound Navigation And Ranging (SONAR), ultrasound waves were used to detect underwater objects [65]. In 1941, ultrasound was first used as a medical tool on humans to outline the ventricles of the human brain [66]. In retrospect, the blood flow in those ventricles might have been the first fluidic flow application of UIV.

<sup>6</sup> [http://www.tsi.com/uploadedFiles/Site\\_Root/Products/Literature/Spec\\_Sheets/DPSS\\_5001457\\_A4\\_WEB.pdf](http://www.tsi.com/uploadedFiles/Site_Root/Products/Literature/Spec_Sheets/DPSS_5001457_A4_WEB.pdf)

UIV is entirely based on the Doppler shift theorem which states that when a sound wave bounces off a moving medium (or object), it deforms the soundwave depending on the traveling direction and speed of that medium [67]. The changes in these waves are measured, and by using the Doppler shift theorem, fluidic velocity and direction can be obtained.

Perhaps the greatest limitation of UIV is that the transducer needs to be in direct contact with the channel. For microchannels, this means that the sensor and sound emitter needs to fit on a small area. The smallest probes currently reported in literature have diameters around 0.3 mm [68]. Spatial resolutions as low as 40  $\mu\text{m}$  [70] and temporal resolutions as low as 10 ns (100 MHz) [71] have been reported.

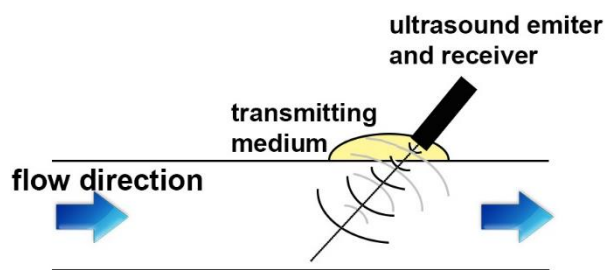


Figure 9: Ultrasound doppler velocimetry used to determine pipe flow velocity. Ultrasound waves (black) are sent through the channel and bounce back from the fluidic particles (light grey). According to the doppler theorem, depending on the frequency shift undergone by the waves, the speed is determined.

## 2.4 Other (Uncommon) Measurement Methods

The measurement methods here are either very new and require more research before actual

implementation into commercial products is possible or old methods which never received a lot of attention but offers a different way of measuring compared to the more commonly used methods.

### 2.4.1 Plasmonic Velocimetry

A plasmon (Figure 10) can be described as “a collective excitation/oscillation of the free electron gas density in a piece of conducting material”<sup>7</sup> or as “a physical phenomenon characterizing plasma oscillations”<sup>8</sup>. Plasmons were first introduced (theorized, not proven) in 1952 by D. Pines and D. Bohm [72]. One of the first papers providing experimental evidence and theoretical considerations about this (quantum) physical phenomenon was published in 2003 [73]. However, it was not until 2010 that the magnetic [74], chiral [75], and electrical [76] capabilities of plasmons were being explored and applications such as velocimetry were proposed.

Plasmonic velocimetry is very new and requires expensive equipment to make and track the particles. For example, to make a nanoparticle with a diameter of  $12 \pm 2$  nm diameter, block copolymer micelle nanolithography and vapor glancing angle deposition need to be used in order to create the tracers [77].

<sup>7</sup> <http://nanoscale.blogspot.nl/2009/02/what-is-plasmon.html>

<sup>8</sup> <http://www.horiba.com/scientific/products/surface-plasmon-resonance-imaging-spri/faqs/what-is-a-plasmon/>

The fluid flow is measured by subjecting the magnetic helices (Figure 10) to a rapidly rotating magnetic field and measuring the phase and amplitude of the resulting circular dichroism sign [77]. Circular dichroism is “the difference in the absorption of left-handed circularly polarized light and right-handed circularly polarized light”<sup>9</sup>. Dark field microscopy can be used to observe a 70 x 55  $\mu\text{m}$  area with a resolution of 500 nm every 3.3 ms [78].

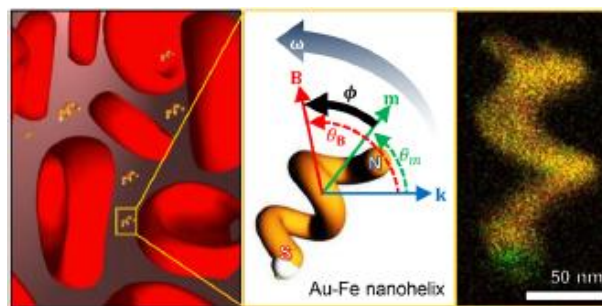


Figure 10: [77] Plasmonic velocimetry uses quantum particles and has a small layer of gold (or other meta) deposited on it in order to measure the fluid flow based on plasma oscillations.

#### 2.4.2 Laser Induced Photobleaching

Laser-induced fluorescence photobleaching anemometer (LIFPA) is a measurement technique introduced in 2005 and was specifically designed for the purpose of achieving high temporal and high spatial resolutions. In LIFPA, a laser shines into the flow filled with fluorescent dyed particles. These dyes lose fluorescence the longer they are in contact with the laser. The contact

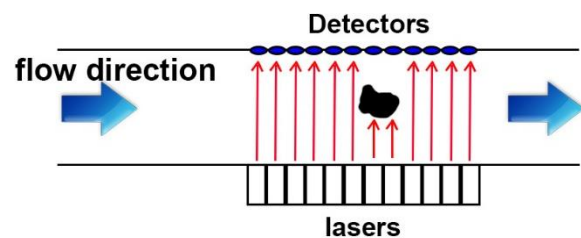
time of these particles is inversely proportional to the flow velocity, and thus the flow velocity can be determined by measuring the fluorescence intensity after the dye passed through the laser [29].

In 2009, the method was proven to obtain a temporal resolution of 100  $\mu\text{s}$  with a spatial resolution of 200-400 nm [79]. In 2010, a temporal resolution of 200  $\mu\text{s}$  with a spatial resolution of 70 nm [80] was reported. Invented in 2005, LIFPA is still in its early stages of development and can be expected to improve spatiotemporal resolution in the future.

#### 2.4.3 Spatial Filtering (SP)

First proposed in 1963 [81], SP has not received much attention. In SP, the solid particles velocity and size is determined as they pass through a laser beam and cast shadows on to an array of optical fibers or photodetectors (Figure 11). An example of a spatial filter is a transmission grating or a parallel slit reticle [61].

Spatial filtering is compact, inexpensive, and easy to handle. Its spatial resolution is lower than that of LDV, but the accuracy of both techniques are at the same order [82].



<sup>9</sup> <https://www.chem.uci.edu/~dmitryf/manuals/Fundamentals/CD%20spectroscopy.pdf>

*Figure 11: Spatial filtering method principle. Lasers are sent through a flow with tracers in it in order to detect on the other receiving end of the lasers, when the tracer interrupts the laser signal. The speed of the flow is determined by the speed how fast the detectors regain a signal.*

## 2.5 Hybrid measurement methods

Hybrid measurement methods refer to the combined use of two or more measurement methods. Several examples are briefly discussed.

Planar particle image doppler velocimetry combines high-resolution digital particle imaging velocimetry with doppler global velocimetry. It can measure all three velocity components across a planar region from a small single access point [83].

The hybrid multi-scale velocimetry from S. Haavisto et al., combines doppler optical coherence tomography with either magnetic resonance imaging or ultrasound velocity profiling. The measurement setup can analyze the flow velocity and direction as well as wall layer dynamics, and has been evaluated by four different fluids under varying flow regimes [84].

Ultrasound speckle image velocimetry combines the advantages of speckle velocimetry and ultrasound imaging [85]. It has been applied for the simultaneous measurement of velocity fields and the speckle pattern from red blood cell under pulsatile blood flows [85], [86].

## 3. Pressure

Pressure sensors measure the force inside a fluid exerted over an area that is in contact with that

fluid. An important criterion when choosing a pressure measurement method is whether and to what extent the required measuring equipment alters the pressurized channel (e.g., channel geometry, channel roughness, etc.). Accordingly, in this review, the measurement methods are categorized based on the degree of invasiveness. Three levels of decreasing invasiveness are distinguished here: invasive, minimally invasive, and non-invasive. All pressure sensor performance data is split up into two large sections, the performance found in commercially obtainable items and the performance reported in academic literature. Relative pressure sensors - sensors with a variable reference pressure- are not discussed in this review because the accuracy and maximum measurable pressure of a sensor with a variable reference pressure is dependent on the reference pressure and strength of the components.

### 3.1 Invasive

A method is defined as invasive when either the chip or probe takes up space inside the pressurized channel or if, in case of a flow, it requires a piece of equipment (i.e., probe) to remain static inside the flow. The amount of disturbance to the pressure mainly depends on the dimensions of the probe or sensor compared to the dimensions of the pressurized channel.

#### 3.1.1 Servo-Null Micropipette System (SNMS)



Invented in 1958 [87], the SNMS measures the resistance at the tip of the recording electrode and the reference electrode which are both filled with a fluid. When the recording electrode is inserted into a pressurized environment, hydrostatic forces push liquid further into the electrode tip, resulting in a change in resistance. A pump creates a counter-pressure until the resistance in the recording electrode is equal to the resistance in the reference electrode. When both resistances are the same, the counter-pressure that was added represents the difference in pressure between the reference and recording electrode [88]. SNMS is often used in low-pressure and no- or slow-flow environments such as intra-ocular [89] and microvascular [90] pressure.

Commercially obtainable SNMS can reach pressures up to 46.66 kPa with a resolution of 66 Pa and a measurement time of 10 ms<sup>10</sup> (100 kHz). A pressure measurement with an accuracy between 27 and 54 Pa has been reported in literature to be taken every 2.5 and 4 ms (250 – 400 Hz) with a maximum pressure well below 1 kPa [89], [91], [92].

Commercially available SNMS uses probes between 2 and 5  $\mu\text{m}$  in diameter<sup>10</sup>. In the literature, an electrode tip as small as 0.1  $\mu\text{m}$  has been reported [92] but generally range between 1 and 5  $\mu\text{m}$  [89], [91].

---

<sup>10</sup> <https://www.wpiinc.com/products/top-products/sys-900a-micropressure-system/>

### 3.1.2 Ionization gauge

An ion pressure sensor works by supplying an electrical current to an electron emitter which creates electrons and ions from being in contact with air. The creation of these electrons and ions result in an electron-ion current flow. This flow passes over an electron collector leaving a flow of ions behind. Pressure can then be determined by measuring the current being created by the ion collector from converting ions into an electrical signal (Figure 12). The electrical signal is proportional to pressure because electron-ion creation is directly related to the gas density. It is mostly used for pressures between atmospheric pressure and vacuum conditions and only works for compressible gasses.

Commercial products can measure pressures up to 133 kPa<sup>11</sup> with an accuracy as low as 1  $\mu\text{Pa}$ <sup>12</sup> and a measurement frequency of 50 ms<sup>13</sup> (20 Hz). Ion gauges reported in the literature can measure up to 101 kPa [93] with an accuracy of 35 nPa and a measuring frequency of 10  $\mu\text{s}$  (100 kHz) [94].

The smallest commercially available ionization sensors currently available do not go below 20 mm diameter<sup>14,15</sup> while sensors described in the

---

<sup>11</sup> <https://products.inficon.com/en-us/nav-products/product/detail/pge500/>

<sup>12</sup> <https://www.vacom.de/en/products/total-pressure-measurement/ionization-vacuum-gauge/hot-cathode-ionization-vacuum-gauges/1007-product-overview>

<sup>13</sup> [http://www.instrutechinc.com/site/files/1082/124782/427457/779090/IGM401\\_Data\\_Sheet.pdf](http://www.instrutechinc.com/site/files/1082/124782/427457/779090/IGM401_Data_Sheet.pdf)

<sup>14</sup> <https://www.mksinst.com/product/Product.aspx?ProductID=459>

literature have a reported area of 2.8 x 2.8 mm [95].

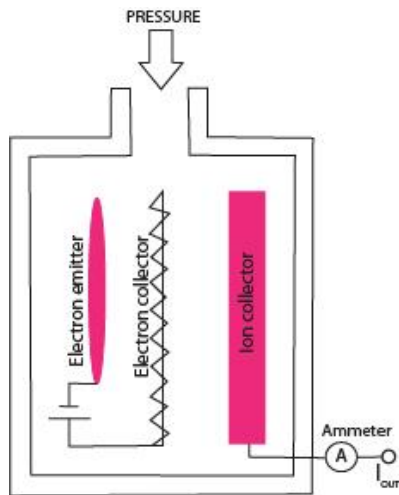


Figure 12:16 An ion pressure gauge, where the electron emitter converts creates an electron-ion flow. The electron-ion flow passes through the electron collector leaving an ion flow behind. The ions that pass through are detected by the ion collector which creates an electrical signal out of the ions.

### 3.2 Minimally Invasive

A method is defined as minimally invasive when the sensor can be integrated into the wall resulting in a spot with different surface roughness and/or small geometrical deviations from the rest of the channel at the location of the sensor.

#### 3.2.1 Piezo Resistor

Piezo resistance was experimentally evaluated for the first time in 1953 by C. Smith [96]. A piezo resistor changes its electrical resistance depending on the applied mechanical strain. By

<sup>15</sup> <http://www.instrutechinc.com/miniature-ion-bayard-alpert-vacuum-gauge/>

<sup>16</sup> <https://wiki.metropolia.fi/display/sensor/Pressure+ensor>

measuring the change in resistance, the pressure is determined.

Commercially available piezo resistive pressure sensors have an operation range up to 100 MPa<sup>17,18,19</sup> with resolutions as low as 1 Pa<sup>20</sup> and measurement frequencies of down to 1.32  $\mu\text{s}$ <sup>21</sup> (760 kHz). Piezo resistive sensors reported in the literature measured pressures up to 150 MPa [97]. Literature also reported a pressure resolution of 0.8 Pa [98], and a measurement frequency down to 1  $\mu\text{s}$  (1 MHz) [99].

The smallest surface area of commercially available sensors are around 2 x 2 x 0.72 mm<sup>20,21</sup>. Similar sized devices have been reported in literature when miniaturization is not required [100]–[102]. However, sizes as small as 75 x 75  $\mu\text{m}$  have also been reported [103].

#### 3.2.2 Piezoelectric

The piezoelectric effect was first discovered in 1880 [104] and states that piezoelectricity is the internal generation of an electrical charge resulting from an applied mechanical force.

<sup>17</sup> <http://www.directindustry.com/prod/ahlborn/product-17042-1911984.html>

<sup>18</sup> <http://www.directindustry.com/prod/nuova-fima/product-14044-471692.html>

<sup>19</sup> <http://www.directindustry.com/prod/meggitt-sensing-systems-measurement-group/product-5413-416891.html>

<sup>20</sup> <https://eu.mouser.com/new/sensors/pressure-sensors/industrial-pressure-sensors/n-6g7qk>

<sup>21</sup> [https://eu.mouser.com/ds/2/418/NG\\_DS\\_XP5\\_A1-1013767.pdf](https://eu.mouser.com/ds/2/418/NG_DS_XP5_A1-1013767.pdf)

However, it was not until 1917 that the first sensor using piezoelectricity was made [105].

Present-day commercial piezoelectrical sensors can measure up to 1 GPa<sup>22</sup>. Measurement in low pressure environments (0 - 6.8 MPa) can be taken as fast as 2  $\mu$ s (500 kHz) with a resolution of 0.689 Pa<sup>23</sup>. Piezoelectrical sensors reported in literature have measured pressures up to 110 GPa [106], at a frequency of 10 ns (100 MHz) [107], and a resolution of 5 mPa [108].

Similar to the piezo resistors, commercially available devices take up an area of 3 x 3 mm [109]<sup>24</sup> or more. The size of piezoelectric sensors reported in literature has been reducing from 200 x 200  $\mu$ m in 2008 [110] to 140 x 140  $\mu$ m in 2017 [111].

### 3.2.3 Piezo-Phototronic

Piezo-phototronic effect is a coupling effect of piezoelectric, semiconductor and photonic properties. Discovered in 2010 [112], [113], the electrical potential generated by the piezoelectric effect is used to activate the integrated photonic properties. There are no commercially available sensors using this principle yet.

The highest pressure reported in literature using the piezo-phototronic effect is 100 MPa

[114] and the highest reported measurement frequency is 10 ms (100 Hz) [115]. The resolution is unknown, as the main focus currently lies on sensitivity, brightness, and efficiency (electricity required for photon activation). The minimum dimensions reported in literature of one piezo-phototronic element can be as small as 2-3  $\mu$ m in length with a diameter around 200-300 nm [116]. However, a sensor using this principle has many (hundreds or thousands) of these elements, and it is currently unclear what the smallest number of elements is in order to create an operational sensor.

### 3.2.4 Capacitive

Developed in 1970 for use in aerospace applications [117], a capacitive pressure sensor uses parallel plates (capacitor) in an electrical circuit to detect the pressure-dependent distance or area shared between those plates (Figure 13). Capacitance is directly related to the shared area divided by the distance of the plates. With the capacitance being measured and knowing either the shared area or distance of the plates, the pressure on the pressure dependent variable (shared area or distance) is determined.

Commercially available capacitive sensors can measure pressures up to 6.8 MPa<sup>25</sup>, and have a resolution of 1 Pa at a measurement frequency of

---

<sup>22</sup> <https://www.kistler.com/en/product/type-6213b--pe-sensor/>

<sup>23</sup> [http://www.pcb.com/TestMeasurement/Pressure/hi\\_sensitivity](http://www.pcb.com/TestMeasurement/Pressure/hi_sensitivity)

<sup>24</sup> [http://www.pcb.com/contentstore/docs/PCB\\_Corporate/Pressure/products/Manuals/M132A31.pdf](http://www.pcb.com/contentstore/docs/PCB_Corporate/Pressure/products/Manuals/M132A31.pdf)

---

<sup>25</sup> [http://cdn1.kavlico.com/downloads/datasheets/P255\\_Data\\_Sheet\\_A4.pdf](http://cdn1.kavlico.com/downloads/datasheets/P255_Data_Sheet_A4.pdf)

2.5  $\mu\text{s}$ <sup>26</sup> (400 kHz). In literature, capacitance sensor have been reported to measure pressures up to 100 MPa [118], with measurement frequencies of 385 ns (2.6 MHz) [119], and an accuracy of 0.1 Pa [120].

Present-day commercially available capacitive sensors rarely become smaller than 1.5 x 1.5 mm<sup>27</sup>, whereas pressure sensor reported in literature have gone as small as 100 x 100  $\mu\text{m}$  [120], [121].

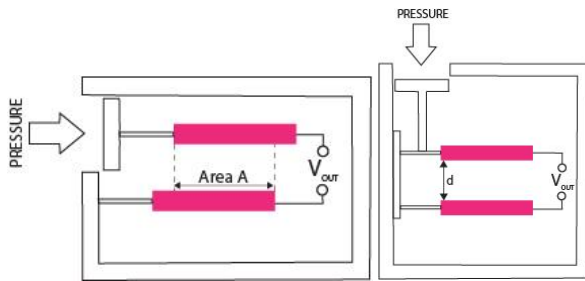


Figure 13<sup>26</sup>: A capacitive sensor measures capacitance to determine the distance or area between the two plates which are dependent on the pressure.

### 3.2.5 Electromagnetic

First patented in 1929 [122], an electromagnetic pressure sensor measures the displacement of an electro-magnetic field due to pressure by means of inductance, the Hall effect, or the eddy current principle (Figure 14).

The pressure range, sensitivity, and area vary depending on the type of electromagnetic sensor. Both the Hall effect and the eddy current pressure sensors are not commercially available likely because there are cheaper, easier, and

smaller alternatives such as inductive or piezo sensors. For the same reason, academic research into Hall effect or Eddy current pressure sensing is also limited.

Commercially available inductive sensors can measure up to 50 MPa at a measurement frequency of 200  $\mu\text{s}$ <sup>28,29</sup> (5 kHz). Lower range pressure sensor can have a sensitivity of 0.5 Pa<sup>30</sup>. Sensors reported in literature have shown to measure pressures up to 450 kPa [123], with a resolution of 3  $\mu\text{Pa}$  [124] is possible when an inductive meter with a 10 nH accuracy is connected<sup>31</sup>. Literature studies have reported a measuring frequency as fast as 100 ns (10 MHz) [125].

The smallest commercial inductive pressure sensors has an area around 1.5 x 1.5 mm<sup>29</sup> while the smallest sensor reported in literature has an area of 750 x 750  $\mu\text{m}$  [126].

Hall effect sensors reported in literature goes up to 275 kPa, with a sensitivity of 6 Pa [127], and with areas larger than 1 x 1 mm [128], [129]. In literature reported Eddy current sensors, have not been reported to measure above 14 kPa [130] and have an area around 10 x 10 mm [131].

<sup>26</sup> <https://eu.mouser.com/new/sensors/pressure-sensors/tdk-icp-10100-sensor-ics/n-6g7qcZ2fna23>

<sup>27</sup> <https://pressureprofile.com/general-sensor-catalog>

<sup>28</sup> <https://www.locon.net/inductive/high-pressure.html>

<sup>29</sup> [https://www.contrinex.com/product\\_range/inductive-high-pressure/](https://www.contrinex.com/product_range/inductive-high-pressure/)

<sup>30</sup> <http://www.fsm.ag/en/production-pressure-sensors-dps.php>

<sup>31</sup> [http://electronics-diy.com/lc\\_meter.php](http://electronics-diy.com/lc_meter.php)

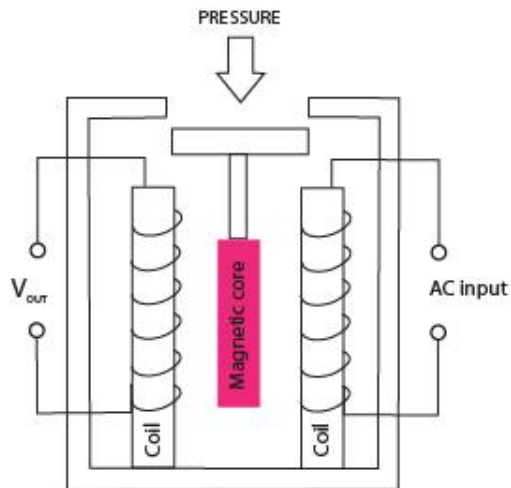


Figure 14<sup>16</sup>: An inductive pressure sensor where a pressure moves the magnetic field. The amplitude of the displacement of the magnetic field is proportional to the output voltage which is used to calculate the applied pressure.

### 3.2.6 Light Waves

Light wave sensors are based on measuring changes in amplitude, frequency, phase, or other alterations to the properties of a wave in order to determine pressure. The most researched and commercially available sensors using light wave alterations is the optical fiber sensors.

Optical fiber sensors can alter the intensity, phase, polarization, wavelength or transit time of light depending on its internal structure. When applying a pressure on the outside of the cable, the internal structure will slightly deform and thus reveal information about the pressure. For example, an internal structure designed for taking out one specific wavelength at a set pressure (i.e., atmospheric pressure), removes a shorter or longer wavelength when its internal structure is deformed due to an change in pressure. Therefore, by analyzing the properties of light

coming out of the optical fiber and comparing it to the reference situation, the pressure on the optical fiber is determined.

Commercially available medical optical fiber pressure sensors can have resolutions down to 26 Pa<sup>32</sup> and measurement frequencies as fast as 4 ms (250 Hz) [132]. The range of pressure measuring with these devices reach up to 10 MPa<sup>33</sup>. Optical fiber sensors reported in literature have a resolution of 20 mPa and measurement frequency of 0.5 ms (2 kHz) [133]. The maximum pressure reported in literature goes up to 140 MPa [134].

The smallest area of commercially available light wave sensors is 80  $\mu\text{m}$  diameter for medical related pressure measurements [132]. Sensors reported in literature have a diameter around 700  $\mu\text{m}$  [133] when miniaturization is not required. However, a diameter as small as  $29.8 \pm 1.6 \mu\text{m}$  have been reported [135].

### 3.2.7 Resonant Principle

First patented in 1972 [136], the resonant principle uses a pressure or density dependent resonant amplitude or frequency. A change in frequency can be observed when density is the variable (works only for compressible fluids) due to more resistance while a change in amplitude which is pressure dependent can work under all conditions (Figure 15).

<sup>32</sup> <https://opsens-solutions.com/products/fiber-optic-pressure-sensors/opp-m/>

<sup>33</sup> [https://fibergratings.com/sensors\\_pressure.html](https://fibergratings.com/sensors_pressure.html)

Commercially available sensors can measure pressures up to 100 MPa<sup>34</sup> at measurement frequencies of 2 ms<sup>34</sup> (500 Hz). The accuracy in these commercial sensors can go down to 10 Pa<sup>35</sup>. Resonant sensors reported in literature have measured pressures up to 11.8 MPa with a pressure accuracy of 2 Pa [137]. The reported measurement frequency of these sensors can go as fast as 50  $\mu$ s (20 kHz) [138].

Both commercial and in literature reported sensors are generally large because it consists out of multiple parts and because it requires space for oscillation. The smallest surface area of commercially available sensor is 20 mm in diameter<sup>35</sup>, while in literature reported resonant sensors have gone down to 1 x 1 mm [139].

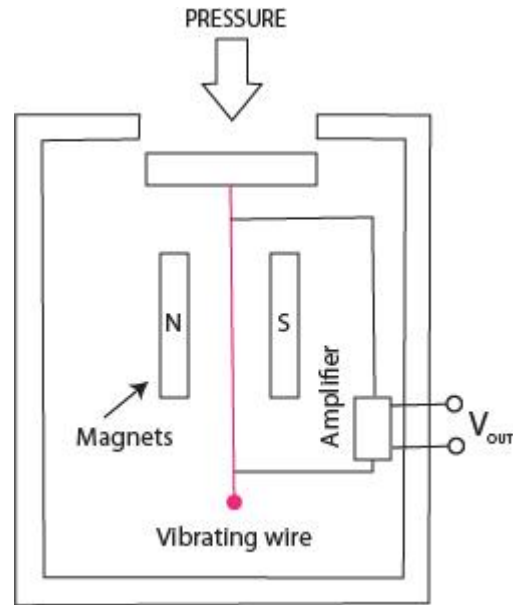


Figure 15<sup>16</sup>: A resonant pressure sensor where the vibration amplitude is dependent on the applied pressure. The position of the vibrating wire is directly proportional to the output voltage.

### 3.2.8 Pirani Gauge

Invented in 1906 [140], the Pirani gauge works by running a current through a wire suspended in a compressible fluid while measuring the wire's resistance (Figure 16). When molecules hit the wire, they take heat away and change the resistance. Therefore, lower pressure means a lower density and less molecules to hit the wire resulting in a hotter wire and a change in resistance.

Commercially available sensors can measure pressures between 0.1  $\mu$ Pa and 101 kPa (1 atm)<sup>36</sup>. These sensors can have a measurement frequency of 1 ms (1 kHz) with a resolution of 1  $\mu$ Pa<sup>36</sup>. Sensors in literature have been reported

<sup>34</sup> <http://www.directindustry.com/prod/dytran-instruments/product-37504-965865.html>

<sup>35</sup> <https://www.gemeasurement.com/sensors-probes-transducers/pressure-transducers-and-transmitters/8000-series-terps-resonant-pressure-sensor>

<sup>36</sup> <https://webshop.demaco.nl/wgm701-wasp-cold-cathode-inverted-magnetron-pirani-vacuum-gauge->

to measure 800 kPa [141] and have a resolution as low as 0.1  $\mu\text{Pa}$  [142]. It has also been reported a measurement frequency of 0.465 ns (2.15 GHz) [143].

The surface area of a commercially available Pirani gauges goes down to around  $2 \times 2 \text{ mm}^2$ . In literature, surfaces areas of  $325 \times 325 \mu\text{m}$  [144] and  $350 \times 3 \mu\text{m}$  are the smallest sensors reported, for a resolution equal to commercial equipment [142]. However, the sensors have been reported to go down to  $40 \times 40 \mu\text{m}$  [145].

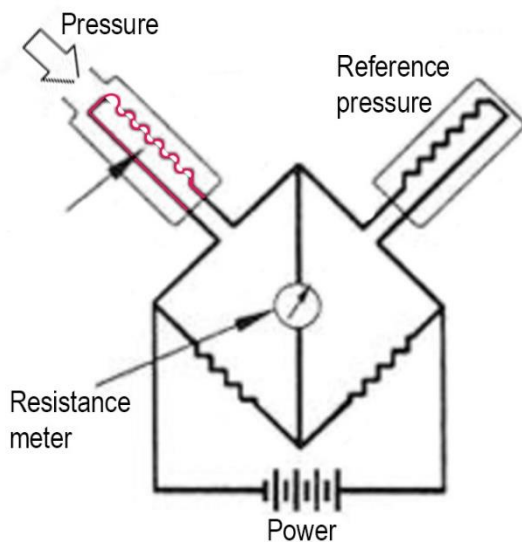


Figure 16<sup>16</sup>: Pirani gauge setup where the resistance of a heated resistor in a pressurized gas is measured to determine the pressure.

### 3.2.9 Potentiometric

A potentiometer is an adjustable variable resistor with a sliding or rotating contact (Figure 17). In

[dn25kf-fitting-1.html?gclid=Cj0KCQiA2snUBRDfARIsAIGfpqE\\_e36sEfOnwvns9sSjl2P9cK4perhgQzmgwLPxOjRVOGmb03vfZkg\\_aAsZpEALw\\_wcB](https://www.researchgate.net/publication/325252511-dn25kf-fitting-1.html?gclid=Cj0KCQiA2snUBRDfARIsAIGfpqE_e36sEfOnwvns9sSjl2P9cK4perhgQzmgwLPxOjRVOGmb03vfZkg_aAsZpEALw_wcB)

this sensor, the contact point changes depending on the pressure resulting in a system with a different resistance. This resistance change is then used to determine pressure.

The potentiometric method for measuring pressure is rarely used commercially and in literature, and will according to Greenslade never become mainstream because of cheaper, smaller and more accurate methods [146]. These cheaper and more accurate methods such as the piezo resistive or pirani gauge even use the same principle (change in resistance) thus making it obsolete.

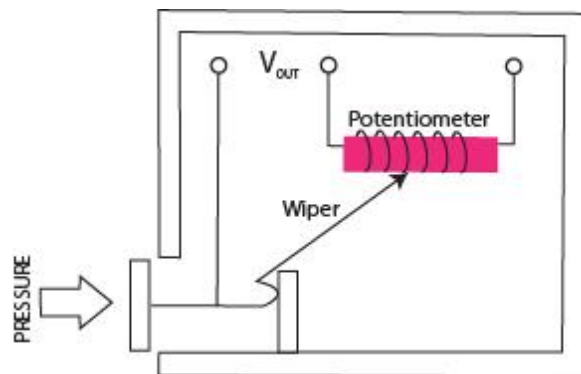


Figure 17<sup>16</sup>: A potentiometer relating wiper movement (contact point) to the surrounding pressure resulting in a different resistance and output voltage.

## 3.3 Noninvasive

A pressure measurement method is described as noninvasive when the sensor is indistinguishable from the wall in terms of surface roughness or geometry either by becoming the channel itself, or by measuring without contact to the pressure.

### 3.3.1 Pressure Sensitive Paint (PSP)

First tested in the early 1990s [147], PSP works by making particles emit a color (wavelength) depending on the applied pressure (without electricity generation or supply) and recording it with a camera. This principle originally used natural emittance (wave length emittance of a particle) that was dependent on the density of air. Recently, PSP became liquid compatible [148]. PSP is noninvasive, because it can be applied to the entire wall of the pressurized channel therefore becoming the new channel.

Although PSP has gained a lot of popularity among researchers, it can only custom ordered commercially due to it being a new method and it being tailored to performance criteria.

PSP found in literature has been reported to measure pressures up to 10 GPa [149]. Measurement frequencies have been reported to go down to 10  $\mu$ s (100 kHz) with an accuracy of 1  $\mu$ Pa [150]. The thickness of a PSP layer is generally between 1 and 10  $\mu$ m [151].

#### **4. Discussion**

Fluidic flow and pressure measurement methods vary widely in performance criteria (Table 1). After experimentalists have eliminated the methods that do not fulfill their desired requirements, the method(s) with the lowest level of invasiveness should be considered first. Lower levels of invasiveness means more realistic results.

Very invasive flow measurement methods have already started to disappear commercially and in research due to the need for more realistic results. Currently, non-invasive methods cannot measure an area (multiple points simultaneously) with the same spatial or temporal resolution as minimally invasive techniques. Therefore, what can be predicted is that the once non-invasive methods are starting to close the gap in performance criterion with minimally invasive methods, they will start to disappear as well.

Improvements in fluidic flow measurement methods cannot be predicted due to each method having their own limiting factors and complexity. However, methods that are often used such as the PIV and LDV method, and very recently discovered methods with low (or none) invasiveness such as plasmonic velocimetry.

Most of the fluidic pressure measurement methods have already become compatible with both gas and liquid. Unless the method offers performances better than any other under specific conditions, methods not compatible with both types of fluid are expected to disappear or made compatible for both due to their exceptional performance under the right conditions.

Fluidic pressure measurement methods that have been incapable of shrinking or no longer offer competitive performance compared to other sensor of the same size such as electromagnetic and resonant sensors are



(expected to become) neglected. Improvements are expected to be made towards often used measurement methods such as PSP, piezo resistive, and piezoelectrical sensors, as well as promising new methods such as piezo-phototronics.

Table 1: Fluid flow measurement methods with expected performance levels in microfluidic flow measurements.

Method	Invasiveness	Physical Principle	Spatial Resolution	Temporal Resolution	Point or area	Optical access
Electrical Tomography	Very	Resistance, capacitance, magnetic inductance	0.13x 50 $\mu\text{m}$ or 0.26 x 3.36 $\mu\text{m}$	17 $\mu\text{s}$	Point	No
Mass Flow Rate Meter	Very	Temperature	20 $\mu\text{m}$	N/A	Point	No
PIV and PTV	Minimally	Visual Tracking	10 nm	4 $\mu\text{s}$	Area	Yes
X-ray	Minimally	X-ray Imaging	7 $\mu\text{m}$	200 $\mu\text{s}$	Area	No
MRV	Minimally	Magnetic fields	50 $\mu\text{m}$	1 ms	Area	No
Interferometry	Not	Waves fringes	9 nm	5.7 ns	Point	Yes
UIV	Not	Doppler effect	40 $\mu\text{m}$	10 ns	Area	No
Plasmons	Minimally	Plasmonic Oscillations	500 nm	3.3 ms	Area	Yes
Laser induced photobleaching	Minimally	Decay time & visual	70 nm	100 $\mu\text{s}$	Point	Yes
Spatial filtering	Not	Shadow tracking	N/A	N/A	Point	No

Table 2: Pressure measurement method overview with all specification. First value represents commercial products and the second value are reported in literature.

Method	Physical Working Principle	Max Pressure*	Accuracy	Chip or probe area	Temporal Resolution **	Liquid or Gas
Piezo resistive	Resistance change from induced strain	100 MPa 150 MPa	1 Pa 0.8 Pa	2 x 2 mm 75 x 75 $\mu\text{m}$	1.32 $\mu\text{s}$ 1 $\mu\text{s}$	Both
Piezoelectric	electricity from induced strain	1 GPa 110 GPa	0.689 Pa 0.005 Pa	3 x 3 mm 140 x 140 $\mu\text{m}$	2 $\mu\text{s}$ 10 ns	Both
Piezo-phototronic	Piezoelectric and photonic	N/A 100 MPa	N/A N/A	N/A N/A	N/A 10 ms	Both
Capacitive	Electrical capacitance	6.8 MPa 100 MPa	1 Pa 0.1 Pa	1.5 x 1.5 mm 100 x 100 $\mu\text{m}$	2.5 $\mu\text{s}$ 385 ns	Both
Electromagnetic	inductance, Hall Effect, or eddy current	50 MPa 450 kPa	0.5 Pa 3 $\mu\text{Pa}$	>1.5 x 1.5 mm >750 x 750 $\mu\text{m}$	200 $\mu\text{s}$ 100 ns	Both
Light Wave Alteration	Interferometry, light sensitivity,	10 MPa 140 MPa	26 Pa 20 mPa	80 x 80 $\mu\text{m}$ 29.8 $\pm$ 1.6 $\mu\text{m}$	4 ms 0.5 ms	Both

	fiber optics (FBG)					
Visually	sensitive paint, sensitive films	N/A 10 GPa	N/A 1 $\mu$ Pa	N/A N/A	N/A 10 $\mu$ s	Both
Resonant	Vibration resistance	100 Mpa 11.8 MPa	10 Pa 2 Pa	20 x 20 mm 1 x 1 mm	2 ms 50 $\mu$ s	Both
Pirani Gauge	Temperature	101 kPa 800 kPa	1 $\mu$ Pa 1 $\mu$ Pa	2 x 2 mm 40 x 40 $\mu$ m	1 ms 0.465 ns	Gas
Servo Null	Resistance & pressure equalization	< 1 kPa < 1 kPa	66 Pa 27 – 54 Pa	2 x 2 $\mu$ m 0.1 x 0.1 $\mu$ m	10 ms 2.5 - 4 ms	Liquid
Ion Gauge	Electrically induced ionization	133 kPa 101 kPa	1 $\mu$ Pa 35 nPa	20 x 20 mm 2.8 x 2.8 mm	50 ms 10 $\mu$ s	Gas
Potentiometer	Variable resistance	N/A N/A	N/A N/A	N/A N/A	N/A N/A	Both
Pressure Sensitive Paint	Pressure dependent natural emittance	N/A 10 GPa	N/A 1 $\mu$ Pa	N/A 1-10 $\mu$ m	N/A 10 $\mu$ s	Both

\*\* time it takes to have taken one measurement of the pressure

\* Values of Inductance will be used since it is the only one that is also commercially available

## 5. Conclusion

In this paper, we reviewed microfluidic flow and pressure measurement methods. The analyzation criteria of the paper allows for experimentalists to explore methods based on required performance and level of invasiveness first, and working principle compatibility second. Often principle compatibility is the first criteria and insufficient performance criteria are worked around, but this review will hopefully help the experimentalist to put performance criteria first and work around measurement compatibility.

Working around the compatibility will hopefully results in novel work-arounds resulting in using methods for a wider variety of applications. Some of these new work-arounds might create a more universal measurement method for flow or pressure. Realizing that the performance criteria of these methods change often, and the amount of improvement cannot be predicted, a clear trend towards non-invasive methods for more realistic measurement can be seen the better non-invasive methods become.

## References

- [1] P. Tabeling, *Introduction to microfluidics*. Oxford University Press, 2005.
- [2] H. Bruus, *Theoretical microfluidics*. Oxford : Oxford University Press, 2008.
- [3] G. Karniadakis, *Microflows and Nanoflows*, vol. 29. New York: Springer-Verlag, 2005.
- [4] B. (Brian J. . Kirby, *Micro- and nanoscale fluid mechanics : transport in microfluidic devices*. Cambridge University Press, 2010.
- [5] K. E. Herold and A. Rasooly, *Lab on a chip technology*. Norfolk, UK : : Caister Academic Press, 2009.
- [6] G. Pascali, P. Watts, and P. A. Salvadori, "Microfluidics in radiopharmaceutical chemistry," *Nucl. Med. Biol.*, vol. 40, no. 6, pp. 776–787, Aug. 2013.
- [7] K. Li and S. Cai, "Wet adhesion between two soft layers," *Soft Matter*, vol. 10, no. 41, pp. 8202–8209, Oct. 2014.
- [8] J. Wang, "On-chip enzymatic assays," *Electrophoresis*, vol. 23, no. 5, pp. 713–718, Mar. 2002.
- [9] H. Moon, A. R. Wheeler, R. L. Garrell, J. A. Loo, and C.-J. Kim, "An integrated digital microfluidic chip for multiplexed proteomic sample preparation and analysis by MALDI-MS," *Lab Chip*, vol. 6, no. 9, p. 1213, Aug. 2006.
- [10] F. Ozsolak and P. M. Milos, "RNA sequencing: advances, challenges and opportunities," *Nat. Rev. Genet.*, vol. 12, no. 2, pp. 87–98, Feb. 2011.
- [11] Julia Khandurina, Timothy E. McKnight, Stephen C. Jacobson, Larry C. Waters, and Robert S. Foote, and J. M. Ramsey\*, "Integrated System for Rapid PCR-Based DNA Analysis in Microfluidic Devices," 2000.
- [12] L. B. Slichter, "The Interpretation of the Resistivity Prospecting Method for Horizontal Structures," *Physics (College Park. Md).*, vol. 4, no. 9, pp. 307–322, Sep. 1933.
- [13] S. Sun, L. Xu, Z. Cao, H. Zhou, and W. Yang, "A high-speed electrical impedance measurement circuit based on information-filtering demodulation," *Meas. Sci. Technol.*, vol. 25, no. 7, p. 75010, Jul. 2014.
- [14] M. Wang and W. Yin, "Measurements of the Concentration and Velocity Distribution in Miscible Liquid Mixing Using Electrical Resistance Tomography," *Chem. Eng. Res. Des.*, vol. 79, no. 8, pp. 883–886, Nov. 2001.
- [15] G. T. Bolton, C. W. Hooper, R. Mann, and E. H. Stitt, "Flow distribution and velocity measurement in a radial flow fixed bed reactor using electrical resistance tomography," *Chem. Eng. Sci.*, vol. 59, no. 10, pp. 1989–1997, May 2004.
- [16] D. Holder, *Electrical impedance tomography : methods, history, and applications*. Bristol : Institute of Physics Pub, 2005.
- [17] Y. Fan, G. Arwatz, T. W. Van Buren, D. E. Hoffman, and M. Hultmark, "Nanoscale sensing devices for turbulence measurements," *Exp. Fluids*, vol. 56, no. 7, p. 138, Jul. 2015.
- [18] A. Talbi *et al.*, "A micro-scale hot wire anemometer based on low stress (Ni/W) multi-layers deposited on nano-crystalline diamond for air flow sensing," *J. Micromechanics Microengineering*, vol. 25, no. 12, p. 125029, Dec. 2015.
- [19] J. Zhao, H. Völlm, D. Feili, T. Panidis, and H. Seidel, "Nano-scale Hot Wire Sensors for Turbulence Measurement Applications," *Procedia Eng.*, vol. 47, pp. 845–848, Jan. 2012.
- [20] S. Liu *et al.*, "Micro triple-hot-wire anemometer on small sized glass tube fabricated in 5DOF UV lithography system," in *2015 28th IEEE International Conference on Micro Electro Mechanical Systems (MEMS)*, 2015, pp. 714–717.
- [21] R. Que and R. Zhu, "Aircraft Aerodynamic Parameter Detection Using Micro Hot-Film Flow Sensor Array and BP Neural Network Identification," *Sensors*, vol. 12, no. 12, pp. 10920–10929, Aug. 2012.
- [22] P. Liu, R. Zhu, and R. Que, "A Flexible Flow Sensor System and Its Characteristics for Fluid Mechanics Measurements," *Sensors*, vol. 9, no. 12, pp. 9533–9543, Nov. 2009.
- [23] A. Jaworski and T. Dyakowski, "Application of electrical capacitance tomography for measurement of gas-solids flow

- characteristics in a pneumatic conveying system Application of electrical capacitance tomography for measurement of gas-solids flow characteristics in a pneumatic conveying system A J Jaworski and T Dyakowski - Regularization Reconstruction Method for Imaging Problems in Electrical," *Meas. Sci. Technol.*, vol. 12, 2001.
- [24] A. Gailitis *et al.*, "Detection of a Flow Induced Magnetic Field Eigenmode in the Riga Dynamo Facility," *Phys. Rev. Lett.*, vol. 84, no. 19, pp. 4365–4368, May 2000.
- [25] L. V. King, "On the Convection of Heat from Small Cylinders in a Stream of Fluid: Determination of the Convection Constants of Small Platinum Wires with Applications to Hot-Wire Anemometry," *Philos. Trans. R. Soc. A Math. Phys. Eng. Sci.*, vol. 214, no. 509–522, pp. 373–432, Jan. 1914.
- [26] H. Berthet, J. Jundt, J. Durivault, B. Mercier, and D. Angelescu, "Time-of-flight thermal flowrate sensor for lab-on-chip applications," *Lab Chip*, vol. 11, no. 2, pp. 215–223, Jan. 2011.
- [27] W. D. Callister and D. G. Rethwisch, *Materials science and engineering : an introduction.*, 8th edition /. 2010.
- [28] H.-S. Chuang, L. Gui, and S. T. Wereley, "Nano-resolution flow measurement based on single pixel evaluation PIV," *Microfluid. Nanofluidics*, vol. 13, no. 1, pp. 49–64, Jul. 2012.
- [29] G. R. Wang, "Laser induced fluorescence photobleaching anemometer for microfluidic devices," *Lab Chip*, vol. 5, no. 4, p. 450, 2005.
- [30] J. H. Lee *et al.*, "Microfluidic centrifuge of nano-particles using rotating flow in a microchamber," *Sensors Actuators B Chem.*, vol. 132, no. 2, pp. 525–530, Jun. 2008.
- [31] S.-W. Lee, H. Kinoshita, H. Noji, T. Fujii, and T. Yamamoto, "Biomolecular Nano-Flow-Sensor to Measure Near-Surface Flow," *Nanoscale Res. Lett.*, vol. 5, no. 2, pp. 296–301, Feb. 2010.
- [32] P. A. Buser and M. Imbert, *Vision*. MIT Press, 1992.
- [33] L. H. Wong, N. A. Kurniawan, H.-P. Too, and R. Rajagopalan, "Spatially resolved microrheology of heterogeneous biopolymer hydrogels using covalently bound microspheres," *Biomech. Model. Mechanobiol.*, vol. 13, no. 4, pp. 839–849, Aug. 2014.
- [34] H. LEI *et al.*, "Nano-level position resolution for particle tracking in digital in-line holographic microscopy," *J. Microsc.*, vol. 260, no. 1, pp. 100–106, Oct. 2015.
- [35] W. Zhao, F. Yang, J. Khan, K. Reifsnider, and G. Wang, "Measurement of velocity fluctuations in microfluidics with simultaneously ultrahigh spatial and temporal resolution," *Exp. Fluids*, vol. 57, no. 1, p. 11, Jan. 2016.
- [36] S. Fu, P. H. Biwole, and C. Mathis, "Numerical and experimental comparison of 3D Particle Tracking Velocimetry (PTV) and Particle Image Velocimetry (PIV) accuracy for indoor airflow study," *Build. Environ.*, vol. 100, pp. 40–49, May 2016.
- [37] K. Hoyer, M. Holzner, B. Lüthi, M. Guala, A. Liberzon, and W. Kinzelbach, "3D scanning particle tracking velocimetry," *Exp. Fluids*, vol. 39, no. 5, pp. 923–934, Nov. 2005.
- [38] T. P. Chang, N. A. Wilcox, and G. B. Tatterson, "Application Of Image Processing To The Analysis Of Three-Dimensional Flow Fields," *Opt. Eng.*, vol. 23, no. 3, pp. 283–1, Jun. 1984.
- [39] H. Münsterberg, "THE X-RAYS.," *Science*, vol. 3, no. 57, pp. 161–3, Jan. 1896.
- [40] S.-J. Lee and G.-B. Kim, "X-ray particle image velocimetry for measuring quantitative flow information inside opaque objects," *J. Appl. Phys.*, vol. 94, no. 102, 2003.
- [41] J. Chen, C. Wu, J. Tian, W. Li, S. Yu, and Y. Tian, "Three-dimensional imaging of a complex concaved cuboctahedron copper sulfide crystal by x-ray nanotomography," *Appl. Phys. Lett.*, vol. 92, no. 23, p. 233104, Jun. 2008.
- [42] G.-C. Yin *et al.*, "30nm resolution x-ray imaging at 8keV using third order diffraction of a zone plate lens objective in a

- transmission microscope," *Appl. Phys. Lett.*, vol. 89, no. 22, p. 221122, Nov. 2006.
- [43] A. Fouras, J. Dusting, R. Lewis, and K. Hourigan, "Three-dimensional synchrotron x-ray particle image velocimetry," *J. Appl. Phys.*, vol. 102, no. 6, p. 64916, Sep. 2007.
- [44] R. A. Jamison, K. K. W. Siu, S. Dubsky, J. A. Armitage, and A. Fouras, "X-ray velocimetry within the ex vivo carotid artery," *J. Synchrotron Radiat.*, vol. 19, no. 6, pp. 1050–1055, Nov. 2012.
- [45] G. W. Goonan, A. Fouras, and S. Dubsky, "Array-source X-ray velocimetry," *Opt. Express*, vol. 26, no. 2, p. 935, Jan. 2018.
- [46] A. Fouras and S. Dubsky, "Particle image velocimetry suitable for x-ray projection imaging," 2010.
- [47] D. N. Ku, C. L. Biancheri, R. I. Pettigrew, J. W. Peifer, C. P. Markou, and H. Engels, "Evaluation of Magnetic Resonance Velocimetry for Steady Flow," *J. Biomech. Eng.*, vol. 112, no. 4, p. 464, Nov. 1990.
- [48] L. F. Gladden, "Magnetic resonance: Ongoing and future role in chemical engineering research," *AIChE J.*, vol. 49, no. 1, pp. 2–9, Jan. 2003.
- [49] K. Kose, "Instantaneous flow-distribution measurements of the equilibrium turbulent region in a circular pipe using ultrafast NMR imaging," *Phys. Rev. A*, vol. 44, no. 4, pp. 2495–2504, Aug. 1991.
- [50] N. Olamaei, F. Cheriet, S. Deschênes, A. Sharafi, and S. Martel, "Three-dimensional reconstruction of a vascular network by dynamic tracking of magnetite nanoparticles," *Med. Phys.*, vol. 42, no. 10, pp. 5702–5710, Sep. 2015.
- [51] S. Lakshmanan, W. A. Maru, D. J. Holland, M. D. Mantle, and A. J. Sederman, "Measurement of an oil–water flow using magnetic resonance imaging," *Flow Meas. Instrum.*, vol. 53, pp. 161–171, Mar. 2017.
- [52] V. D. Schepkin, W. W. Brey, P. L. Gor'kov, and S. C. Grant, "Initial in vivo rodent sodium and proton MR imaging at 21.1 T," *Magn. Reson. Imaging*, vol. 28, no. 3, pp. 400–407, Apr. 2010.
- [53] J. Grasselli, "On the Relative Motion of the Earth and the Luminiferous Ether," *Appl. Spectrosc. Vol. 41, Issue 6, pp. 933-935*, vol. 41, no. 6, pp. 933–935, Aug. 1987.
- [54] D. A. Markov, S. Dotson, S. Wood, and D. J. Bornhop, "Noninvasive fluid flow measurements in microfluidic channels with backscatter interferometry," *Electrophoresis*, vol. 25, no. 21–22, pp. 3805–3809, Nov. 2004.
- [55] K. Sleiman *et al.*, "Optical Coherence Tomography Predictors of Risk for Progression to Non-Neovascular Atrophic Age-Related Macular Degeneration," *Ophthalmology*, vol. 124, no. 12, pp. 1764–1777, Dec. 2017.
- [56] M. Siddiqui, A. S. Nam, S. Tozburun, N. Lippok, C. Blatter, and B. J. Vakoc, "High-speed optical coherence tomography by circular interferometric ranging," *Nat. Photonics*, vol. 12, no. 2, pp. 111–116, Feb. 2018.
- [57] Y. Yeh and H. Z. Cummins, "LOCALIZED FLUID FLOW MEASUREMENTS WITH AN He–Ne LASER SPECTROMETER," *Appl. Phys. Lett.*, vol. 4, no. 10, pp. 176–178, May 1964.
- [58] G. Bouzgarrou, Y. Bury, S. Jamme, L. Joly, and J.-F. Haas, "Laser Doppler Velocimetry Measurements in Turbulent Gaseous Mixing Induced by the Richtmyer–Meshkov Instability: Statistical Convergence Issues and Turbulence Quantification," *J. Fluids Eng.*, vol. 136, no. 9, p. 91209, Jul. 2014.
- [59] K. R. Brein and C. E. Riva, "Laser Doppler velocimetry measurement of pulsatile blood flow in capillary tubes," *Microvasc. Res.*, vol. 24, no. 1, pp. 114–118, Jul. 1982.
- [60] J. P. Sislian, L.-Y. Jiang, and R. A. Cusworth, "Laser doppler velocimetry investigation of the turbulence structure of axisymmetric diffusion flames," *Prog. Energy Combust. Sci.*, vol. 14, no. 2, pp. 99–146, Jan. 1988.
- [61] Y. Aizu and T. Asakura, "Principles and development of spatial filtering velocimetry," *Appl. Phys. B Photophysics Laser Chem.*, vol. 43, no. 4, pp. 209–224, Aug. 1987.

- [62] F.-P. Chiang, "Micro-/Nano-Speckle Method with Applications to Materials, Tissue Engineering and Heart Mechanics," *Strain*, vol. 44, no. 1, pp. 27–39, Jan. 2008.
- [63] S. N. Ma and Q. Lin, "Laser speckle velocimetry: using modulated dynamic speckle to measure the velocity of moving diffusers," *Appl. Opt.*, vol. 25, no. 1, p. 22, Jan. 1986.
- [64] W. J. Choi, Y. Li, W. Qin, and R. K. Wang, "Cerebral capillary velocimetry based on temporal OCT speckle contrast," *Biomed. Opt. Express*, vol. 7, no. 12, p. 4859, Dec. 2016.
- [65] S. Singh and A. Goyal, "The Origin of Echocardiography: A Tribute to Inge Edler," *Texas Hear. Inst. J.*, vol. 34, no. 4, p. 431, 2007.
- [66] K. T. Dussik, "Über die Möglichkeit, hochfrequente mechanische Schwingungen als diagnostisches Hilfsmittel zu verwerten," *Zeitschrift für die gesamte Neurol. und Psychiatr.*, vol. 174, no. 1, pp. 153–168, Dec. 1942.
- [67] C. Doppler, *About the colored light of the double stars and some other stars of the sky*. Calve, 1842.
- [68] M. Schumacher, L. Yin, S. Swaid, J. Oldenburger, J. M. Gilsbach, and A. Hetzel, "Intravascular Ultrasound Doppler Measurement of Blood Flow Velocity," *J. Neuroimaging*, vol. 11, no. 3, pp. 248–252, Jul. 2001.
- [69] G. T. Bui, Y.-T. Jiang, and D.-C. Pang, "Two Capacitive Micro-Machined Ultrasonic Transducers for Wind Speed Measurement.," *Sensors (Basel)*, vol. 16, no. 6, Jun. 2016.
- [70] F. Peters, L. Lobry, and E. Lemaire, "Pressure-driven flow of a micro-polar fluid: Measurement of the velocity profile," *J. Rheol. (N. Y. N. Y.)*, vol. 54, no. 2, p. 311, Mar. 2010.
- [71] L. Elvira, P. Vera, F. J. Cañadas, S. K. Shukla, and F. Montero, "Concentration measurement of yeast suspensions using high frequency ultrasound backscattering," *Ultrasonics*, vol. 64, pp. 151–161, Jan. 2016.
- [72] D. Pines and D. Bohm, "A Collective Description of Electron Interactions: II. Collective vs Individual Particle Aspects of the Interactions," *Phys. Rev.*, vol. 85, no. 2, pp. 338–353, Jan. 1952.
- [73] E. Prodan, C. Radloff, N. J. Halas, and P. Nordlander, "A Hybridization Model for the Plasmon Response of Complex Nanostructures," *Science (80-. )*, vol. 302, no. 5644, pp. 419–422, Oct. 2003.
- [74] G. Armelles, A. Cebollada, A. García-Martín, and M. U. González, "Magnetoplasmonics: Combining Magnetic and Plasmonic Functionalities," *Adv. Opt. Mater.*, vol. 1, no. 1, pp. 10–35, Jan. 2013.
- [75] V. K. Valev, J. J. Baumberg, C. Sibilia, and T. Verbiest, "Chirality and Chiroptical Effects in Plasmonic Nanostructures: Fundamentals, Recent Progress, and Outlook," *Adv. Mater.*, vol. 25, no. 18, pp. 2517–2534, May 2013.
- [76] M. T. Sheldon, J. van de Groep, A. M. Brown, A. Polman, and H. A. Atwater, "Plasmoelectric potentials in metal nanostructures," *Science (80-. )*, vol. 346, no. 6211, pp. 828–831, Nov. 2014.
- [77] H.-H. Jeong *et al.*, "Active Nanorheology with Plasmonics," *Nano Lett.*, vol. 16, no. 8, pp. 4887–4894, Aug. 2016.
- [78] Z. Zhang, Q. Li, S. S. Haque, and M. Zhang, "Far-field plasmonic resonance enhanced nanoparticle image velocimetry within a microchannel," *Rev. Sci. Instrum.*, vol. 82, no. 2, p. 23117, Feb. 2011.
- [79] C. Kuang, W. Zhao, F. Yang, and G. Wang, "Measuring flow velocity distribution in microchannels using molecular tracers," *Microfluid. Nanofluidics*, vol. 7, no. 4, pp. 509–517, Oct. 2009.
- [80] C. Kuang and G. Wang, "A novel far-field nanoscopic velocimetry for nanofluidics," *Lab Chip*, vol. 10, no. 2, pp. 240–245, Dec. 2010.
- [81] J. T. Ator, "Image-Velocity Sensing with Parallel-Slit Reticles\*," *J. Opt. Soc. Am.*, vol. 53, no. 12, p. 1416, Dec. 1963.
- [82] Y. Aizu and T. Asakura, *Spatial Filtering Velocimetry*, vol. 116. Berlin/Heidelberg: Springer-Verlag, 2006.
- [83] M. P. Wernet-Dgv, J. F. Meyers, J. W. Lee, and R. J. Schwartz, "Planar particle imaging Doppler velocimetry: a hybrid

- PIV/DGV technique for three-component velocity measurements Temporally resolved PIV for space–time correlations in both cold and hot jet flows,” *Meas. Sci. Technol.*, vol. 15, 2004.
- [84] S. Haavisto *et al.*, “Experimental investigation of the flow dynamics and rheology of complex fluids in pipe flow by hybrid multi-scale velocimetry,” *Exp. Fluids*, vol. 58, no. 11, p. 158, Nov. 2017.
- [85] E. Yeom, K.-H. Nam, D.-G. Paeng, and S. J. Lee, “Improvement of ultrasound speckle image velocimetry using image enhancement techniques,” *Ultrasonics*, vol. 54, no. 1, pp. 205–216, Jan. 2014.
- [86] S. J. Lee, J. H. Park, J. J. Kim, and E. Yeom, “Quantitative Analysis of Helical Flow with Accuracy Using Ultrasound Speckle Image Velocimetry: In Vitro and in Vivo Feasibility Studies,” *Ultrasound Med. Biol.*, vol. 44, no. 3, pp. 657–669, Mar. 2018.
- [87] M. B. Rappaport, E. H. Bloch, J. W. Irwin, and J. W. Irwin, “A manometer for measuring dynamic pressures in the microvascular system,” *Am. Physiol. Soc.*, pp. 651–654, 1958.
- [88] B. A. Link, M. P. Gray, R. S. Smith, and S. W. M. John, “Intraocular pressure in zebrafish: Comparison of inbred strains and identification of a reduced melanin mutant with raised IOP,” *Investig. Ophthalmol. Vis. Sci.*, vol. 45, no. 12, pp. 4415–4422, Dec. 2004.
- [89] M. Y. Avila, D. A. Carré, R. A. Stone, and M. M. Civan, “Reliable measurement of mouse intraocular pressure by a servo-null micropipette system,” *Invest. Ophthalmol. Vis. Sci.*, vol. 42, no. 8, pp. 1841–6, Jul. 2001.
- [90] K. A. Overholser, J. Bhattacharya, and N. C. Staub, “Microvascular pressures in the isolated, perfused dog lung: Comparison between theory and measurement,” *Microvasc. Res.*, vol. 23, no. 1, pp. 67–76, Jan. 1982.
- [91] R. Inamoto, T. Miyashita, A. Matsubara, H. Hoshikawa, and N. Mori, “The difference in endolymphatic hydrostatic pressure elevation induced by isoproterenol between the ampulla and the cochlea,” *Auris Nasus Larynx*, vol. 44, no. 3, pp. 282–287, Jun. 2017.
- [92] J. R. Fox and C. A. Wiederhielm, “Characteristics of the servo-controlled micropipet pressure system,” *Microvasc. Res.*, vol. 5, no. 3, pp. 324–335, May 1973.
- [93] I.-M. Choi and S.-Y. Woo, “Application of carbon nanotube field emission effect to an ionization gauge,” *Appl. Phys. Lett.*, vol. 87, no. 17, p. 173104, Oct. 2005.
- [94] H. Zhang *et al.*, “An ionization gauge for ultrahigh vacuum measurement based on a carbon nanotube cathode,” *Rev. Sci. Instrum.*, vol. 88, no. 10, p. 105107, Oct. 2017.
- [95] D. Li, Y. Cheng, Y. Wang, H. Zhang, C. Dong, and D. Li, “Improved field emission properties of carbon nanotubes grown on stainless steel substrate and its application in ionization gauge,” *Appl. Surf. Sci.*, vol. 365, pp. 10–18, Mar. 2016.
- [96] C. S. Smith, “Piezoresistance Effect in Germanium and Silicon,” *Phys. Rev.*, vol. 94, no. 1, pp. 42–49, Apr. 1954.
- [97] Z. Niu, Y. Zhao, and B. Tian, “Design optimization of high pressure and high temperature piezoresistive pressure sensor for high sensitivity,” *Rev. Sci. Instrum.*, vol. 85, no. 1, p. 15001, Jan. 2014.
- [98] L. Pan *et al.*, “An ultra-sensitive resistive pressure sensor based on hollow-sphere microstructure induced elasticity in conducting polymer film,” *Nat. Commun.*, vol. 5, p. 3002, Jan. 2014.
- [99] H. Zhao and J. Bai, “Highly Sensitive Piezo-Resistive Graphite Nanoplatelet–Carbon Nanotube Hybrids/Polydimethylsilicone Composites with Improved Conductive Network Construction,” *ACS Appl. Mater. Interfaces*, vol. 7, no. 18, pp. 9652–9659, May 2015.
- [100] T. Xu *et al.*, “Piezoresistive pressure sensor with high sensitivity for medical application using peninsula-island structure,” *Front. Mech. Eng.*, vol. 12, no. 4, pp. 546–553, Dec. 2017.

- [101] H. S. Ko, C. Gau-, R. Baviere, and F. Ayela, "Micromachined strain gauges for the determination of liquid flow friction coefficients in microchannels Bonding of a complicated polymer microchannel system for study of pressurized liquid flow characteristics with the electric double effect Micromachined strain gauges for the determination of liquid flow friction coefficients in microchannels," *Meas. Sci. Technol. Meas. Sci. Technol*, vol. 15, no. 15, pp. 377–377, 2004.
- [102] L. Tang, K. Zhang, S. Chen, G. Zhang, and G. Liu, "MEMS inclinometer based on a novel piezoresistor structure," *Microelectronics J.*, vol. 40, no. 1, pp. 78–82, Jan. 2009.
- [103] V. Mitrakos *et al.*, "Nanocomposite-Based Microstructured Piezoresistive Pressure Sensors for Low-Pressure Measurement Range," *Micromachines*, vol. 9, no. 2, p. 43, Jan. 2018.
- [104] J. Curie and P. Curie, "Contractions et dilatations produites par des tensions dans les cristaux hémihédres à faces inclinées," pp. 1137–1140, 1881.
- [105] S. Katzir, "Who knew piezoelectricity? Rutherford and Langevin on submarine detection and the invention of sonar," *Notes Rec. R. Soc.*, vol. 66, no. 2, pp. 141–157, Jun. 2012.
- [106] S. Yoshida, H. Hanzawa, K. Wasa, and S. Tanaka, "Fabrication and characterization of large figure-of-merit epitaxial PMnN-PZT/Si transducer for piezoelectric MEMS sensors," *Sensors Actuators A Phys.*, vol. 239, pp. 201–208, Mar. 2016.
- [107] M. Okandan *et al.*, "High Speed (GHz), Ultra-High Pressure (GPa) Sensor Array Fabricated in Integrated CMOS+MEMS Process," in *2009 IEEE 22nd International Conference on Micro Electro Mechanical Systems*, 2009, pp. 845–847.
- [108] C. Dagdeviren *et al.*, "Conformable amplified lead zirconate titanate sensors with enhanced piezoelectric response for cutaneous pressure monitoring," *Nat. Commun.*, vol. 5, p. 4496, Aug. 2014.
- [109] A. Kuoni, R. I. Holzherr, M. Boillat, and N. F. de Rooij, "Polyimide membrane with ZnO piezoelectric thin film pressure transducers as a differential pressure liquid flow sensor," *J. Micromechanics Microengineering*, vol. 13, no. 4, pp. S103–S107, Jul. 2003.
- [110] W.-Y. Chang, C.-H. Chu, and Y.-C. Lin, "A Flexible Piezoelectric Sensor for Microfluidic Applications Using Polyvinylidene Fluoride," *IEEE Sens. J.*, vol. 8, no. 5, pp. 495–500, May 2008.
- [111] M. Li, W. Cheng, J. Chen, R. Xie, and X. Li, "A High Performance Piezoelectric Sensor for Dynamic Force Monitoring of Landslide.," *Sensors (Basel)*, vol. 17, no. 2, Feb. 2017.
- [112] Z. L. Wang, "Piezopotential gated nanowire devices: Piezotronics and piezo-phototronics," *Nano Today*, vol. 5, no. 6, pp. 540–552, Dec. 2010.
- [113] Y. Hu, Y. Chang, P. Fei, R. L. Snyder, and Z. L. Wang, "Designing the Electric Transport Characteristics of ZnO Micro/Nanowire Devices by Coupling Piezoelectric and Photoexcitation Effects," *ACS Nano*, vol. 4, no. 2, pp. 1234–1240, Feb. 2010.
- [114] C. Pan *et al.*, "Progress in Piezo-Phototronic-Effect-Enhanced Light-Emitting Diodes and Pressure Imaging," *Adv. Mater.*, vol. 28, no. 8, pp. 1535–1552, Feb. 2016.
- [115] J. Zhou *et al.*, "Flexible Piezotronic Strain Sensor," *Nano Lett.*, vol. 8, no. 9, pp. 3035–3040, Sep. 2008.
- [116] B. Yin *et al.*, "Piezo-phototronic effect enhanced pressure sensor based on ZnO/NiO core/shell nanorods array," *Nano Energy*, vol. 21, pp. 106–114, Mar. 2016.
- [117] E. Turci, "New Capacitive Pressure Transducer for Aerospace Use," Springer, Dordrecht, 1970, pp. 712–718.
- [118] S. . Moe *et al.*, "Capacitive differential pressure sensor for harsh environments," *Sensors Actuators A Phys.*, vol. 83, no. 1–3, pp. 30–33, May 2000.
- [119] M. M. Abutaleb and A. M. Anis, "High-performance Dual-band Wireless Capacitive Pressure Sensor," *Int. J. Appl. Inf.*



*Syst.*, vol. 7, no. 8, pp. 28–31, Sep. 2014.

- [120] D. Davidovikj, P. H. Scheepers, H. S. J. van der Zant, and P. G. Steeneken, "Static Capacitive Pressure Sensing Using a Single Graphene Drum," *ACS Appl. Mater. Interfaces*, vol. 9, no. 49, pp. 43205–43210, Dec. 2017.
- [121] C.-L. Dai, P.-W. Lu, C. Chang, and C.-Y. Liu, "Capacitive Micro Pressure Sensor Integrated with a Ring Oscillator Circuit on Chip," *Sensors*, vol. 9, no. 12, pp. 10158–10170, Dec. 2009.
- [122] O. R. Schurig, "Electromagnetic pressure-measuring means," US1718494A, 25-Jun-1929.
- [123] H.-C. Chang *et al.*, "Wireless magnetostrictive type inductive sensing CMOS-MEMS pressure sensors," in *2016 IEEE 29th International Conference on Micro Electro Mechanical Systems (MEMS)*, 2016, pp. 218–221.
- [124] A. Arshad, K. A. Kadir, S. Khan, A. H. M. Z. Alam, and R. Tasnim, "A pressure sensor based inductive transducer designed for biomedical applications," in *2015 IEEE 3rd International Conference on Smart Instrumentation, Measurement and Applications (ICSIMA)*, 2015, pp. 1–6.
- [125] Y. W. Kim *et al.*, "Preliminary study on implantable inductive-type sensor for continuous monitoring of intraocular pressure," *Clin. Experiment. Ophthalmol.*, vol. 43, no. 9, pp. 830–837, Dec. 2015.
- [126] H.-C. Chang, S.-C. Liao, H.-S. Hsieh, J.-H. Wen, C.-H. Lai, and W. Fang, "Magnetostrictive type inductive sensing pressure sensor," *Sensors Actuators A Phys.*, vol. 238, pp. 25–36, Feb. 2016.
- [127] G. Rajita, D. Banerjee, N. Mandal, and S. C. Bera, "Design and Analysis of Hall Effect Probe-Based Pressure Transmitter Using Bellows as Sensor," *IEEE Trans. Instrum. Meas.*, vol. 64, no. 9, pp. 2548–2556, Sep. 2015.
- [128] Y. Kanda and A. Yasukawa, "Hall-effect devices as strain and pressure sensors," *Sensors and Actuators*, vol. 2, pp. 283–296, Jan. 1981.
- [129] H. Yu, M. Qin, and M. Nie, "MEMS Hall effect pressure sensor," *Electron. Lett.*, vol. 48, no. 7, p. 393, 2012.
- [130] B. . Dutoit, Y. Pilloud, F. Elegibili, P.-A. Besse, and R. . Popovic, "Flat electromagnetic pressure sensor for harsh environments," *Sensors Actuators A Phys.*, vol. 91, no. 1–2, pp. 51–56, Jun. 2001.
- [131] H. Lee, G. Lee, H. Kim, and J. Ahn, "Design of Diaphragm and Coil for Stable Performance of an Eddy Current Type Pressure Sensor," *Sensors*, vol. 16, no. 12, p. 1025, Jul. 2016.
- [132] S. Poeggel, D. Tosi, D. Duraibabu, G. Leen, D. McGrath, and E. Lewis, "Optical Fibre Pressure Sensors in Medical Applications," *Sensors*, vol. 15, no. 12, pp. 17115–17148, Jul. 2015.
- [133] M. Manzo, T. Ioppolo, U. K. Ayaz, V. LaPenna, and M. V. Ötügen, "A photonic wall pressure sensor for fluid mechanics applications," *Rev. Sci. Instrum.*, vol. 83, no. 10, p. 105003, Oct. 2012.
- [134] J.-Y. Huang *et al.*, "FBGs written in specialty fiber for high pressure/high temperature measurement," *Opt. Express*, vol. 25, no. 15, p. 17936, Jul. 2017.
- [135] M. de Fatima F Domingues *et al.*, "Liquid Hydrostatic Pressure Optical Sensor Based on Micro-Cavity Produced by the Catastrophic Fuse Effect," *IEEE Sens. J.*, vol. 15, no. 10, pp. 5654–5658, Oct. 2015.
- [136] W. C. Blanchard, "Resonant pressure sensor," 07-Jan-1972.
- [137] L. Zhu *et al.*, "A Resonant Pressure Sensor Capable of Temperature Compensation with Least Squares Support Vector Machine," *Procedia Eng.*, vol. 168, pp. 1731–1734, Jan. 2016.
- [138] X. Du, L. Wang, A. Li, L. Wang, and D. Sun, "High Accuracy Resonant Pressure Sensor With Balanced-Mass DETF Resonator and Twinborn Diaphragms," *J. Microelectromechanical Syst.*, vol. 26, no. 1, pp. 235–245, Feb. 2017.
- [139] Y. Sujan, G. Uma, and M. Umopathy, "Micro pressure sensor with three degrees of freedom resonator," *Microsyst. Technol.*, vol. 23, no. 8, pp. 3201–3214, Aug. 2017.

- [140] M. Von Pirani, "Selbszeigendes vakuu-mefsinstrument.," *Verhandlungen der Dtsch. Phys. Gesellschaft*, pp. 686–694, 1906.
- [141] C. Ghouila-Houri *et al.*, "High temperature gradient nanogap-Pirani micro-sensor with maximum sensitivity around atmospheric pressure," *Appl. Phys. Lett.*, vol. 111, no. 11, p. 113502, Sep. 2017.
- [142] D. Lee, Y. Noh, S. Park, M. Kumar, and Y. S. Cho, "Performance enhancement of Pirani gauge on silicon-on-insulator wafer with simple fabrication process," *Sensors Actuators A Phys.*, vol. 263, pp. 264–268, Aug. 2017.
- [143] M. Moutaouekkil *et al.*, "Elaboration of a Novel Design Pirani Pressure Sensor for High Dynamic Range Operation and Fast Response Time," *Procedia Eng.*, vol. 120, pp. 225–228, Jan. 2015.
- [144] J. Shie, B. C. S. Chou, and Y. Chen, "High performance Pirani vacuum gauge," *J. Vac. Sci. Technol. A Vacuum, Surfaces, Film.*, vol. 13, no. 6, pp. 2972–2979, Nov. 1995.
- [145] Jiaqi Wang, Zhenan Tang, Jinfeng Li, and Fengtian Zhang, "A MicroPirani Pressure Sensor Based on the Tungsten Microhotplate in a Standard CMOS Process," *IEEE Trans. Ind. Electron.*, vol. 56, no. 4, pp. 1086–1091, Apr. 2009.
- [146] T. B. Greenslade, "The Potentiometer," *Phys. Teach.*, vol. 43, no. 4, pp. 232–235, Apr. 2005.
- [147] C. Tropea and A. L. Yarin, *Handbook of Experimental Fluid Mechanics* -. Springer, 2007.
- [148] F. Cellini, S. D. Peterson, and M. Porfiri, "Highly compressible fluorescent particles for pressure sensing in liquids," *Appl. Phys. Lett.*, vol. 110, no. 22, p. 221904, May 2017.
- [149] A. A. Banishev and D. D. Dlott, "Ultrafast pressure-sensitive paint for shock compression spectroscopy," *J. Appl. Phys.*, vol. 115, no. 20, p. 203515, May 2014.
- [150] J. Crafton, A. Forlines, S. Palluconi, K.-Y. Hsu, C. Carter, and M. Gruber, "Investigation of transverse jet injections in a supersonic crossflow using fast-responding pressure-sensitive paint," *Exp. Fluids*, vol. 56, no. 2, p. 27, Feb. 2015.
- [151] H. Yokoyama, K. Miura, and A. Iida, "Measurement of unsteady surface pressure on rotor blades of fans by pressure-sensitive paint," in *AIP Conference Proceedings*, 2017, vol. 1807, no. 1, p. 20001.